Neutron Stars, the Exotica

From Modifying General Relativity to Strong Magnetic Fields

by

Farbod Kamiab

A thesis
presented to the University of Waterloo
in fulfillment of the
thesis requirement for the degree of
Doctor of Philosophy
in
Physics and Astronomy

Waterloo, Ontario, Canada, 2015

This thesis consists of material all of which I authored or co-authored: see Statement of Contributions included in the thesis. This is a true copy of the thesis, including any required final revisions, as accepted by my examiners.

I understand that my thesis may be made electronically available to the public.

Statement of Contributions

This dissertation is partially the product of collaborative research and co-authored publications. The following publications form the basis of Chapters 2 and 4 in this dissertation.

- **Farbod Kamiab** and Niayesh Afshordi, "Neutron Stars and the Cosmological Constant Problem", 2011, Physical Review D, 84, 063011
- **Farbod Kamiab**, Avery E. Broderick and Niayesh Afshordi, "The Mass and Radii of Strongly Magnetized Neutron Stars", 2015, arXiv:1503.03898, submitted to the Astrophysical Journal.

Chapter 3 in this thesis is the outcome of an on-going collaboration with Jonah Miller, Niayesh Afshordi and Erik Schnetter.

Abstract

The gravitational aether theory is a modification of General Relativity that decouples vacuum energy from gravity, and thus can potentially address the cosmological constant problem. The classical theory is distinguishable from General Relativity only in the presence of relativistic pressure (or vorticity). Since the interior of neutron stars has high pressure and as their mass and radius can be measured observationally, they are the perfect laboratory for testing the validity of the aether theory. In this thesis, we first solve the hydrostatic equations of stellar structure for the gravitational aether theory and find the predicted mass-radius relation of nonrotating neutron stars using two different realistic proposals for the equation of state of nuclear matter. We find that the maximum neutron-star mass predicted by the aether theory is 12%-16% less than the maximum mass predicted by General Relativity assuming these two equations of state. We then study the dynamics of a neutron star in the aether theory and establish that a Cauchy problem can be defined. We derive the dynamical equations, and through analyzing them, we find two modes, one of which is well-posed (expansion of matter in the aether frame) and the other is not well-posed (collapse of matter in the aether frame). Starting from a hydrostatic neutron star configuration that we perturb by adding extrinsic curvature (and radial velocity), we numerically evolve the Einstein field equations for the aether theory in the well-posed mode and find that it evolves towards the not well-posed regime. This feature may pose a serious challenge to our initial value formulation of the aether theory. Whether an alternative formulation can handle the collapsing neutron stars is a question of utmost importance for the viability of the aether theory.

It has been clear for some time now that super-critical surface magnetic fields, exceeding 4×10^{13} G, exist on a subset of neutron stars. These magnetars may harbor interior fields many orders of magnitude larger, potentially reaching equipartition values. However, the impact of these strong fields on stellar structure has been largely ignored, potentially complicating attempts to infer the high density nuclear equation of state. In this thesis, we assess the effect of these strong magnetic fields on the mass-radius relationship of neutron stars. We employ an effective field theory model for the nuclear equation of state that includes the impact of hyperons, anomalous magnetic moments, and the physics of the crust. We consider two magnetic field geometries, bounding the likely magnitude of the impact of magnetic fields: a statistically isotropic, tangled field and a force-free configuration. In both cases even equipartition fields have at most a 30% impact on the maximum mass. However, the direction of the effect of the magnetic field depends on the geometry employed - force-free fields leading to reductions in the maximum neutron star mass and radius while tangled fields increase both - challenging the common intuition in the literature on the impact of magnetic fields.

Acknowledgements

These days, it is heard often that life has no meaning other than what we manage to give it. Reflecting back at the past years, I realize I have been fortunate to have had a very meaningful time. Spending time in a lively academic environment, and being surrounded by creative people (many of whom became my friends) gave meaning to my life at a time when it was most needed.

I owe these meaningful moments, first and foremost to Niayesh Afshordi who gave me his trust at a time of vulnerability, steadily showed me his support and from whom I learned most of what I know today. With his patience, he made me comfortable asking for help when I was confused. With his humility, he allowed me not to be too intimidated by his brilliant mind and guided me on the path to scientific self-improvement. Wherever life takes me after this, I will always look back at the time I spent learning physics under his supervision with gratitude and pride.

I feel deeply indebted to Rafael Sorkin, who joined us in our weekly group meetings. Having an in-depth knowledge of vast areas of physics, which is probably due to his intense intellectual curiosity, and always seeking rigor and clarity, he often showed interest in my research and provided positive feedback. Rafael has the unique ability to reformulate even my most ignorant questions and make them sound intelligent. More importantly, in private conversations, I was lucky to receive his advice on various issues in my life and paths I can take in my future.

I came in touch with Avery Broderick in the midst of my PhD program. I learned a lot from him about neutron stars and compact objects during a reading course I took with him. Later on, I was very fortunate to continue learning from him by collaborating on a research project that became the basis of one of the chapters in this thesis. I would like to thank him for his time and all he has taught me.

In the last year, I have been extensively collaborating with Jonah Miller, a friend and fellow student at the Perimeter Institute, on a numerical relativity project on which I had been working for most of my degree. Jonah's numerical expertise proved to be extremely useful in overcoming many challenges. Together we re-wrote the code I had previously partly written. Working relentlessly, we made a lot of progress and learned a lot together. Parts of what we learned are presented in this thesis. Our collaboration is on-going and I wish it will continue in the future. A special thanks goes to his girlfriend Ale for her witty words of advice.

I would also like to thank Matthew Johnson, with whom I collaborated for a year on a numerical relativity project about the initial conditions of inflation. I learned a lot from

him about inflation in the process. Our collaboration ended with me having to take a break from my degree and I never had an occasion to return working on the project. May be one day we will finally finish that project Matt.

I am thankful to those who took time out from their busy schedules to read my thesis, mainly the members of my advisory committee, Michael Balogh (who has been following my academic journey and giving me useful advice since my MSc years), Robert Mann and Steve Weinstein. A special thanks goes to Dimitrios Psaltis who in addition to reading the thesis, is traveling to Waterloo to attend the PhD defence. Jacob Barnett, Daniel Guariento and Heidar Moradi also took time to read my thesis and provided very helpful feedback.

I am also grateful to Erik Schnetter (with whom I am collaborating), Luis Lehner, Siavash Aslanbeigi, Mehdi Saravani and Stephen Green for very helpful discussions. So many other friends have been supportive of me with their encouraging words. I will surely forget to name some but among others, I am truly grateful to Mansour Karami, Yasaman Yazdi, Anton van Niekerk, Markus Hauru, Miguel Zilhao, Richard Brito, Trevor Rempel, Faroogh Moosavian, Ravi Kunjwal, Sebastian Mizera and Frank Coronado.

I would like to say a special thanks to Judy McDonnell at the University of Waterloo and Debbie Guenther at the Perimeter Institute for their continuous support in my graduate studies.

In the end, I would like to acknowledge the two people I am most grateful to in life, my parents, Farahnaz Malekyazdi and Kaveh Kamiab. No words are enough to describe my love for them and my gratitude for all they have done for me. They are my role models and my first reasons for keeping faith and hope in this world.

In memory of my grand-mother

No day passes without missing her

Table of Contents

List of Tables

List of Figures

Chapter 1

Introduction

Among observable astrophysical objects in our universe, neutron stars are some of the most extreme and exotic. A culmination of the most abstract theoretical ideas developed since the 20th century contributes to their understanding. Rare are examples, where quantum mechanics and nuclear forces come hand in hand with general relativity, to directly affect and explain the macroscopic properties of an observable astrophysical object. Due to this, neutron stars are often regarded as phenomenological laboratories for testing the validity of theoretical models in extreme conditions, which can not be easily tested in laboratories on Earth. Not surprisingly, the observational data from neutron stars is not enough to fully constrain all theoretical models. Nevertheless, studying neutron stars is a very effective way of quantifying our unknowns about these theories. Most of this thesis is concerned with this goal, more specifically with studying the features of a modification of general relativity, called "the gravitational aether theory" in the context of neutron stars.

It is crucial to note that neutron stars are not just testing grounds for theories of extreme matter and gravity. Understanding these fascinating objects is a worthy goal on its own, as they are believed to be one of the common end states of a massive main sequence star's life. In other words, neutron stars are thought to be born when massive (but not too massive) stars die. There is believed to be of order of 10^8 neutron stars in our galaxy (most of which are undetectable on Earth due to their weak electromagnetic signals). Those neutron stars that are in binaries or that are rotating and send strong enough signals (pulsars) can be observed. Currently, there are about 2000 observed neutron stars in the Milky Way and the Magellanic clouds. Out of these stars, a small fraction, have been known to harbor strong magnetic fields, thus being dubbed "magnetars". Part of this thesis, treats questions regarding how these strong magnetic fields affect the microscopic and macroscopic properties of magnetars.

In this chapter, we start by introducing neutron stars from a theoretical point of view (Section 1.1). We present an overview of neutron star observations in Section 1.2. As studying neutron stars in the context of the gravitational aether theory is one of the main themes of this thesis, we will present reasons to go beyond general relativity and the phenomenology of the aether theory in Section 1.3. We review some of the recent literature on neutron stars in modified theories of gravity in Section 1.4. Finally, Section 1.5 will introduce the problem of incorporating strong magnetic fields in the study of neutron stars.

1.1 On Theories of Neutron Stars and The Maximum Mass

Neutron stars belong to a category of astrophysical objects called "compact objects". As the name indicates, compact objects are characterized by their high average densities. In the case of a neutron star, a mass up to about 2 $M_\odot$ (solar masses) can be concentrated in a radius of ~ 10 km's.

Compactness (a large amount of mass in a small radius) implies that the escape velocity (or surface potential) of the object is a significant fraction of the speed of light. This ratio is illustrated in Table 1.1 for the sun, white dwarfs, neutron stars and black holes (Shapiro & Teukolsky, 1983).

Object	Mass	Radius	Surface Potential (GM/Rc^2)
Sun	$M_\odot$	$R_\odot$	10^{-6}
White Dwarf	$\leq 1.4M_\odot$	$\sim 10^{-2}R_\odot$	10^{-4}
Neutron Star	$\sim 1-3M_\odot$	$\sim 10^{-5}R_\odot$	10^{-1}
Black Hole	Arbitrary	$2GM/c^2$	1

Table 1.1: Comparison of surface potentials for different astrophysical objects.

It is when the escape velocity ($v_{esc} = \sqrt{2GM/R}$) becomes a significant fraction of the speed of light that the effects of General Relativity can no more be ignored. As we see in Table 1.1, although General Relativity has small effects in the structure of the sun or white dwarfs, its effects become non-negligible in neutron stars (and of course in black holes, as they are fundamentally General Relativistic objects).

The gravity from the large amount of mass in compact objects cannot be supported against, only by thermal pressure (as is the case in ordinary stars). Neutron stars are

supported largely by the pressure of degenerate neutrons[1], while white dwarfs are supported by the pressure of degenerate electrons. In addition to quantum degeneracy pressure, the strong and weak nuclear forces also contribute to supporting neutron stars against gravity.

To summarize what was said above, two physical inputs are critical to the structure of neutron stars:

1- The microscopic model, describing the quantum degeneracy pressure, strong and weak nuclear forces. All this information can be encoded in a nuclear equation of state (EOS) giving the pressure p inside the neutron star as a function of the energy density ρ.

2- The macroscopic model, describing gravity (e.g. General Relativity).

One of the important consequences of incorporating General Relativity in the study of neutron stars is the prediction of an upper limit to their masses. The details of the nuclear physics below densities of $\sim 10^{13}$ gr/cm^3 which affect the crust of the neutron star have a small effect on this maximum mass. It is in higher nuclear densities that the physics of the nucleon-nucleon interactions and the possible exotic components at the core of neutron stars (e.g. hyperons, Bose condensate of pions or kaons, deconfined quark matter) can affect the maximum mass. In order to theoretically predict an absolute value for the maximum mass of neutron stars based on fundamental principles, without knowledge of the correct nuclear physics at the core of the star, Rhoades & Ruffini (1974) assumed the most extreme nuclear equation of state that gives the maximum mass compatible only with three conditions:

1- General Relativistic hydrostatic equilibrium.

2- Sub-luminal speed of sound ($dp/d\rho \leq 1$ in units where the speed of light $c = 1$).

3- Pressure being a monotonically non-decreasing function of density ($dp/d\rho \geq 0$).

They found that based on these principles, the most extreme equations of state predict a maximum mass of at most $\sim 3M_\odot$.

Assuming General Relativity, it is the stiffness of the nuclear equation of state that controls the maximum mass value. The introduction of non-nucleonic degrees of freedom generally softens the equation of state and reduces the maximum mass (Lattimer & Prakash, 2007). As will be the focus of this thesis, modifying General Relativity, or the existence of strong magnetic fields also affect the value of the maximum mass of neutron stars.

[1]Most of the interior of neutron stars is made of neutrons and they are effectively giant nuclei (with $\sim 10^{57}$ baryons).

This upper limit on the mass of neutron stars gives us a powerful means of testing the validity of theoretical models via the observation of very massive neutron stars. The detection of a neutron star with a mass above the maximum mass, would refute one or many of the theoretical assumptions at the basis of the maximum mass calculation (e.g. the theory of gravity or the nuclear physics). However, it is important to note that often, degeneracy exists in the outcomes of various assumptions. For example, a theory of gravity that predicts a maximum mass below the mass of a detected neutron star, can be saved assuming a stiffer nuclear equation of state, which would increase the maximum mass value. To go beyond this degenerary in the hope of more definite evaluations of the validity of models, one would require additional observables such as the radius of the neutron star. Going beyond hydrostatic equilibrium and studying other scenarios involving neutron stars such as their dynamical evolution may be another path worth considering.

As the mass measurements of neutron stars are of major importance in testing theoretical models, the next section will be a brief overview of these observations.

1.2 Observations of Massive Neutron Stars

Rotating neutron stars with strong magnetic fields (where the axis of rotation is not aligned with the magnetic dipole moment) can be observed as pulsars. The electro-magnetic pulses (originating from accelerated particles at the poles of the magnetic field) arrive at Earth with regular time intervals each time the magnetic moment is aligned with the direction of the Earth. Figure 1.1 shows a schematic representation of a pulsar. Due to the rotational stability of pulsars, one can measure with high precision the various effects that may alter the arriving times of these pulses. These kinds of measurements are called "pulsar timing". One of the effects that may alter the arriving times of the pulses is the General Relativistic Shapiro delay in binary pulsars. The Shapiro delay is caused by the fact the light pulses originating from the pulsar are slowed due to the gravitational potential of the binary companion as predicted by General Relativity. This effect was measured by Demorest et al. (2010) for the PSR J1614-2230 binary pulsar (consisting of a neutron star orbiting around a white dwarf). They fit a "timing model" to the pulse profiles that takes into account various effects such as pulsar rotation, the spin-down of the pulsar due to loss of energy in electro-magnetic waves, astrometric terms, binary orbital parameters and General Relativistic effects such as the Shapiro delay. They perform a χ^2 fit of the model to the data. The comparison of the timing residual measurements and the model prediction is shown in Figure 1.2. Based on their best-fit model, the authors calculate the mass of the white dwarf (which is responsible for the gravitational potential

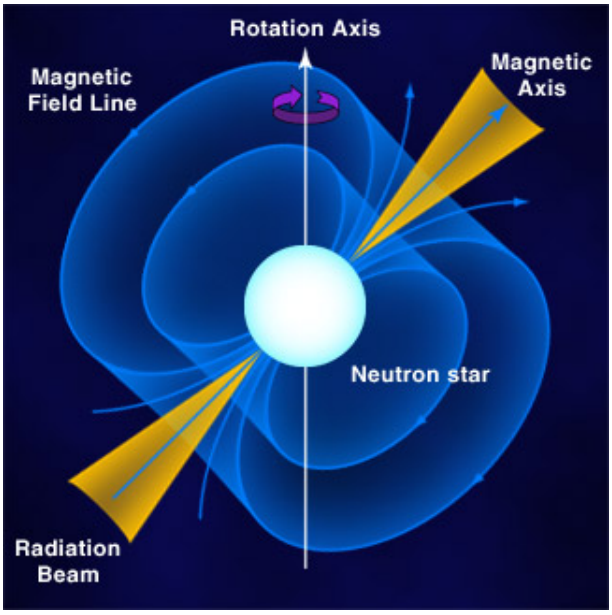

Figure 1.1: Schematic representation of a pulsar.

causing the Shapiro delay of the pulses coming from the pulsar). The white dwarf mass is 0.500 ± 0.006 $M_\odot$. The model shows the binary system to be very edge-on, with an inclination of $89.17° \pm 0.02°$. Based on Keplerian orbital physics, the model then predicts a mass of 1.97 ± 0.04 $M_\odot$ for the neutron star. This is a relatively high mass measured with very good precision, partly due to the orbit being very edge-on. As mentioned in the previous section, high mass measurements for neutron stars have the potential to refute theoretical models going into the mass-radius calculation. Figure 1.3 shows this mass measurement compared to maximum masses predicted by various nuclear equations of state assuming General Relativity (each "mass-radius relationship" is the result of calculating the mass M for which a non-rotating neutron star of a given radius R will be able to sustain hydrostatic equilibrium). Assuming General Relativity, Demorest et al. (2010) argue that any EOS that gives a mass-radius relationship that does not intersect the J1614-2230 band is ruled out by their measurement. In particular, the authors suggest that most EOS curves involving exotic matter, such as kaon condensates or hyperons, that tend to predict maximum neutron star masses well below 2.0 $M_\odot$, are therefore ruled out.[2]

Another interesting mass measurement was performed for the pulsar PSR B1957+20

[2]See Özel et al. (2010) for the implications of this mass measurement for the conditions under which a transition to quark matter in neutron-stars can occur.

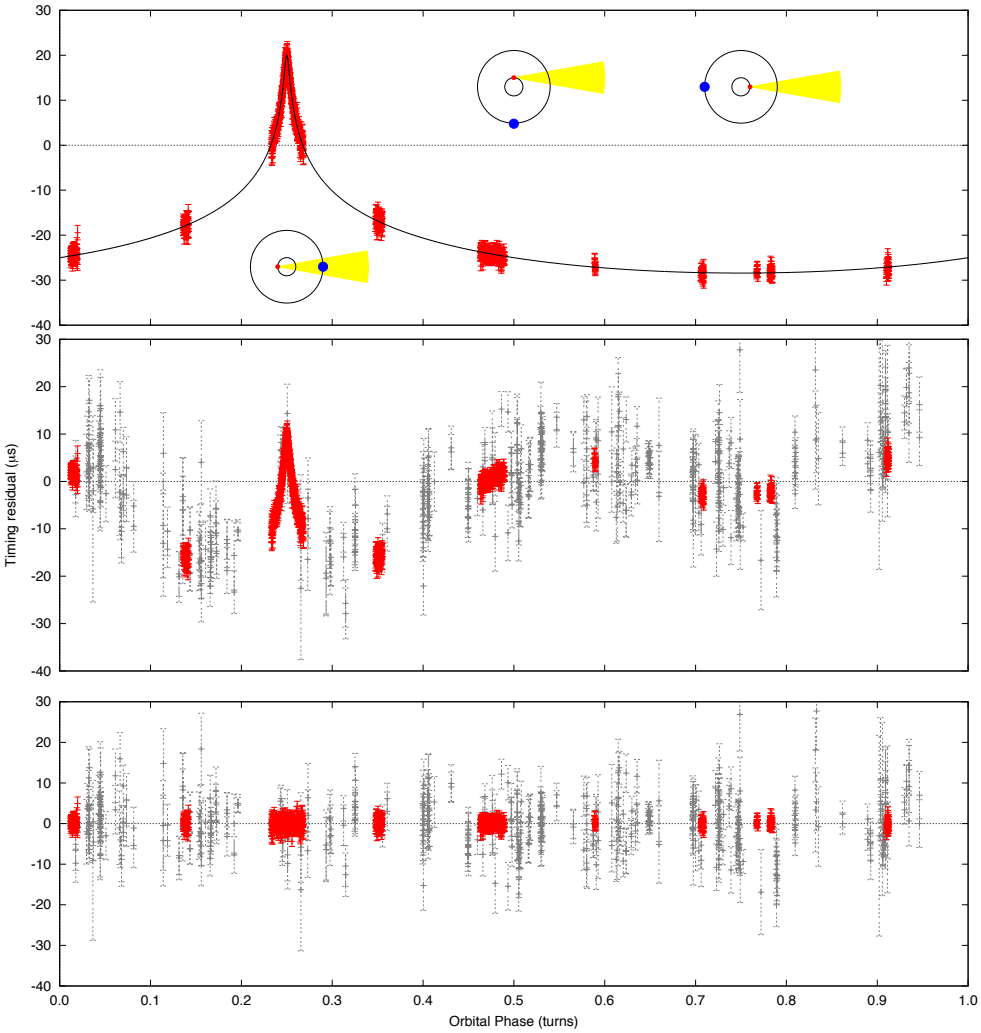

Figure 1.2: From Demorest et al. (2010). The top panel shows the Shapiro delay if it is not included in the timing model but with all other model parameters fixed at their best-fit values. The solid line shows the Shapiro delay coming from the timing model, and the red points are timing measurements from the observational data. The orbital pictures show a top-down view of the binary system at orbital phases 0.25, 0.5, and 0.75 with the red dot being the pulsar and the blue dot being the white dwarf. The middle panel is the time residual best fits coming from a timing model taking into account orbital parameters but no General Relativistic effects. The bottom panel shows the post-fit residuals for the fully relativistic timing model (including Shapiro delay).

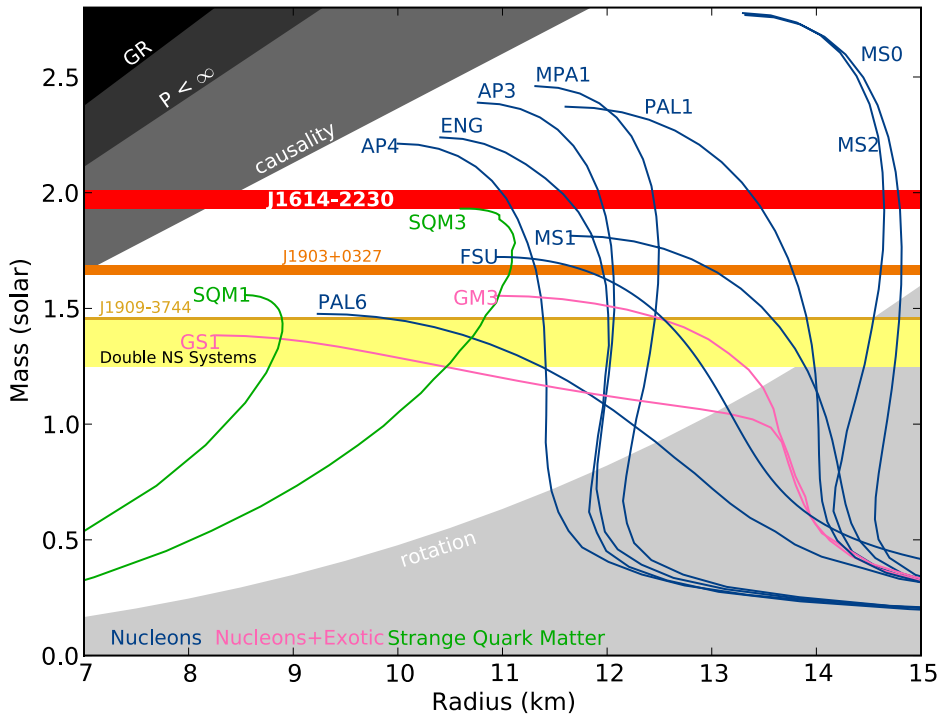

Figure 1.3: From Demorest et al. (2010). The mass-radius relationship of non-rotating neutron stars based on General Relativity and various nuclear equations of state. The horizontal bands show the observational constraint from the PSR J1614-2230 mass measurement of 1.97 ± 0.04 $M_{\odot}$, and similar measurements for two other millisecond pulsars (Jacoby et al., 2005; Freire et al., 2011), and the range of observed masses for double neutron star binaries (Lattimer & Prakash, 2007).

by van Kerkwijk et al. (2011). This pulsar is in a "black widow" binary system. Black-widow systems consist of a millisecond pulsar (a pulsar with a milli-second spin period) accompanied by a low-mass, few 0.01 $M_\odot$ white dwarf companion, which is bloated and strongly irradiated by the pulsar. The strong irradiation leads to outflows strong enough to eclipse the pulsar signal for significant fractions of the orbit. The heating caused by the irradiation on the side of the companion facing the pulsar produces strong orbital brightness variations. By studying these variations and using spectral information, the authors constrained the inclinations of the orbit, the radial velocities and derived a mass of $M = 2.40 \pm 0.12$ $M_\odot$ for the pulsar. However, this measurement happens to be dependent on the theoretical models of the light curves, and making more conservative assumptions in these models, the authors get a mass $M > 1.66$ $M_\odot$. Another black widow pulsar (PSR J1311-3430) mass measurement was made by Romani et al. (2012). This time, all the light curve models give masses $M > 2.1$ $M_\odot$.

More recently, Antoniadis et al. (2013) measured the mass of the pulsar PSR J0348+0432, by first calculating the mass of its white dwarf companion based on observational constraints (spectroscopy) combined with a theoretical finite-temperature mass-radius relation for low-mass white-dwarfs. They found a high mass of 2.01 ± 0.04 $M_\odot$ for the pulsar.

These high-mass measurements, can effectively constrain nuclear physics and the equations of state, assuming General Relativity. However, as we will see in the next section, there are reasons why considering alternative theories to General Relativity is important. Changing General Relativity may change the mass-radius relationship of neutron stars. Therefore, it is worth asking how these mass measurements can constrain or test the modifications of General Relativity.

1.3 Beyond General Relativity

The theory of General Relativity is one of the prime examples of a successful theoretical model, primarily motivated by fundamental principles, and consistent with observational data. Albert Einstein, prior to being concerned with experiments testing his theory, was motivated by the goal of constructing an elegant physical model incorporating the principle of equivalence and special relativity. Since, the theory has passed all precision tests, most of them being probes of "weak-field gravity" at intermediate scales between 1μm and 10^{11}m and therefore at intermediate energy scales (Berti et al., 2015). Deviations from General Relativity in this regime can be quantified and constrained using the parameterized post-Newtonian (PPN) formalism (Will, 2014).

Among the reasons why it is worth thinking about alternative theories of gravity, one could point to three challenges facing General Relativity:

1 - Quantum Gravity: At energy scales where the Einstein-Hilbert action for General Relativity becomes of the order of the quantum of action $\hbar$, in other words, the Planck scale $M_{PL} = \sqrt{\hbar c/G_N} \sim 1.22 \times 10^{19}$ GeV/c^2, the classical theory of gravitation fails to be predictive (e. g. singularities in cosmology and in black holes). Naive attempts at quantizing the theory of gravity have failed, due to renormalizations issues. The fact that the Planck energy scale is not currently accessible for high-energy experiments, makes it impossible to directly test the validity of models of quantum gravity. However, conceptual progress in these fields has had a valuable impact on mathematics and other fields of physics such as condensed matter (Witten, 1998; Maldacena, 1999; Aharony et al., 2000). For two approaches to quantizing gravity, namely string theory and loop quantum gravity, see Witten (2001); Ashtekar & Lewandowski (2004) and for a philosophical overview see Weinstein & Rickles (2015).

2 - The Cosmic Acceleration: Evidence from type Ia supernovae point to the fact that the expansion of the Universe is accelerating (Riess et al., 1998; Garnavich et al., 1998; Perlmutter et al., 1999). There have been a few approaches to explain this acceleration. One has been to introduce an exotic component dubbed "dark energy" among the constituents of our Universe. An example of such an energy source is a minimally coupled scalar field in Quintessence models (Ratra & Peebles, 1988; Ferreira & Joyce, 1997; Caldwell et al., 1998). Scalar-Tensor theories are also worth mentioning in the context of dark energy theories (Boisseau et al., 2000). The other approach has been to modify General Relativity in order to obtain the desired cosmological acceleration. One way to do so is with a cosmological constant. The most widely accepted cosmological model today is the ΛCDM model which assumes a cosmological constant Λ in the Einstein equations and also assumes that the matter content of the Universe is dominated by cold dark matter (a form of matter with negligible temperature and only interacting with gravity). It is important to note that the addition of such a cosmological constant with very small value, introduces fine-tuning issues which are referred to as the *new cosmological constant problem* and constitute one of the unsolved puzzles of the ΛCDM model. A few other examples of popular modifications of General Relativity include: Adding to the Einstein-Hilbert Lagrangian a function of the Ricci scalar $f(R)$ (Carroll et al., 2004; Harko et al., 2012; Capozziello et al., 2013)[3], theories coming from writing the most general Lagrangian which leads to second

[3]It is worth mentioning that the $f(R)$ theories can be written as Scalar-Tensor theories in the Einstein frame, blurring the line between dark energy and modified gravity models.

order field equations - first written down by Horndeski (1974), generalized Horndeski (G^3) theories (Gleyzes et al., 2015), Galileon theories (Chow & Khoury, 2009) and finally the massive gravity paradigm, where the graviton is modified and as if gravity is massive then it will be weaker at large scales, one can obtain the late-time cosmic acceleration (de Rham, 2014). The best astrophysical laboratories to test strong-field gravity are black holes and neutron stars whether isolated or in binary systems. As an example of using neutron stars to test the validity of $f(R)$ theories see Cooney et al. (2010) and for a review of the current bounds on some of the modified gravity models mentioned above from binary pulsar and cosmological observations, and the potential of future gravitational wave measurements see Berti et al. (2015).

3 - The Gravitational Effects of The Vacuum Energy: One of the lessons of quantum field theory is that there is an energy associated with the vacuum as the vacuum can be viewed as an infinite collection of harmonic oscillators.[4] The sum of an infinite number of ground-state energies will be obviously infinite. However, what is observable in quantum field theory is the difference in the energies. Therefore, this first type of infinity can be ignored. Other divergences then occur in quantum field theory that are regularized. The fact that quantum field theory's predictions are confirmed by accelerator experiments with high accuracy means that the results of these regularizations are correct.

The effects of ignoring the first type of infinity, however, return when one includes gravity in the calculations. One is tempted to use the usual regularization methods to deal with this infinity, and in fact these regularizations provide a finite answer to the vacuum energy. Unfortunately, this value is many orders of magnitude (~ 60) discrepant with the value that can be tolerated by cosmological equations in order for structures to appear in the Universe and ultimately in order for us to be around and ask these questions. The stress energy tensor of a field in vacuum is

$$\langle 0|T_{\mu\nu}|0\rangle = \rho_{\rm vac} g_{\mu\nu}, \tag{1.1}$$

which can be seen from the fact that the only invariant tensor in flat space-time is the metric $\eta_{\mu\nu}$, therefore the vacuum energy should be proportional to $\eta_{\mu\nu}$ and the equivalent of this in curved space-time is Eq. (1.1). Energy momentum conservation requires that $\rho_{\rm vac}$ must be a constant. As can be seen, the vacuum energy can be effectively absorbed into

[4]For experimental detections of the Casimir effect as a proof of the exsitence of vacuum energy, see Wilson et al. (2011); Fialkovsky et al. (2011); Lahteenmaki et al. (2013). However, it is worth noting that it has been claimed that Casimir effects can be formulated and Casimir forces can be computed without reference to zero point energies (Jaffe, 2005). This challenges the notion that the Casimir effect provides decisive evidence that the zero point energies of quantum fields are "real".

the cosmological constant. Therefore, this inconsistency between quantum field theory and General Relativity is referred to as the *old cosmological constant problem* and remains one of the most fundamental puzzles of modern physics.

The problem can be a sign of the failure of renormalization techniques, in which case the solution lies in new approaches in quantum field theory. However, it might also be a sign we do not understand the gravitational effects of the vacuum fluctuations in which case the solution lies in a modification of General Relativity. For a review of the problem and various approaches see Weinberg (1989); Carroll (2001); Nobbenhuis (2006); Martin (2012). The modification of General Relativity considered in this thesis (the gravitational aether theory) adresses the old cosmological constant problem. Therefore, we will introduce it in more detail in the following section.

1.3.1 The Gravitational Aether Theory

Modifying General Relativity in order for the vacuum not to gravitate is one of the main pathways to solving the old cosmological constant problem. One such modification was suggested by Afshordi (2008). He modifies the Einstein equation in the following way

$$(8\pi\mathcal{G})^{-1}G_{\mu\nu}[g_{\mu\nu}] = T_{\mu\nu} - \frac{1}{4}Tg_{\mu\nu} + \dots\,, \tag{1.2}$$

where $\mathcal{G} = 4G_N/3$ and G_N is the usual Newton's gravitational constant. By subtracting the trace of the energy momentum tensor on the right-hand side, the Einstein equation becomes insensitive to the vacuum energy density, $\rho_{\rm vac}$, where $T_{\mu\nu} = \rho_{\rm vac}g_{\mu\nu} + \text{excitations}$.[5] As energy and momentum are conserved, the divergence of $T_{\mu\nu}$ vanishes. By definition the divergence of $G_{\mu\nu}$ also vanishes through the Bianchi identities. Therefore, if one wants to subtract the trace of the energy momentum tensor, one needs to add a suitable term to it so that the divergence of the right-hand side of Eq. (1.2) vanishes. It was suggested by Afshordi (2008) that this term can be the energy momentum tensor of a perfect fluid $\mathcal{T}_{\mu\nu}$, which is dubbed "gravitational aether". With this term, Eq. (1.2) takes the form:

$$(8\pi\mathcal{G})^{-1}G_{\mu\nu}[g_{\mu\nu}] = T_{\mu\nu} - \frac{1}{4}Tg_{\mu\nu} + \mathcal{T}_{\mu\nu}, \tag{1.3}$$

[5] This is in a sense similar to unimodular gravity where the metric determinant g is not dynamical, which means the action only has to be stationary with respect to variations in the metric that keep the determinant fixed, yielding a field equation looking like Eq. (1.2). At the end of the day, unimodular gravity is equivalent to General Relativity with a cosmological constant that has nothing to do with any terms in the action or vacuum fluctuations, arising, instead, as a mere integration constant (Weinberg, 1989).

$$\mathcal{T}_{\mu\nu} = \mathcal{P}(\mathcal{U}_\mu \mathcal{U}_\nu + g_{\mu\nu}), \tag{1.4}$$

where $\mathcal{P}$ and $\mathcal{U}_\mu$ are the pressure and four-velocity of the gravitational aether. For the right hand side of Eq. (1.3) to be divergenceless, one requires

$$\mathcal{T}_\mu{}^\nu{}_{;\nu} = \frac{1}{4} T_{,\mu}. \tag{1.5}$$

It is argued by Afshordi (2008) that the pressure and four-velocity of the gravitational aether are dynamically fixed in terms of $T_{\mu\nu}$ via Eq. (1.5).

With the metric being blind to vacuum energy, the gravitational aether theory solves the old cosmological constant problem. It is interesting to point to three features of the aether theory:

1 - No action principle: The theory modifies the coupling of gravity to matter at the level of the Einstein field equations and not at the level of the action. The theory can be viewed as a low-energy effective approximation to an underlying quantum gravity action which we do not know yet, the same way the Navier-Stokes equation in fluid mechanics, which gives an effective coarse-grained description of the phase space density of particles, lacks an action, while an action principle can be written for individual particles.

2 - Lorentz violation: As for consistency reasons with cosmological constraints, the aether fluid has been chosen by Afshordi (2008) to be incompressible (zero energy density), its speed of sound is infinite. This breaks Lorentz invariance and introduces a *preferred frame* for the theory, which is the frame of the aether.

3 - No free parameters in aether: A good feature of the aether theory is that through the coupling of aether and matter given by Eq. (1.5), the aether is dynamically fixed and does not have any free parameters. This increases the predictive power of the theory and makes it harder to save the theory by fixing free parameters (as is the case in many other theories of gravity).

1.3.2 The Phenomenology of the Aether Theory

Prescod-Weinstein et al. (2009) studied static black hole solutions in the gravitational aether. They found that the pressure of aether goes to infinity at the horizon and as they found the Ricci scalar to be proportional to the pressure of aether, they establish that

any static event horizon in the gravitational aether theory coincides with a real metric singularity. As in this scenario, quantum gravity effects become important at the horizon (at the singularity), the authors postulate that aether couples the spacetime metric close to the black hole horizon, to the metric at infinity, leading to an accelerating cosmological solution, far from the horizon. This connection between the formation of stellar black holes and the acceleration of the expansion of the universe can potentially relate the solutions of the old and new cosmological constant problems, through Planck-suppressed corrections in black hole physics.

It was shown by Aslanbeigi et al. (2011) that the deviations of the aether theory from General Relativity can only be significant in situations with relativistic pressure, or (potentially) relativistic vorticity. They showed that for a perfect fluid with linear equation of state ($p \propto \rho$), the solutions to the gravitational aether theory are identical to those of General Relativity only with a renormalized gravitational constant. As the gravitational coupling is not a constant in the aether, the authors found that in the case of homogeneous FLRW cosmology, radiation energy gravitates more strongly than non-relativistic matter. The aether theory implies that gravity should be 33% stronger in the cosmological radiation era than the predictions of General Relativity.

As the increase of the gravitational constant at around the $T = \mathcal{O}(1)$ MeV epoch induces an earlier freezeout of the neutron to proton ratio because of a speed-up effect of the increased cosmic expansion, the abundance of ^{4}He increases sensitively, and the abundance of deuterium (D) increases mildly while the abundance of ^{7}Be decreases. Comparing the theoretical prediction with the observational light element abundances, the authors found that every light element abundance agrees with the gravitational aether theory within 2σ. They found notably that ^{7}Li fits the data better in the gravitational aether than in the standard big bang nucleosynthesis (which over-predicts ^{7}Li abundance by 4-5σ as calculated by Cyburt et al. (2008)). The main discrepancy found was with deuterium abundance observed in quasar absorption lines.

Aslanbeigi et al. (2011) also examined the implications for precision tests of gravity using the PPN (parametrized post-Newtonian) formalism (Will, 2006), and showed that the only PPN parameter that deviates from its General Relativistic value is ζ_4, the anomalous coupling to pressure (=1/3 for the aether and 0 for General Relativity), that has never been tested experimentally. Finally, they argued that current tests of Earth's gravito-magnetic effect mildly prefer a co-rotation of aether with matter, although they are consistent with an irrotational aether at 2σ level.

More recently, Narimani et al. (2014) have analyzed cosmological observations probing the gravity of relativistic pressure in the radiation era (Planck, WMAP and BICEP2) and

found that the best fit for anomalous pressure coupling is about half-way between General Relativity and gravitational aether and excludes both theories at around the 3σ level, while including higher resolution CMB observations ("highL") or baryonic acoustic oscillations pushes the best fit closer to General Relativity, excluding the gravitational aether theory at the 4-5σ level.

1.4 Neutron Stars and Modified Gravity

As was shown in the previous section, the gravitational aether theory is an alternative to General Relativity which makes phenomenological predictions that can be tested observationally. A theory is good only if it can make definite predictions that are consistent with current and future observational results. In astrophysical situations where gravity due to vorticity or pressure is negligible, the effects of the aether theory are indistinguishable from General Relativity (Afshordi, 2008; Aslanbeigi et al., 2011). The aether theory can be tested only in high pressures and strong gravitational forces. The interior of neutron stars satisfies these conditions. In addition pulsars can be observed and studied empirically, enabling observational tests of theoretical models. Most of this thesis (Chapters 2 and 3) is concerned with the study of neutron stars in the aether theory. In Chapter 2, we will look at the hydrostatic equilibrium configurations of non-rotating neutron stars in the aether theory. In Chapter 3, we will take on a more ambitious goal of studying the dynamics of a neutron star in the aether theory. This will require using methods from numerical relativity. In recent years, there has been a surge in studies of neutron stars in modified gravity. In the remainder of this section, we will do a short literature review of some of these studies.

Eling et al. (2007) studied the hydrostatic structure of non-rotating neutron stars in the context of the Einstein-Aether theory (a Lorentz-violating theory in which a dynamical unit time-like vector field is coupled to gravity) and found that it is fairly close to that in General Relativity, with quantitative differences. Depending on the equation of state, the maximum masses range from about 6-15% smaller than in General Relativity.

Lasky et al. (2008) solved the equations of hydrostatic equilibrium for a spherically symmetric, static distribution of a perfect fluid in Bekenstein's Tensor-Vector-Scalar (TeVeS) theory (Bekenstein, 2004). Imposing a specific polytropic equation of state allowed them to analyze the differences in neutron star structure between those appearing in General Relativity and those in TeVeS and put constraints on a coupling parameter in their model.

Kobayashi & Maeda (2008); Upadhye & Hu (2009); Babichev & Langlois (2010); Cooney et al. (2010); Santos (2012); Orellana et al. (2013); Cheoun et al. (2013); Astashenok et al.

(2013); Ganguly et al. (2014); Astashenok et al. (2014b); Momeni et al. (2015); Capozziello et al. (2015) have all studied neutron stars in $f(R)$ models. Neutron star solutions are not easy to calculate in these models because of several potentially dangerous issues, including singularities and multivaluedness in the scalar potential and a diverging effective mass for the field. The numerical challenges involved in these calculations may also serve as a motivation to develop more efficient integration methods (Berti et al., 2015). Many of these studies also aim to constrain the $f(R)$ model parameters in order for static neutron star solutions compatible with observations to exist. Pani et al. (2011a); Cisterna et al. (2015); Momeni & Myrzakulov (2015) have studied neutron stars in the context of scalar-tensor and Gauss-Bonnet gravity.

The studies mentioned so far are all constrained to hydrostatic situations. Few are numerical studies of modified gravity in dynamical situations, such as the dynamics of one neutron star or the dynamics of neutron star mergers. The latter was studied by Barausse et al. (2013) for Scalar-Tensor theories. The authors consider neutron star binaries and focus on strong-field and highly dynamical effects during the late inspiral until the merger. They show that for a class of Scalar-Tensor theories, neutron star binaries can present strong-field effects that are qualitatively different from General Relativity that may be detectable in gravitational wave experiments such as LIGO. For a recent review of probes of strong field gravity through numerical simulations see Choptuik et al. (2015).

1.5 Strongly Magnetized Neutron Stars

Observations and theoretical studies of soft gamma-ray repeaters and X-ray pulsars point to the existence of neutron stars with very high surface magnetic fields ($B > 10^{14}$ G), comprising the so-called magnetars (Duncan & Thompson, 1992; Paczynski, 1992; Thompson & Duncan, 1995, 1996; Melatos, 1999). These surface magnetic fields are inferred through the observed slowing of the stellar rotation, presumed to be a result of the emission of energy and angular momentum via large-scale magnetic fields at the light cylinder, the point beyond which they are unable to continue to rigidly rotate with the star. This is expected to spin the star down on a timescale $\approx P/\dot{P} \propto B^{-2}P^4$, where P is the spin period. Thus, magnetars are universally observed to have long periods, roughly 1 s, and thus correspondingly large light cylinders $cP/(2\pi) \approx 5 \times 10^4$ km. As a result, the implied surface fields necessarily rely on a significant extrapolation, and typically assume a dipolar magnetospheric magnetic field geometry, necessarily producing a lower limit on the surface field strength, which is itself likely to be a lower limit on the interior field strengths.

As a recent example, Gotthelf et al. (2013) monitored the temporal and spectral evo-

lution of a pulsar, originally discovered by the NuSTAR X-ray Observatory, and from the spin-down measurement, inferred a *dipole* magnetic field strength $B = 3 \times 10^{14}$ G. Magnetars can also be observed in the radio band. Follow-up observations of the pulsar PSR J1622-4950, discovered by Levin et al. (2010) in a survey of radio pulsars with the Parkes 64 m telescope, show that the pulsar has the highest inferred surface magnetic field of the known radio pulsars ($B \sim 3 \times 10^{14}$ G), making it the first magnetar discovered via its radio emission. A catalog of 26 currently known magnetars was presented recently by Olausen & Kaspi (2014).

The existence of extremely strong magnetic fields observed in magnetars can be explained by a number of processes. Neutron stars with strong magnetic dipole fields $B \sim 10^{14}$ - 10^{15} G, can form when conditions for efficient helical dynamo action are met during the first few seconds after gravitational collapse (Duncan & Thompson, 1992). In addition to differential rotation, convection may play a significant role in amplifying the magnetic field (Thompson & Duncan, 1993). However, the nonlinear saturation of these, which determines the maximum internal magnetic field strength attainable, remains highly uncertain.

Simulations of neutron star mergers that follow the evolution of the interior magnetic fields indicate that the field strengths can be amplified to values of at least 2.0×10^{15} G (Price & Rosswog, 2006) and 10^{16} G (Zrake & MacFadyen, 2013; Obergaulinger et al., 2010; Anderson et al., 2008) within the first millisecond, long before the time it takes for the neutron star remnant to collapse into a black hole. The subsequent differential rotation of the neutron star remnant will cause the field to increase further. In addition to merger simulations, simulations of the magneto-rotational instability in proto-neutron stars indicate magnetic field strength amplifications to values well in excess of 10^{15} G (Obergaulinger et al., 2009; Masada et al., 2015; Naso et al., 2008). In many simulations, equipartition with the turbulent motion, and in at least one case equipartition with the thermal energy density (Guilet & Müller, 2015), is reached. In a handful, equipartition with the rest mass energy density is implied (Price & Rosswog, 2006; Naso et al., 2008, where in the latter toroidal field strengths as high as 10^{18} G are predicted).

Nevertheless, it is important to note that numerical simulations of magnetic field growth in dynamical nuclear-density material are complicated by the extreme physical conditions present. To date no single simulation resolves all of the relevant physical scales, and often simulations focus on a subset of the relevant instabilities, evidenced by the variety of approaches taken. In no numerical study has the evolution of the magnetic field converged, with higher resolution simulations producing larger magnetic field strengths (e.g., Sawai et al., 2013; Obergaulinger et al., 2010). Thus, the present simulations can only provide *lower limits* on the strength of proto-neutron star magnetic fields.

A natural *upper limit* to proto-neutron star magnetic field strengths is given by equipartition with the gas pressure (corresponding to $B = 10^{16}$-10^{18} G), where the mechanisms responsible for the amplification of the field have certainly saturated (Price & Rosswog, 2006). That such high fields are possible is circumstantially supported by the general relativistic magneto-hydro-dynamic (GRMHD) black hole accretion flow simulations of thick disks, which are sufficiently resolved to reach a steady-state field and typically find Maxwell stresses that are of order the rest mass density, implying equipartition fields (Penna et al., 2013; Igumenshchev & Narayan, 2002).

It is far from clear that the MHD prescription is sufficient in the highly dynamical, highly magnetized proto-neutron star. In addition to the large uncertainties surrounding the equation of state, non-ideal MHD effects and vacuum polarization remain largely ignored during the initial field generation. As a result, it is unlikely that the upper limit on the interior neutron star magnetic field strength will be convincingly settled by theoretical arguments alone. That is, ultimately, the maximum attainable field strength is a question that needs to be addressed empirically, e.g. through measurements of the mass and radius of magnetars.

Therefore, one is tempted to ask how strong field strengths affect the structure of these stars. This is particularly important as the equilibrium mass and radius of neutron stars vary based on the nuclear and gravitational physics assumed (for example, see Lattimer & Prakash (2001, 2007) for the effects of various nuclear equations of state on the structure of neutron stars, and see Kamiab & Afshordi (2011); Pani et al. (2011b); Alavirad & Weller (2013) for effects of modifying general relativity). As a result, observational measurements of these masses and radii have the potential to constrain theoretical models. In particular, observing neutron stars with very high masses is useful, as each set of models (nuclear equation of state and gravitational model) predicts a maximum mass beyond which no neutron stars would exist. For example, the detection of a 1.97 ± 0.04 $M_\odot$ pulsar by Demorest et al. (2010), or the measurement of a 2.01 ± 0.04 $M_\odot$ pulsar by Antoniadis et al. (2013) have been used to significantly constrain the viable nuclear equations of state, as well as potential modifications of general relativity (Kamiab & Afshordi, 2011). Therefore, before reaching definite conclusions, it is crucial to include all the necessary physics, and in the case of magnetars, investigate how strong magnetic fields affect their mass-radius (M-R) distribution.

The presence of a strong magnetic field in a neutron star can potentially affect the mass and radius in two ways:

1. Locally, a magnetic field affects the nuclear equation of state (EOS) thus indirectly affecting the equilibrium configurations of the star.

2. The magnetic field can affect the structure of the neutron star globally by contributing to the hydrostatic support against gravity via its stress, and the structure of its spacetime via its energy (in other words, through the contribution of the Maxwell energy-momentum tensor to the Einstein equations).

Broderick et al. (2000, 2002) studied the effects of a strong magnetic field on the nuclear EOS. As part of this thesis is an extension of their studies, we will describe this magnetized nuclear EOS in more detail in Chapter 4. The EOS expresses nuclear pressure in terms of the local magnetic field strength and nuclear density. Therefore, some assumption about the structure of the magnetic field is necessary. Cardall et al. (2001) studied static neutron stars with poloidal magnetic fields and a simple class of electric current distributions consistent with the requirement of stationarity. Considering the global effect of the magnetic field stress in the Einstein equations, and assuming a set of nuclear EOS, mainly the one calculated by Broderick et al. (2000, 2002), they found that the magnetic field increases noticeably the maximum mass. In a recent study, Astashenok et al. (2014a) have considered neutron stars with strong magnetic fields (where the field strength is a simple parametric function of baryon density only) in the framework of $f(R)$ gravity. Using a nuclear EOS similar to the one calculated by Broderick et al. (2000, 2002), and assuming the global effect of the magnetic field pressure, they found that the strong magnetic field can increase considerably the maximal mass of the star. They also find that for large fields, the M-R relation differs considerably from that of general relativity only for stars with masses close to the maximal one. In another recent study, Lopes & Menezes (2014) assume a chaotic magnetic field model introducing a variable magnetic field, which depends on the energy density rather than on the baryonic density, and based on this calculate the mass radius relationship for neutron stars.

It is important to stress that in the studies of Lopes & Menezes (2014), Astashenok et al. (2014a) and Cardall et al. (2001), the magnetic field is able to provide hydrostatic support in the global sense mentioned above where the magnetic field contributes directly in pressure in the Einstein equations [for example, $P_B = B^2/8\pi$ in the case of Astashenok et al. (2014a) and $P_B = B^2/24\pi$ in the case of Lopes & Menezes (2014)]. Although the local effects of the magnetic field on the EOS should be considered in calculating the M-R relations, it is not certain whether the magnetic field can provide global hydrostatic support for the star. Using the principle of conservation of total helicity, Broderick & Narayan (2008) developed a variational principle for computing the structure of the magnetic field inside a conducting sphere surrounded by an insulating vacuum. They show that, for a fixed total helicity, the minimum energy state corresponds to a *force-free* configuration, which is generically anisotropic. If magnetic field lines rearrange to a force-free configuration in

neutron stars, then by definition, they cannot hydrostatically support the star, and thus their impact is limited to local effects on EOS.

In Chapter 4, we will study the effect of these various assumptions (in particular, the force-free model of Broderick & Narayan, 2008) on the M-R distribution of neutron stars.

Chapter 2

Hydrostatic Neutron Stars in the Gravitational Aether Theory

Two sets of models define the structure of neutron stars. First models describing gravity that is the binding force of the star, and second models describing the elementary constituents at the core of neutron stars and their repulsive forces that work against gravity and prevent the neutron star from collapsing and forming a black hole. Apart from quantum degeneracy pressure, strong nuclear interactions are the main sources of pressure inside neutron stars. Various nuclear models give different pressure-density relations (equations of state) for the interior of neutron stars. Much of the uncertainty in the study of neutron stars is due to the lack of knowledge of the correct EOS. Having the EOS and using a description of gravity we can find the mass-radius relation of neutron stars in static equilibrium. In other words, for each neutron star of a given radius, we can find the mass for which the repulsive and attractive forces cancel and ensure the hydrostatic equilibrium of the star. This mass-radius relation has a maximum mass M_{max} beyond which no neutron star would exist and only black holes could have higher masses (Lattimer & Prakash, 2007). Therefore observations of high-mass neutron stars have the potential to constrain some equations of state and rule out others. As mentioned in the Introduction, such an observation was made recently (Demorest et al., 2010). A millisecond pulsar was observed and its mass (1.97 ± 0.04 $M_\odot$) was calculated using the Shapiro delay of the pulsar light due to its companion, a half solar-mass white dwarf. The high mass of this pulsar provides a lower limit on the maximum mass of neutron stars and rules out a number of proposed equations of state (Özel et al., 2010). Another observation was reported by van Kerkwijk et al. (2011). The authors presented evidence that the black widow pulsar, PSR B1957+20, has a high mass. Their best fit pulsar mass was $\sim 2.40 \pm 0.12$ $M_\odot$. A number

of assumptions in the theoretical modelling of the pulsar contributed to the uncertainty in this number. Considering different constraints, the authors inferred a lower limit to the pulsar mass of $M > 1.66\ M_\odot$. Future observations of neutron stars will put additional constraints on the EOS.

In this chapter, we calculate the mass-radius relation predicted by the gravitational aether theory for two well-known equations of state. The first EOS (hereafter denoted FPS) was calculated by Friedman & Pandharipande (1981) and improved by Lorenz et al. (1993). This equation of state is based on variational calculations over a wide density range using a realistic nuclear hamiltonian that contains two- and three-nucleon interactions, and fits the nucleon-nucleon scattering, as well as nuclear matter data. The Skyrme model is used in the FPS equation of state. In this model, the effective interaction has the spatial character of a two-body delta function plus derivatives. The second EOS was calculated by Akmal & Pandharipande (1997) (hereafter denoted AP3). Some improvements of this calculation compared to FPS are the use of Greens function Monte Carlo (GFMC) methods in the variational theory and including two-pion exchange three-nucleon interaction and isospin symmetry breaking terms in the hamiltonian. Özel & Psaltis (2009) show that the complete mass-radius relation of neutron stars can be reproduced to high accuracy for all proposed equations of state, when the pressure of the neutron star is specified at three fiducial densities beyond the nuclear saturation density of $\rho_{\rm ns} \sim 2.7 \times 10^{14}$ g cm $^{-3}$.[1] As they have calculated these values of pressure for the FPS and AP3 equations of state, we will use their method to reproduce these two equations of state for densities higher than ρ_0 which is a parameter to be adjusted for each EOS. For densities below ρ_0 (the outer layers of the neutron star) we will use the SLy (Skyrme Lyon) equation of state calculated by Douchin & Haensel (2001). This EOS is based on the effective nuclear interaction SLy of the Skyrme type, which is useful in describing the properties of very neutron rich matter.

The structure of this chapter is as follows: In Section 2.1, we derive the equations of stellar structure for the gravitational aether theory and relate the mass predicted by the theory to the observable mass of neutron stars. In Section 2.2, we solve the equations of stellar structure for a simplistic polytropic equation of state and explain the numerical method used. In Section 2.3, we solve the equations for the realistic FPS and AP3 equations of state, find the mass-radius relation of neutron stars predicted by the gravitational aether theory and compare it to the prediction of General Relativity. An equivalent description of the problem in terms of a modified EOS will be described in Section 2.4. Section 2.5 will include a discussion and the summary of our results.

[1] For an earlier decomposition of the EOS in three polytropes with fixed density interfaces see Read et al. (2009).

2.1 The Aether Equations of Stellar Structure

As we assume a spherically symmetric static star, the metric will take the form

$$g_{\mu\nu} = \begin{pmatrix} -B(r) & 0 & 0 & 0 \\ 0 & A(r) & 0 & 0 \\ 0 & 0 & r^2 & 0 \\ 0 & 0 & 0 & r^2 \sin^2\theta \end{pmatrix},$$

with the line element being $ds^2 = g_{\mu\nu} dx^\mu dx^\nu$. With this metric and since the problem is static and isotropic the energy momentum tensor will be

$$T^\mu_\nu = \begin{pmatrix} -\epsilon(r) & 0 & 0 & 0 \\ 0 & p(r) & 0 & 0 \\ 0 & 0 & p(r) & 0 \\ 0 & 0 & 0 & p(r) \end{pmatrix},$$

where $\epsilon(r)$ and $p(r)$ are the energy density and pressure at radius r of the star. The modified Einstein equation has the form

$$(8\pi G_N)^{-1} G_{\mu\nu}[g_{\mu\nu}] = \tilde{T}_{\mu\nu}, \tag{2.1}$$

where $\tilde{T}_{\mu\nu}$ is given by

$$\tilde{T}_{\mu\nu} = (4/3)\big[T_{\mu\nu} - \frac{1}{4} T^\alpha_\alpha g_{\mu\nu} + \mathcal{P}(\mathcal{U}_\mu \mathcal{U}_\nu + g_{\mu\nu})\big]. \tag{2.2}$$

$T^\alpha_\alpha = 3p(r) - \epsilon(r)$ is the trace of the energy momentum tensor and $\mathcal{P}$ and $\mathcal{U}_\mu$ are the pressure and four-velocity of the gravitational aether. Having $\tilde{T}^\mu_\nu = g^{\mu\beta}\tilde{T}_{\beta\nu}$, where we have the Einstein summation over index β, and imposing spherical static conditions on the aether we will get

$$\tilde{T}^\mu_\nu = \begin{pmatrix} -\tilde{\epsilon}(r) & 0 & 0 & 0 \\ 0 & \tilde{p}(r) & 0 & 0 \\ 0 & 0 & \tilde{p}(r) & 0 \\ 0 & 0 & 0 & \tilde{p}(r) \end{pmatrix},$$

where

$$\begin{aligned} \tilde{\epsilon}(r) &= \epsilon(r) + p(r), \\ \tilde{p}(r) &= (1/3)\ \big[\ \epsilon(r) + p(r)\ \big] + (4/3)\ \mathcal{P}(r). \end{aligned} \tag{2.3}$$

As Eq. (2.1) is similar to the Einstein equation only with different energy density $\tilde{\epsilon}(r)$ and pressure $\tilde{p}(r)$ given by Eq. (2.3), the equations of stellar structure will be the same as in General Relativity only with these updated quantities ($\tilde{\epsilon}$ and $\tilde{p}$). Using the Ricci tensor components and writing the different spherical components of the modified Einstein equation (2.1) we will have (Weinberg, 1972)

$$R_{rr} = \frac{B''}{2B} - \frac{B'}{4B}\Big(\frac{A'}{A} + \frac{B'}{B}\Big) - \frac{A'}{rA} = -4\pi G_N\big(\tilde{\epsilon} - \tilde{p}\big)A, \tag{2.4}$$

$$R_{\theta\theta} = -1 + \frac{r}{2A}\Big(-\frac{A'}{A} + \frac{B'}{B}\Big) + \frac{1}{A} = -4\pi G_N\big(\tilde{\epsilon} - \tilde{p}\big)r^2, \tag{2.5}$$

$$R_{tt} = -\frac{B''}{2A} + \frac{B'}{4A}\Big(\frac{A'}{A} + \frac{B'}{B}\Big) - \frac{B'}{rA} = -4\pi G_N\big(\tilde{\epsilon} + 3\tilde{p}\big)B, \tag{2.6}$$

where the prime superscript denotes the derivative with respect to radius. We have omitted the $R_{\phi\phi}$ equation as it is identical to $R_{\theta\theta}$ because of the spherical symmetry. Rewriting these equations using Eq. (2.3) we get

$$\frac{B''}{2B} - \frac{B'}{4B}\Big(\frac{A'}{A} + \frac{B'}{B}\Big) - \frac{A'}{rA} = -\frac{8\pi}{3}G_N\big(\epsilon + p - 2\mathcal{P}\big)A, \tag{2.7}$$

$$-1 + \frac{r}{2A}\Big(-\frac{A'}{A} + \frac{B'}{B}\Big) + \frac{1}{A} = -\frac{8\pi}{3}G_N\big(\epsilon + p - 2\mathcal{P}\big)r^2, \tag{2.8}$$

$$-\frac{B''}{2A} + \frac{B'}{4A}\Big(\frac{A'}{A} + \frac{B'}{B}\Big) - \frac{B'}{rA} = -8\pi G_N(\epsilon + p + 2\mathcal{P})B. \tag{2.9}$$

Given our metric, the equation of hydrostatic equilibrium for p and ϵ is (Weinberg, 1972)

$$\frac{B'}{B} = -\frac{2p'}{\epsilon + p}. \tag{2.10}$$

In addition to this, the same equation holds for our updated $\tilde{\epsilon}$ and $\tilde{p}$. This equation is not independent from the modified Einstein equations and can be derived from them

$$\frac{B'}{B} = -\frac{2\tilde{p}'}{\tilde{\epsilon} + \tilde{p}} = -2\frac{(\epsilon' + p')/4 + \mathcal{P}'}{\epsilon + p + \mathcal{P}}. \tag{2.11}$$

Given the suitable boundary conditions, Equations (2.7), (2.8), (2.10) and (2.11) along with an equation of state giving $\epsilon(p)$ (the energy density of the star as a function of its pressure) are enough to find our unknowns: $A(r)$, $B(r)$, $p(r)$, $\epsilon(r)$ and $\mathcal{P}(r)$. In practice, this needs to be done numerically.

According to Prescod-Weinstein et al. (2009), the pressure in the vacuum does not vanish and is comparable to the pressure associated with dark energy. This pressure will be negligible for the calculations of neutron star structure. Therefore we can assume that pressure and energy density both vanish outside the neutron star and the metric becomes the familiar Schwarzschild metric for which at $r \geq \mathrm{R}$

$$B(r) = A^{-1}(r) = 1 - \frac{2G_N \mathrm{M(R)}}{r}, \tag{2.12}$$

where R is the radius of the neutron star and M is the observed mass of the star given by the aether theory

$$\mathrm{M(R)} = \int_0^{\mathrm{R}} \tilde{\epsilon}(r) r^2 dr d\Omega. \tag{2.13}$$

Using Eq. (2.3) this gives

$$\mathrm{M(R)} = \int_0^{\mathrm{R}} \big[\epsilon(r) + p(r)\big] r^2 dr d\Omega. \tag{2.14}$$

The purpose of this work is to find the $\mathrm{M} - \mathrm{R}$ relation for neutron stars assuming different equations of state.

2.2 Numerical Solutions for a Polytropic Equation of State

We start by solving the equations of stellar structure for a simple EOS. The polyropic equation of state is a power-law relation between pressure and matter density

$$p = K\rho^{\Gamma}. \tag{2.15}$$

The energy density is given as a function of matter density by

$$\epsilon(\rho) = \rho c^2 + \rho \int_0^{\rho} \frac{p(\rho')d\rho'}{\rho'^2}, \tag{2.16}$$

where the second term is negligible for non-relativistic matter. For neutron stars this term needs to be taken into account. If we use Eq. (2.15) to perform the integration in the second term we will get

$$\epsilon(\rho) = \rho c^2 + \frac{K\rho^{\Gamma}}{\Gamma - 1}. \tag{2.17}$$

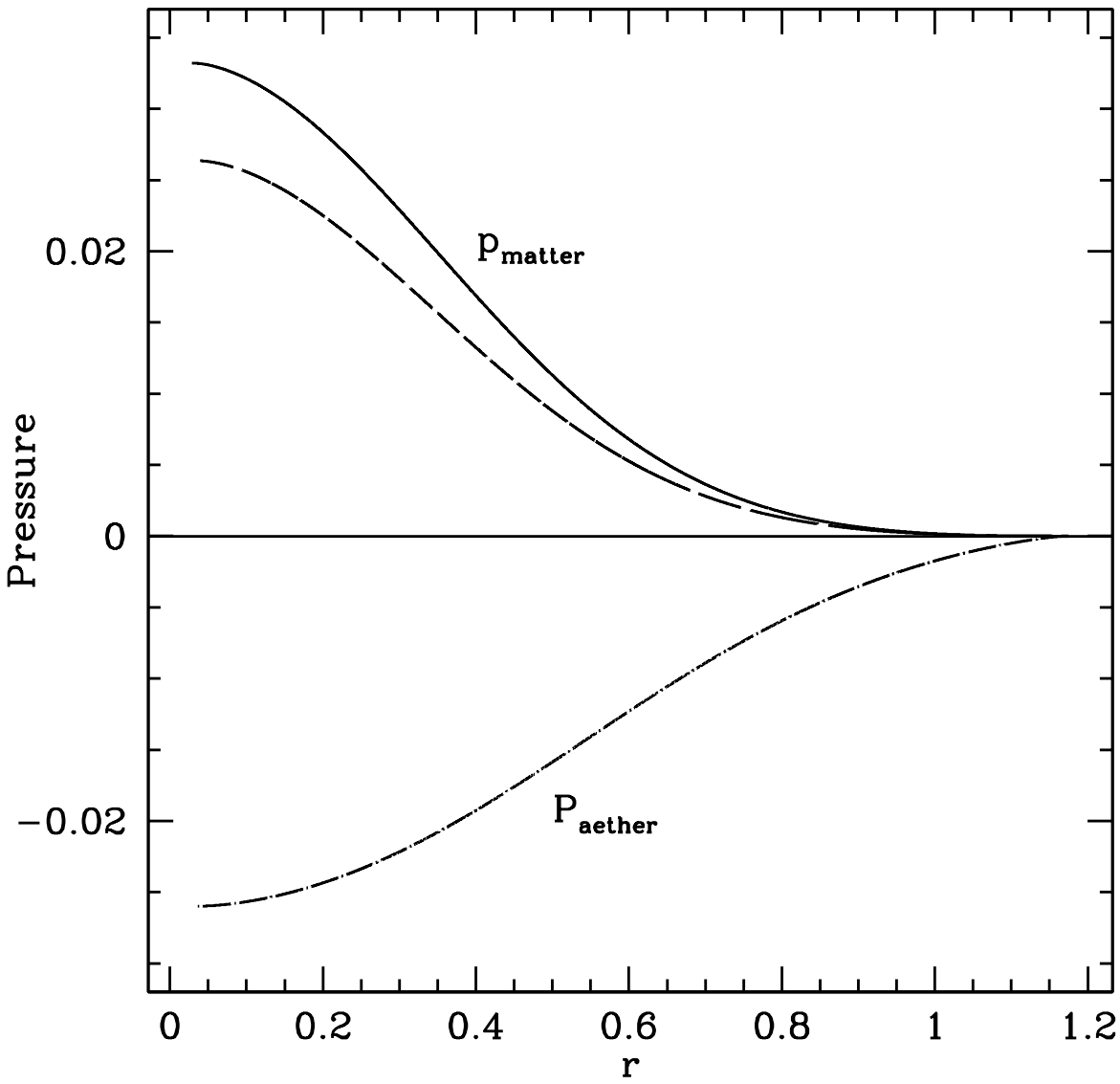

Figure 2.1: The $p(r) - r$ relation of a neutron star of radius R = 1.175 with a polytropic equation of state $p = K\rho^{\Gamma}$ where $\Gamma = 9/5$ for General Relativity (solid) and the aether theory (dashed). The pressure of the aether $\mathcal{P}(r)$ which is negative is shown as well (dashed-dotted). The units have been chosen so that $G_N = 1$, $c = 1$ and $K = 1$.

If we choose our units so that $c = 1$ and $G_N = 1$ (these will fix our time and mass units given a length unit), the energy density as a function of pressure will be

$$\epsilon(p) = (\frac{p}{K})^{\frac{1}{\Gamma}} + \frac{p}{\Gamma - 1}. \tag{2.18}$$

The differential equations (2.7), (2.8), (2.10) and (2.11) along with Eq. (2.18) need to be solved numerically. The boundary conditions are the values of $A(\mathrm{R})$, $B(\mathrm{R})$, $p(\mathrm{R})$, $\epsilon(\mathrm{R})$ and $\mathcal{P}(\mathrm{R})$ (R is the radius of the neutron star). We set the values of pressure, energy density and aether pressure equal to zero at R

$$\begin{aligned} \epsilon(\mathrm{R}) &= 0, \\ p(\mathrm{R}) &= 0, \\ \mathcal{P}(\mathrm{R}) &= 0. \end{aligned} \tag{2.19}$$

The reason why we set the pressure of the aether equal to zero at the boundary of the star is that if the pressure of the aether in the vacuum is very small at infinity it will remain small up to the boundary of the star. This can be understood by writing Eq. (2.11) in the vacuum

$$\frac{B'}{B} = -2\frac{\mathcal{P}'}{\mathcal{P}}, \tag{2.20}$$

which gives

$$\mathcal{P} = \frac{\mathcal{P}_\infty}{\sqrt{1 - 2GM/r}}. \tag{2.21}$$

If $\mathcal{P}_\infty \to 0$, then $\mathcal{P} \to 0$ at the boundary of the star. It is straight-forward to generalize this argument to dynamical situations, i.e. aether pressure vanishes in vacuum everywhere if it vanishes at large distances. Therefore, the aether does not affect the binary mass measurements, enabling us to compare our results with the current observations.

The values of $A(\mathrm{R})$ and $B(\mathrm{R})$ are given by

$$B(\mathrm{R}) = A^{-1}(\mathrm{R}) = 1 - \frac{2\mathrm{M}(\mathrm{R})}{\mathrm{R}}. \tag{2.22}$$

As we do not have the value of M(R) and finding it is the purpose of this integration, we will use a shooting method in which for a given radius R we solve the differential equations with different values of M(R) starting from R/2 to smaller values. For each value of M(R) solving the equations gives the energy density and pressure as a function of radius. Using Eq. (2.14) we can find the integrated mass $\mathcal{M}$. The value of M(R) for

which $\mathrm{M(R)} = \mathcal{M}$ is the correct mass of the neutron star of radius R. For this value the functions $A(r)$, $B(r)$, $p(r)$, $\epsilon(r)$ and $\mathcal{P}(r)$ are well-behaved and correspond to the solutions of equations (2.7), (2.8), (2.10), (2.11) and (2.18). For instance, the pressure $p(r)$ given by General Relativity and the aether theory is shown in Figure 2.1 for a neutron star of fixed radius. The integration method used is a fourth-order Runge-Kutta. Figure 2.2 shows the M(R) - R relation for neutron stars with a polytropic equation of state $p = K\rho^{\Gamma}$ with $\Gamma = 9/5$ for General Relativity and the aether theory in units for which $G_N = 1$, $c = 1$ and $K = 1$. We have chosen $\Gamma = 9/5$ as it is consistent with the constraints found by Özel & Psaltis (2009) and used by Cooney et al. (2010) to study the structure of neutron stars in $f(\mathrm{R})$ gravity theories with perturbative constraints. We see that the aether theory gives a smaller mass for a neutron star of a given radius. This was expected as gravity is stronger in the gravitational aether theory in the relativistic regime, reflected in the $\mathcal{G} = 4G_N/3$ relation. Therefore a neutron star of a given radius needs less mass to sustain its hydrostatic equilibrium compared to General Relativity.

To understand the behaviour of M(R) in large radii (the Newtonian limit) we can look at the equation of hydrostatic equilibrium in this limit

$$\rho(r)g(r) = \frac{dp(r)}{dr}, \tag{2.23}$$

where g is the gravitational force and $\rho(r) \sim \epsilon(r)$ in the Newtonian limit (as we have set $c = 1$). As $p = K\rho^{\Gamma}$ the above equation takes the form

$$-\rho\frac{M}{r^2} = (\Gamma - 1)\rho^{\Gamma-1}\frac{d\rho}{dr}. \tag{2.24}$$

We can write this as

$$-\frac{M}{r^2}dr = (\Gamma - 1)\rho^{\Gamma-2}d\rho. \tag{2.25}$$

In large radii we can treat M as constant and integrate both sides to get the following approximation

$$\frac{\mathrm{M}}{\mathrm{R}} \propto \left(\frac{\mathrm{M}}{\mathrm{R}^3}\right)^{\Gamma-1}, \tag{2.26}$$

which gives

$$\mathrm{M} \propto \mathrm{R}^{(3\Gamma-4)/(\Gamma-2)}. \tag{2.27}$$

As $\Gamma = 9/5$ here we will have $\mathrm{M} \propto \mathrm{R}^{-7}$, which is the behaviour seen in large radii in Figure 2.2.

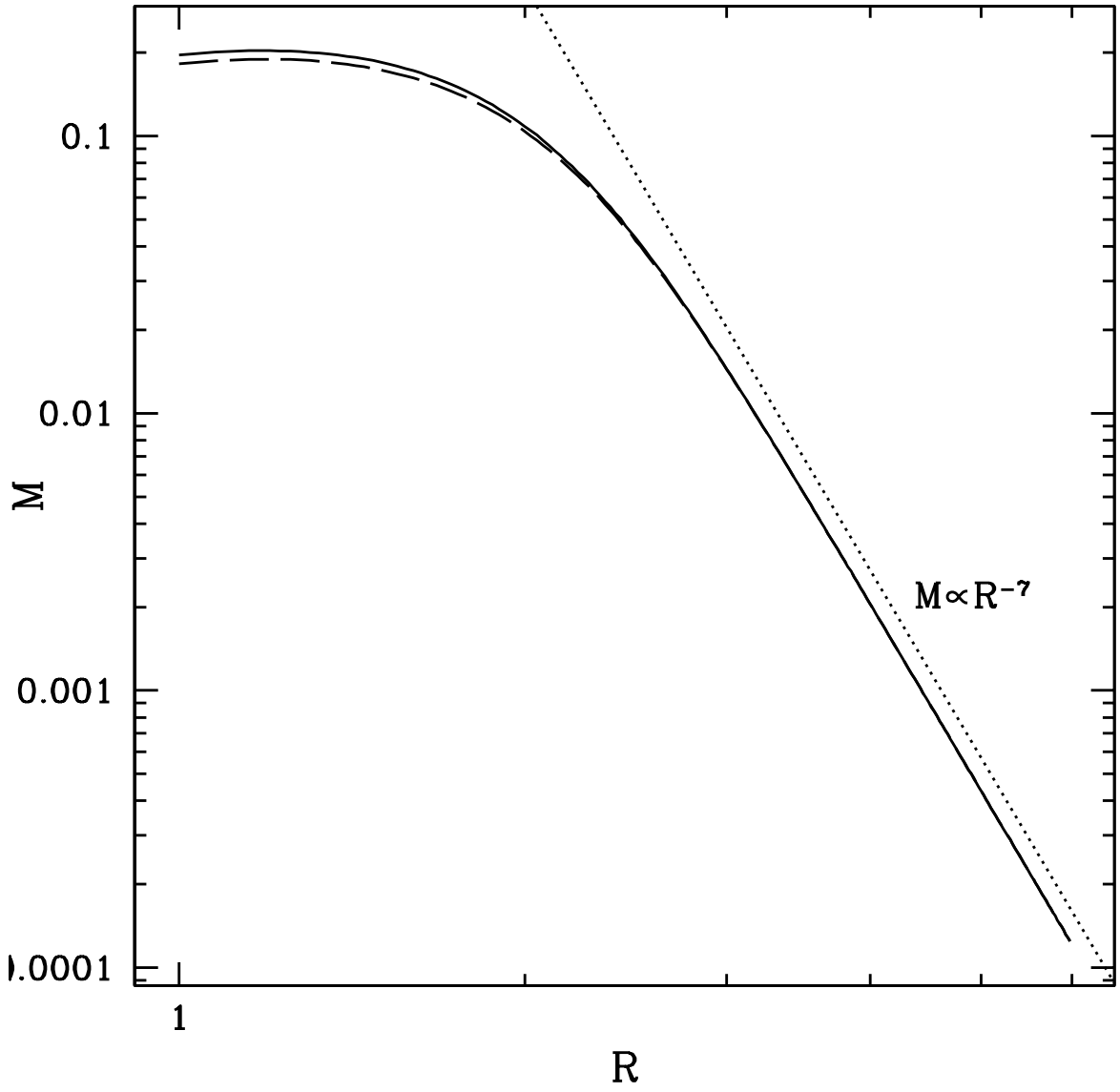

Figure 2.2: The M(R) - R relation of a neutron star with a polytropic equation of state $p = K\rho^{\Gamma}$ where $\Gamma = 9/5$ for General Relativity (solid) and the aether theory (dashed). The units have been chosen so that $G_N = 1$, $c = 1$ and $K = 1$. We see that the maximum observed mass predicted by the aether theory is less than the maximum mass predicted by General Relativity. We also see that in the Newtonian limit (large R) M(R) $\propto \mathrm{R}^{-7}$.

2.3 Numerical Solutions for Realistic Equations of State

For densities below a fiducial density ρ_0 of the order of the nuclear saturation density $\rho_{\rm ns} \sim 2.7 \times 10^{14}$ g/cm^3, the equation of state is well described by the SLy EOS (Douchin & Haensel, 2001). For densities higher than ρ_0, it is shown by Özel & Psaltis (2009) that it is sufficient to specify the pressure of the neutron star at three fiducial densities $\rho_1 = 1.85\rho_{\rm ns}$, $\rho_2 = 2\rho_1$ and $\rho_3 = 2\rho_2$ in order to reconstruct the mass-radius relations based on the AP3 and FPS equations of state. Figure 2.3 shows the SLy equation of state in $\rho < \rho_0$ as well as the parametrized AP3 and FPS equations of state in $\rho > \rho_0$ using the polytropic parameters found by Özel and Psaltis and listed in Table 2.1 (from Özel & Psaltis, 2009).

If we use the smoothed version of these two equations of state (to avoid discontinuities in the derivative of pressure as the aether theory is sensitive to these derivatives) to numerically solve the stellar structure equations in the same way we did for a polytropic EOS in Section 2.2, we find the M(R) - R relations shown in Figure 2.4. General Relativity predicts a maximum neutron star mass $M_{\rm max} \sim 1.81$ $M_\odot$ for the FPS EOS and $M_{\rm max} \sim 2.37$ $M_\odot$ for the AP3 EOS. Therefore the difference in the two parametrized equations of state (as seen by looking at the difference of the solid and dotted curves in Figure 2.3) results in a 24% difference in the maximum neutron star mass predicted by General Relativity. The aether theory gives a smaller maximum mass as expected from Section 2.2. The aether theory predicts $M_{\rm max} \sim 1.58$ $M_\odot$ for the FPS EOS and $M_{\rm max} \sim 2.00$ $M_\odot$ for the AP3 EOS.

If the FPS equation of state is refuted on the basis of the 1.97 ± 0.04 $M_\odot$ neutron star observed by Demorest et al. (2010) and if we assume the validity of the AP3 equation of state, then both the aether theory and General Relativity agree with this observational measurement. For this EOS the maximum mass predicted by the Aether theory is 16% less than the maximum mass predicted by General Relativity. However, for the AP3 EOS the aether prediction is inconsistent with the van Kerkwijk et al. (2011) measured mass, although this mass measurement is uncertain due to assumptions made in the theoretical model used in calculating the neutron star mass. As other EOS candidates exist (see Lattimer & Prakash, 2001), more measurements of the mass and radius of neutron stars are needed to put further constraints on the existing equations of state, and allow us to

EOS	$\log \rho_0$	$\log P_1$	$\log P_2$	$\log P_3$
FPS	14.30	34.283	35.142	35.925
AP3	14.30	34.392	35.464	36.452

Table 2.1: Polyropic parameters for the FPS and AP3 equations of state calculated by Özel & Psaltis (2009).

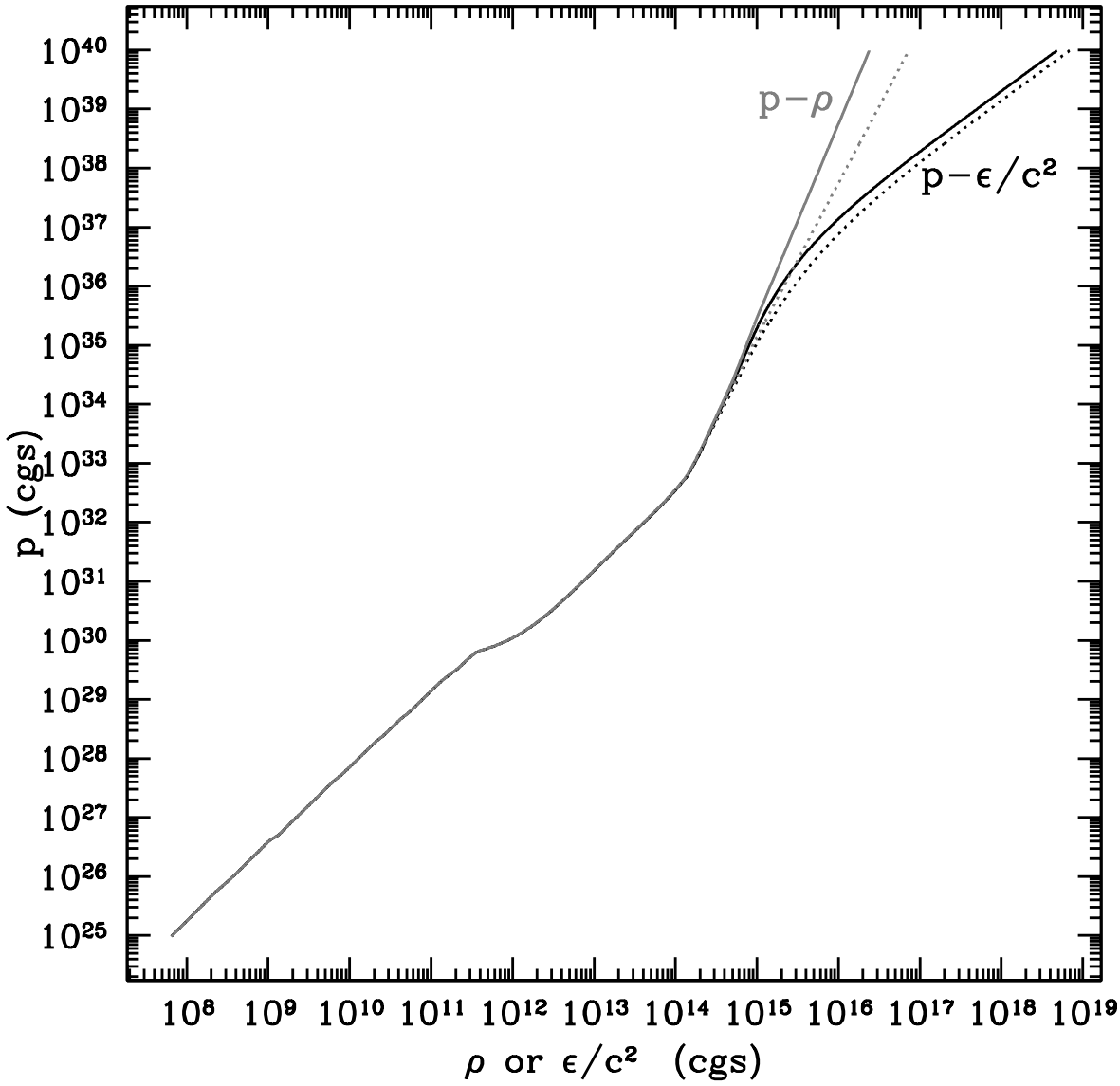

Figure 2.3: $p-\rho$ (grey) and $p-\epsilon/c^2$ (black) relations: For matter densities $\rho < \rho_0 = 10^{14.3}\mathrm{g/cm^3}$ we use the SLy EOS (Douchin & Haensel, 2001). For $\rho > \rho_0$, the solid curves show the $p-\rho$ (grey) and $p-\epsilon/c^2$ (black) relations based on the minimal representation of the AP3 equation of state using the polytropic parameters of Özel & Psaltis (2009). The dotted curves are the same relations for the FPS equation of state. The equations have been smoothed to avoid discontinuities in the derivative of pressure as the aether theory is sensitive to these derivatives.

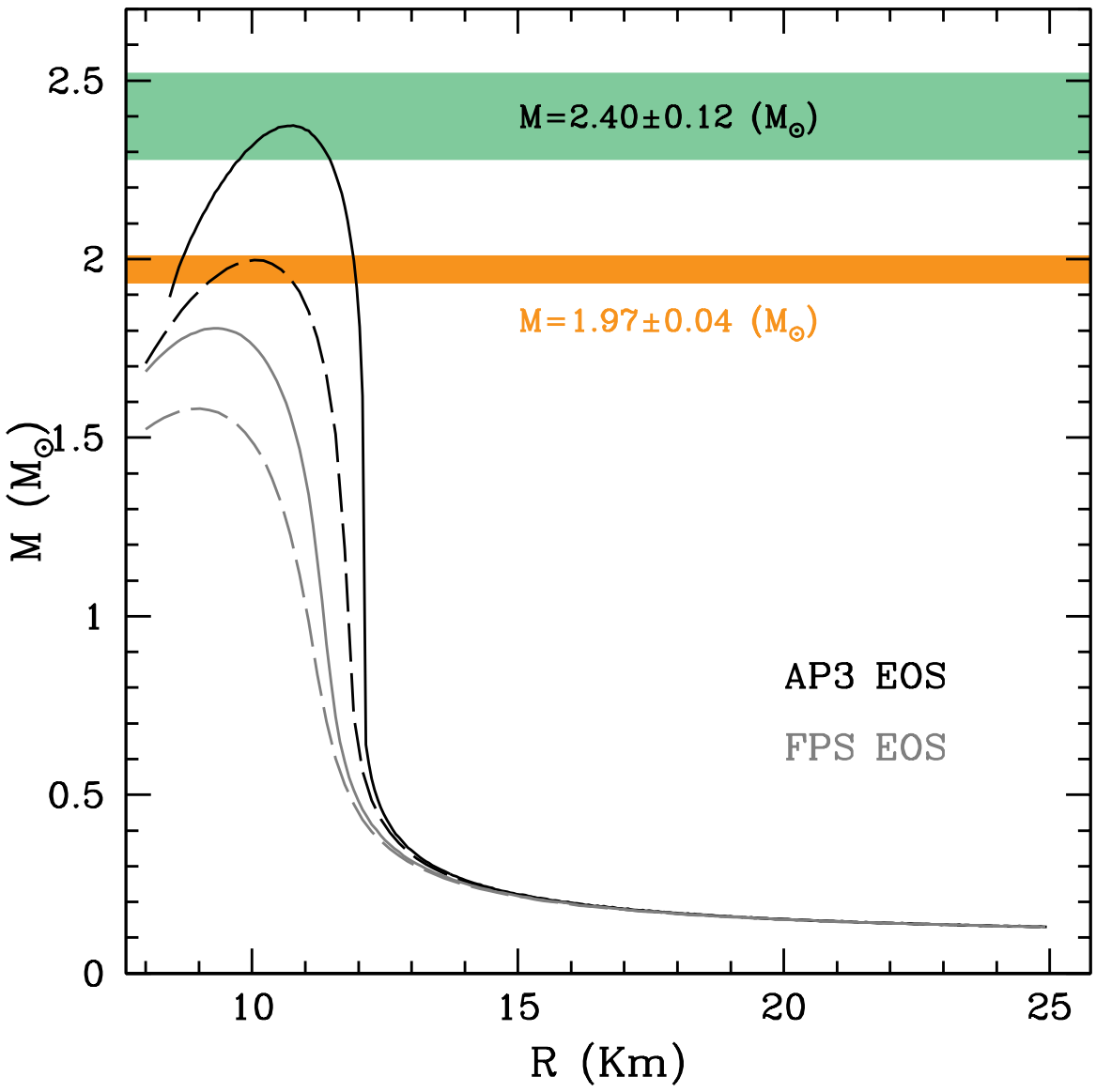

Figure 2.4: The M(R) - R relation of neutron stars given by General Relativity (solid) and the aether theory (dashed) based on the parametrized AP3 (black) and FPS (grey) equations of state. The two observed pulsar masses of Demorest et al. (2010) and van Kerkwijk et al. (2011) are shown in orange and green respectively.

make definite comparisons between the gravitational aether theory and General Relativity.

As was mentioned in Section 1.3.2, the value of ζ_4 for the aether theory is 1/3 in contrast with General Relativity ($\zeta_4 = 0$). Therefore, assuming the AP3 equation of state, the maximum neutron star masses given by the aether theory and General Relativity in Figure 2.4 can be translated into constraints on the value of ζ_4. Using a linear interpolation, we find that $\zeta_4 < 0.43$ (0.19) at 95% confidence from the Demorest et al. (2010) (van Kerkwijk et al., 2011) mass measurements.

2.4 The Aether Equation of State

An equivalent description of the problem is suggested by Eq. (2.3). This equation gives the updated energy density and pressure for which (with the new gravitational constant) the aether theory's Einstein equation (2.1) looks like the Einstein equation of General Relativity. Therefore we can describe the aether theory's prediction of the structure of the neutron star as equivalent to the one of General Relativity only with an updated equation of state given by $\tilde{p}(\tilde{\epsilon})$. To find this updated equation of state we equate the right-hand sides of equations (2.10) and (2.11) to get

$$-\frac{2p'}{\epsilon + p} = -\frac{2\tilde{p}'}{\tilde{\epsilon} + \tilde{p}}. \tag{2.28}$$

If we use Eq. (2.3) to write $\tilde{\epsilon}$ as a function of ϵ and p and if we replace the derivatives with respect to radius with derivatives with respect to ϵ we get

$$\frac{d\tilde{p}}{d\epsilon} - \frac{f(\epsilon)}{\epsilon + p(\epsilon)}\tilde{p} - f(\epsilon) = 0, \tag{2.29}$$

where $f(\epsilon) = dp(\epsilon)/d\epsilon$. Both $f(\epsilon)$ and $p(\epsilon)$ are given by the equation of state we are using. If we solve the differential Eq. (2.29) for the FPS and AP3 equations of state numerically we get $\tilde{p}$ as a function of ϵ. Using Eq. (2.3) we can find $\tilde{p}$ as a function of $\tilde{\epsilon}$. These are the dashed curves shown in Figure 2.5. The figure compares the AP3 and FPS parametric equations of state ($p-\epsilon$) and the modified equations of state ($\tilde{p}-\tilde{\epsilon}$) given by the gravitational aether theory based on the same equations of state. The effects of the aether theory become distinguishable beyond the nuclear saturation density (the region shown in Figure 2.5). As in high densities, the aether theory gives a lower pressure gradient than the one given by the equation of state, the stability of the neutron star will be obtained for a lower mass compared to the prediction of General Relativity for a neutron star of the same radius. This is why the aether mass-radius relation falls below the general relativistic mass-radius relation for neutron stars.

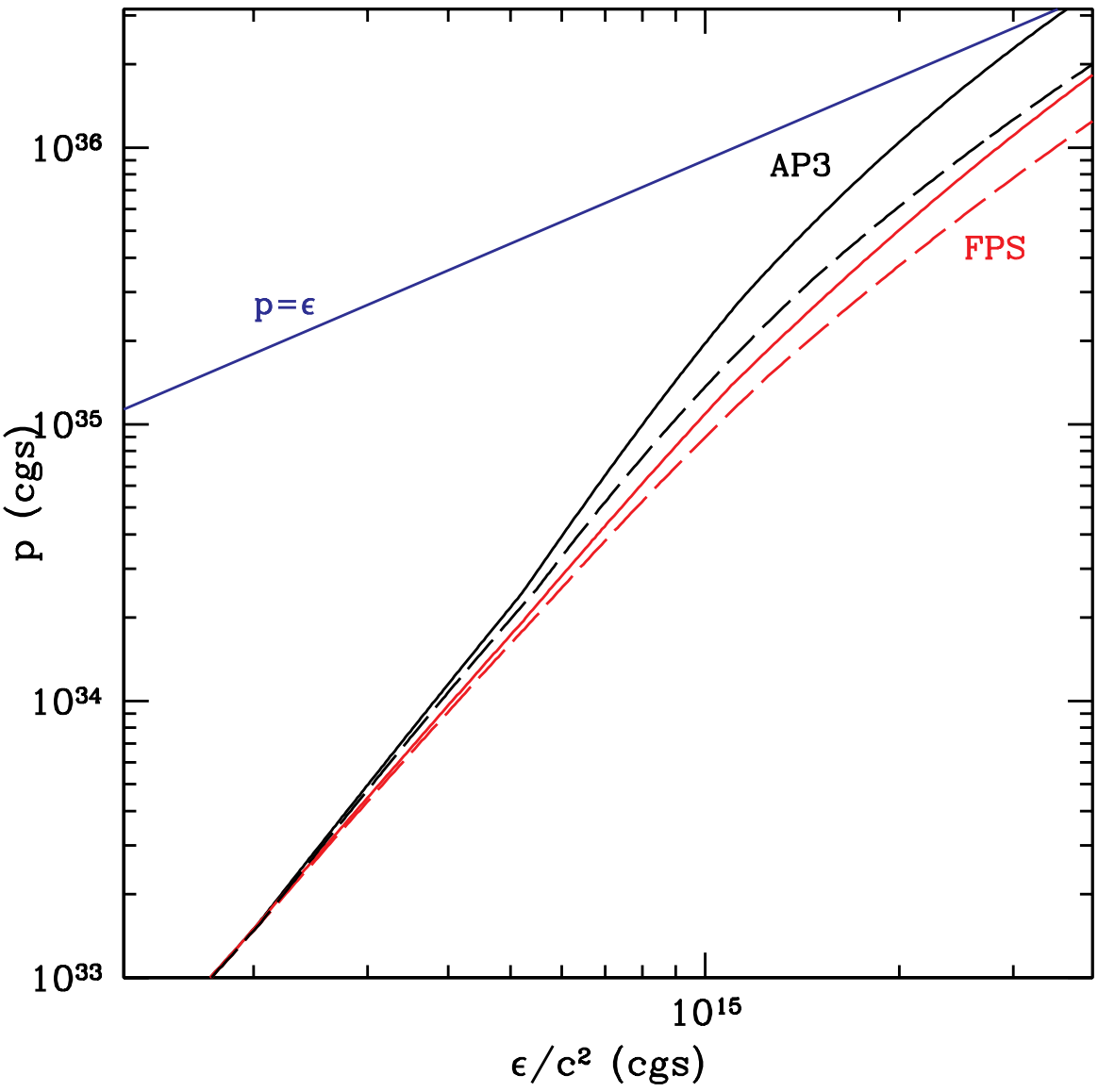

Figure 2.5: The AP3 (solid black) and FPS (solid red) parametric equations of state $p - \epsilon/c^2$ and the modified effective equations of state $\tilde{p} - \tilde{\epsilon}/c^2$ given by the gravitational aether theory based on the same equations of state (dashed black for AP3 and dashed red for FPS). The blue line corresponds to $p = \epsilon$.

2.5 Conclusions and Future Prospects

The gravitational aether theory provides a possible solution to the cosmological constant problem. The structure of neutron stars is related to their nuclear properties (the equation of state) as well as the theory describing gravity. Therefore, the aether theory can be tested in the light of mass-radius measurements of these stars. In this chapter, we solved the aether theory's equations of stellar structure for two equations of state of nuclear matter (AP3 and FPS) and found the mass-radius relation of neutron stars based on these two EOS, and compared this with the mass-radius relation given by General Relativity. The FPS equation of state gave mass-radius relations that both for General Relativity and the aether theory, were incompatible with the 1.97 ± 0.04 $M_\odot$ neutron star observed by Demorest et al. (2010). The mass-radius relations given by the aether theory and General Relativity on the basis of the AP3 equation of state were both compatible with this observation. We saw that for this equation of state the aether predicts a maximum mass that is 16% less than the maximum mass predicted by General Relativity. We also found the modified equation of state of neutron stars given by the aether theory and based on that explained why the mass-radius relation given by the aether theory falls below the one given by General Relativity. It is important to note that there are other equations of state such as the one calculated by Müller & Serot (1996)[2] that do also agree with the Demorest et al. (2010) measured pulsar mass.

In addition, including the effect of hyperons and quarks in the equation of state (e.g., Alford et al., 2005; Prakash et al., 1995; Glendenning, 1985; Balberg & Gal, 1997; Glendenning & Schaffner-Bielich, 1999; Pandharipande & Smith, 1975) can have a similar effect to the aether in lowering the maximum mass of neutron stars. For example, it is shown by Alford et al. (2005) that a hybrid (nuclear+quark matter) star can have a mass-radius relationship very similar to that predicted for a star made of purely nucleonic matter. The authors obtain hybrid stars as heavy as 2 $M_\odot$ for reasonable values of their model parameters. Due to these uncertainties in the equation of state we can not make definite comparisons between the aether theory and General Relativity at the moment.

To be able to test the aether theory more robustly, we need further constraints on the neutron star equations of state. In addition to constraints coming from the mass measurements of neutron stars (such as Demorest et al., 2010), we also need further constraints from radius measurements that are considerably harder to get. The radius of a neutron star can be measured in various ways such as the thermal observations of the surface of the neutron star, pulse profiles or redshift measurements (Lattimer & Prakash, 2007). We also

[2] And others mentioned by Lattimer & Prakash (2001).

know that mergers of compact objects such as pairs of neutron stars or neutron star-black hole pairs emit gravitational waves. These waves can be detected using current detectors if the emitter is close enough. Gravitational waves allow us to simultaneously measure masses and radii of these compact objects and could constrain the neutron star maximum mass and thus its equation of state (Lattimer & Prakash, 2007). They can also constrain the equation of state directly. Read et al. (2009) have studied the accuracy with which one can use gravitational wave observations of double neutron star inspirals to measure parameters of the neutron-star equation of state using numerical simulations. They concluded that gravitational wave observations could put a direct constraint on the EOS pressure at a rest mass density $\rho = 5 \times 10^{14}$ g cm^{-3} of $\delta p \sim 10^{32}$ dyn cm^{-2} at an effective distance $D_{\rm eff} = 100$ Mpc (also see Pannarale et al., 2011). At this density, the difference of pressure between the aether EOS and the AP3 EOS is $\Delta p = 7.6 \times 10^{32}$ dyn cm^{-2}. This means that the aether theory's modified equation of state can be tested using gravitational waves, unless its predicted pressure value at the density mentioned above, is equal to the pressure predicted by another equation of state. This degeneracy will fade if further progress is made in constraining the equation of state of nuclear matter in densities above the nuclear saturation density. Another promising way to break this degeneracy is to study the dynamics of a collapsing neutron star which could distinguish the effects of modifying gravity from modifying the equation of state.

Future observations ranging from the electromagnetic emissions of pulsars to the gravitational wave emissions of neutron stars in compact systems will allow us to learn not only about the nuclear constituents at the core of neutron stars but also about the nature of gravitation and fundamental questions such as the cosmological constant problem.

Chapter 3

Neutron Star Dynamics in the Gravitational Aether Theory

3.1 Theory

3.1.1 Preliminaries

We are interested in the dynamics of a neutron star in the gravitational aether theory. As was mentioned in the Introduction, this theory was suggested by Afshordi (2008) to adress the comsological constant problem. In this theory, the Einstein equation is modified in the following way so that the vacuum does not gravitate

$$(8\pi\mathcal{G})^{-1}G_{\mu\nu}[g_{\mu\nu}] = T_{\mu\nu} - \frac{1}{4}Tg_{\mu\nu} + \dots\ , \tag{3.1}$$

where $\mathcal{G} = 4G_N/3$ and G_N is the usual Newton's gravitational constant. By subtracting the trace of the energy momentum tensor on the right-hand side, the Einstein equation becomes insensitive to the vacuum energy density, $\rho_{\rm vac}$, where $T_{\mu\nu} = \rho_{\rm vac}g_{\mu\nu} + \text{excitations}$. As energy and momentum are conserved, the divergence of $T_{\mu\nu}$ vanishes. By definition the divergence of $G_{\mu\nu}$ also vanishes through the Bianchi identities. Therefore, if we want to subtract the trace of the energy momentum tensor, we need to add a suitable term to it so that the divergence of the right-hand side of Eq. (3.1) vanishes. It was suggested by Afshordi (2008) that this term can be the energy momentum tensor of a perfect fluid $\mathcal{T}_{\mu\nu}$, which is dubbed "gravitational aether". With this term, Eq. (3.1) takes the form

$$(8\pi\mathcal{G})^{-1}G_{\mu\nu}[g_{\mu\nu}] = T_{\mu\nu} - \frac{1}{4}Tg_{\mu\nu} + \mathcal{T}_{\mu\nu}, \tag{3.2}$$

$$\mathcal{T}_{\mu\nu} = \mathcal{P}(\mathcal{U}_\mu \mathcal{U}_\nu + g_{\mu\nu}), \tag{3.3}$$

where $\mathcal{P}$ and $\mathcal{U}_\mu$ are the pressure and four-velocity of the gravitational aether. For the right hand side of Eq. (3.5) to be divergenceless, we require

$$\mathcal{T}_\mu{}^\nu{}_{;\nu} = \frac{1}{4} T_{,\mu}. \tag{3.4}$$

Afshordi (2008) shows that the pressure and four-velocity of the gravitational aether are dynamically fixed in terms of $T_{\mu\nu}$ via Eq. (3.4). Kamiab & Afshordi (2011) have studied the hydrostatic structure of a neutron star in the gravitational aether theory. The results of this work were discussed in Chapter 2.

Generalized Aether

For the sake of comparison, we would like to generalize the aether theory, so that it could be viewed as continuously diverging from General Relativity through a parameter λ in the following way

$$(8\pi\mathcal{G})^{-1} G_{\mu\nu} = \tilde{T}_{\mu\nu} = T_{\mu\nu} - \lambda T g_{\mu\nu} + \mathcal{T}_{\mu\nu}, \tag{3.5}$$

where

$$\mathcal{G} \equiv \frac{G_N}{1-\lambda} \tag{3.6}$$

and λ goes from 0 where the theory is equivalent to General Relativity, to 1/4 (where the vacuum energy is decoupled from gravity). The equation for the conservation of aether (3.4) now becomes

$$\mathcal{T}_\mu{}^\nu{}_{;\nu} = \lambda\, T_{,\mu}. \tag{3.7}$$

We will later see that this equation implies that the pressure of aether (and thus its energy momentum tensor) vanish as expected in the general relativistic limit $\lambda = 0$. In this chapter, all equations are kept general using the parameter λ. However, wherever numerical results are shown, the value of λ has been set to 1/4 for which the aether theory solves the old cosmological constant problem. Having equations in general form, one could in principle calculate results for values of $0 < \lambda < 1/4$, which would allow a smooth transition towards General Relativity. This is left for future work.

Gauge Choice

As the aether is an incompressible fluid (its speed of sound is infinite due to its vanishing energy density), the theory breaks Lorentz invariance and introduces a preferred frame

of reference. This is the frame of the aether. This restricts our gauge freedom to the choice of the shift vector while the lapse function is determined by the frame of aether. This considerably complicates our problem, as gauge freedom is very useful in numerical relativity in order to obtain numerically well-behaved equations.

We choose the shift vector $\vec{\beta}$ to be zero. The metric in spherical symmetry can be written as

$$g_{\mu\nu} = \begin{pmatrix} -\alpha^2 & 0 & 0 & 0 \\ 0 & a^2 & 0 & 0 \\ 0 & 0 & r^2 b^2 & 0 \\ 0 & 0 & 0 & r^2 b^2 \sin^2(\theta) \end{pmatrix}.$$

In the frame of reference of the gravitational aether we have

$$n_\alpha = \mathcal{U}_\alpha = (-\alpha, 0, 0, 0). \tag{3.8}$$

where n_α is the unit vector normal to the hypersurfaces. As we will see later, the lapse function α will be determined by this choice of frame through the conservation equation for aether (3.7).

The four-velocity of the matter in spherical symmetry will be

$$u_\alpha = (u_t, u_r, 0, 0), \tag{3.9}$$

$$u^\alpha = (-\frac{u_t}{\alpha^2}, \frac{u_r}{a^2}, 0, 0). \tag{3.10}$$

As we need $u_\alpha u^\alpha = -1$, we will have

$$u_t = -\alpha\sqrt{1 + u_r^2/a^2} = -\alpha W, \tag{3.11}$$

where W is the Lorentz factor defined as

$$W \equiv \sqrt{1 + u_r^2/a^2}. \tag{3.12}$$

Equation of State of Matter

The energy-momentum tensors for matter is

$$T_{\mu\nu} = (\rho + p)(u_\mu u_\nu) + p g_{\mu\nu}, \tag{3.13}$$

where ρ is the total energy density of matter given in terms of the rest-mass density by

$$\rho = (1 + \epsilon)\rho_0, \tag{3.14}$$

where ϵ is the specific internal energy density. For many purposes, it is useful to employ a simple "Γ-law" equation of state (EOS) of the form

$$p = K\rho_0^{\Gamma}, \tag{3.15}$$

where we set $K = 1$, which alongside the Newton gravitational constant $G_N = 1$ and the speed of light $c = 1$ will fully determine the units for our problem. For this EOS we also have

$$p = (\Gamma - 1)\rho_0\epsilon. \tag{3.16}$$

The energy density is given as a function of matter density by

$$\rho(\rho_0) = \rho_0 + \rho_0 \int_0^{\rho_0} \frac{p(\rho_0')d\rho_0'}{\rho_0'^2}, \tag{3.17}$$

where the second term is negligible for non-relativistic matter. For neutron stars this term needs to be taken into account. If we use Eq. (3.15) to perform the integration in the second term we will get

$$\rho(\rho_0) = \rho_0 + \frac{\rho_0^{\Gamma}}{\Gamma - 1}. \tag{3.18}$$

The energy density as a function of pressure will be

$$\rho(p) = p^{\frac{1}{\Gamma}} + \frac{p}{\Gamma - 1}. \tag{3.19}$$

To model a stiff nuclear EOS in a neutron star, one can adopt a moderately high value of Γ in a "Γ-law" EOS, e.g., $\Gamma \approx 2$. For this problem we will choose $\Gamma = 9/5$.

Hydrodynamical Matter Equations

As the energy-momentum of the matter is conserved

$$T^{\alpha\beta}{}_{;\beta} = 0, \tag{3.20}$$

the hydrodynamical equations of the matter are the standard continuity and Euler equations which are then reformulated in a conserved form for stable numerical evolution. This conserved form is well-known and thus will not be derived and only mentioned in Section 3.1.3. However, as the aether pressure and four-velocity (in other words the lapse function, as we are in the frame of aether) are determined through the dynamics of matter (Eq. 3.7), it is necessary to find the time evolution of the energy density and velocity of matter via solving the Euler and continuity equations.

Looking at the energy momentum conservation of matter in the direction of the flow of matter (contracting with u_α), we will have

$$u_\alpha T^{\alpha\beta}{}_{;\beta} = -\rho_{,\alpha} u^\alpha - (\rho + p)\ u^\beta{}_{;\beta} = 0. \tag{3.21}$$

This gives us the continuity equation for matter

$$\rho_{,\alpha} u^\alpha + (\rho + p)\ u^\beta{}_{;\beta} = 0. \tag{3.22}$$

The divergence of the four-velocity can be written as a function of the metric determinant

$$u^\beta{}_{;\beta} = \frac{1}{\sqrt{-g}} (\sqrt{-g}\ u^\beta)_{,\beta}, \tag{3.23}$$

where $\sqrt{-g} = \alpha a r^2 b^2 \sin^2(\theta)$. Rewriting Eq. (3.22) based on (3.23) and expanding, we will have

$$\rho_{,t} u^t + \rho_{,r} u^r + \frac{\rho + p}{\alpha a r^2 b^2 \sin^2(\theta)} \left[\alpha a r^2 b^2 \sin^2(\theta)\ u^t\right]_{,t} + \frac{\rho + p}{\alpha a r^2 b^2 \sin^2(\theta)} \left[\alpha a r^2 b^2 \sin^2(\theta)\ u^r\right]_{,r} = 0. \tag{3.24}$$

As $u^t = W/\alpha$, we will have

$$\rho_{,t} u^t + \rho_{,r} u^r + \frac{\rho + p}{\alpha a r^2 b^2 \sin^2(\theta)} \left[\cancel{\alpha} a r^2 b^2 \sin^2(\theta)\ \frac{W}{\cancel{\alpha}}\right]_{,t} + \frac{\rho + p}{\alpha a r^2 b^2 \sin^2(\theta)} \left[\alpha a r^2 b^2 \sin^2(\theta)\ u^r\right]_{,r} = 0. \tag{3.25}$$

Taking the time derivative in the third term and leaving the rest untouched

$$\rho_{,t} u^t + \rho_{,r} u^r + (\rho + p)\left(\frac{W\ a_{,t}}{\alpha\ a} + \frac{2W\ b_{,t}}{\alpha\ b} + \frac{W_{,t}}{\alpha}\right) + \frac{\rho + p}{\alpha a r^2 b^2} \left(\alpha a r^2 b^2\ u^r\right)_{,r} = 0. \tag{3.26}$$

Based on the definition of W (Eq. 3.12)

$$W_{,t} = \frac{\partial W}{\partial u_r} u_{r\,,t} + \frac{\partial W}{\partial a} a_{,t}, \tag{3.27}$$

which simplifies to

$$W_{,t} = \frac{u_r\ u_{r,t}}{W a^2} - \frac{{u_r}^2\ a_{,t}}{W a^3}. \tag{3.28}$$

As will be mentioned in Section 3.1.2, we know from the evolution equations for the induced metric that

$$\frac{a_{,t}}{a} = -\alpha K^r_r, \tag{3.29}$$

$$\frac{b_{,t}}{b} = -\alpha K^{\theta}_{\theta}, \tag{3.30}$$

where K^r_r and K^θ_θ are components of the extrinsic curvature in spherical symmetry. Using equations (3.28), (3.29) and (3.30) to simplify Eq. (3.26), we get

$$\rho_{,t}u^t+\rho_{,r}u^r+(\rho+p)\big(-WK^r_r-2WK^\theta_\theta+\frac{K^r_r{u_r}^2}{Wa^2}+\frac{u_r\ u_{r,t}}{W\alpha a^2}\big)+\frac{\rho+p}{\alpha ar^2b^2}\big(\alpha ar^2b^2\ u^r\big)_{,r}=0. \tag{3.31}$$

We can write the above equation as

$$\mathcal{A}\ \rho_{,t}+\mathcal{B}\ u_{r,t}+\mathcal{C}=0, \tag{3.32}$$

where

$$\mathcal{A} = u^t=\frac{W}{\alpha}, \tag{3.33}$$

$$\mathcal{B} = \frac{(\rho+p)\ u_r}{W\alpha a^2}, \tag{3.34}$$

$$\mathcal{C} = \rho_{,r}u^r+(\rho+p)\big(-WK^r_r-2WK^\theta_\theta+\frac{K^r_r{u_r}^2}{Wa^2}\big)+\frac{\rho+p}{\alpha ar^2b^2}\big(\alpha ar^2b^2\ u^r\big)_{,r}. \tag{3.35}$$

Now if we contract the energy-momentum conservation equation normal to u_α, we get the Euler equation for the matter

$$(\delta^\alpha_\lambda+u^\alpha u_\lambda)\ T^{\lambda\beta}{}_{;\beta}=0\rightarrow(\rho+p)\ u^\alpha{}_{;\beta}\ u^\beta+p_{,\beta}\ u^\beta\ u^\alpha+p_{,}{}^\alpha=0. \tag{3.36}$$

Writing the r component of this equation in spherical symmetry and noting that $p_{,}{}^r=g^{rr}p_{,r}=p_{,r}/a^2$, we have

$$(\rho+p)\big(u^r{}_{,t}\ u^t+u^r{}_{,r}\ u^r\big)+p_{,t}u^tu^r+p_{,r}(u^r)^2+\frac{p_{,r}}{a^2}=0. \tag{3.37}$$

Writing the covariant derivatives in terms of the connections

$$(\rho+p)\Big[\big(u^r{}_{,t}+\Gamma^r_{tt}u^t+\Gamma^r_{tr}u^r\big)\ u^t+\big(u^r{}_{,r}+\Gamma^r_{rt}u^t+\Gamma^r_{rr}u^r\big)\ u^r\Big]+p_{,t}u^tu^r+p_{,r}(u^r)^2+\frac{p_{,r}}{a^2}=0, \tag{3.38}$$

where

$$\Gamma^r_{tt} = \frac{\alpha\alpha_{,r}}{a^2}, \tag{3.39}$$

$$\Gamma^r_{rt} = \frac{a_{,t}}{a}=-\alpha K^r_r, \tag{3.40}$$

$$\Gamma^r_{rr} = \frac{a_{,r}}{a}, \tag{3.41}$$

As $u^r = u_r/a^2$, we have

$$u^r{}_{,t} = \frac{u_{r,t}}{a^2} - \frac{2u_r a_{,t}}{a^3} = \frac{u_{r,t}}{a^2} + \frac{2u_r \alpha K^r_r}{a^2}. \tag{3.42}$$

If the pressure is given by an equation of state $p(\rho)$, we have

$$\begin{aligned} p_{,t} &= \frac{\partial p}{\partial \rho}\rho_{,t}, \\ p_{,r} &= \frac{\partial p}{\partial \rho}\rho_{,r}. \end{aligned} \tag{3.43}$$

Based on (3.42) and (3.43), we can simplify Eq. (3.38) as

$$\mathcal{L}\ \rho_{,t} + \mathcal{Q}\ u_{r,t} + \mathcal{S} = 0, \tag{3.44}$$

where

$$\mathcal{L} = \frac{\partial p}{\partial \rho} u^t u^r, \tag{3.45}$$

$$\mathcal{Q} = (\rho + p)\frac{u^t}{a^2}, \tag{3.46}$$

$$\mathcal{S} = (\rho + p)\Big[\frac{2u_r W K^r_r}{a^2} + \Gamma^r_{tt}(u^t)^2 + 2\Gamma^r_{tr}u^r u^t + \Gamma^r_{rr}(u^r)^2 + u^r{}_{,r}u^r\Big] + p_{,r}(u^r)^2 + \frac{p_{,r}}{a^2}. \tag{3.47}$$

Based on equations (3.32) and (3.44), we can solve for $\rho_{,t}$ and $u_{r,t}$

$$\rho_{,t} = \frac{\mathcal{B}\mathcal{S} - \mathcal{C}\mathcal{Q}}{\mathcal{A}\mathcal{Q} - \mathcal{L}\mathcal{B}}, \tag{3.48}$$

$$u_{r,t} = \frac{\mathcal{L}\mathcal{C} - \mathcal{A}\mathcal{S}}{\mathcal{A}\mathcal{Q} - \mathcal{L}\mathcal{B}}. \tag{3.49}$$

We can seperate the α dependences in $\mathcal{A}$, $\mathcal{B}$, $\mathcal{C}$, $\mathcal{Q}$, $\mathcal{L}$ and $\mathcal{S}$ as follows

$$\begin{aligned} \mathcal{A} &= \mathcal{A}_0/\alpha, \\ \mathcal{B} &= \mathcal{B}_0/\alpha, \\ \mathcal{Q} &= \mathcal{Q}_0/\alpha, \\ \mathcal{L} &= \mathcal{L}_0/\alpha, \\ \mathcal{C} &= \mathcal{C}_\alpha + \mathcal{C}_0, \\ \mathcal{S} &= \mathcal{S}_\alpha + \mathcal{S}_0, \end{aligned} \tag{3.50}$$

where

$$
\begin{aligned}
\mathcal{A}_0 &= W, \qquad (3.51)\\
\mathcal{B}_0 &= \frac{(\rho+p)\ u_r}{Wa^2},\\
\mathcal{Q}_0 &= \frac{(\rho+p)\ W}{a^2},\\
\mathcal{L}_0 &= W\ \frac{\partial p}{\partial \rho}\ \frac{u_r}{a^2},\\
\mathcal{C}_0 &= \frac{\rho+p}{ar^2b^2}(ar^2b^2\ u^r)_{,r} + \rho_{,r}u^r + (\rho+p)\big(-WK^r_r - 2WK^\theta_\theta + \frac{K^r_r {u_r}^2}{a^2W}\big),\\
\mathcal{S}_0 &= (\rho+p)\Big[\frac{2u_rWK^r_r}{a^2} - 2K^r_rWu^r + \Gamma^r_{rr}(u^r)^2 + {u^r}_{,r}\ u^r\Big] + p_{,r}(u^r)^2 + \frac{p_{,r}}{a^2},\\
\mathcal{C}_\alpha &= (\rho+p)\ u^r\ \frac{\alpha_{,r}}{\alpha},\\
\mathcal{S}_\alpha &= (\rho+p)\ \Gamma^r_{tt}\ (u^t)^2 = (\rho+p)\frac{\alpha\alpha_{,r}}{a^2}\frac{W^2}{\alpha^2} = (\rho+p)\frac{W^2}{a^2}\frac{\alpha_{,r}}{\alpha}
\end{aligned}
$$

where for writing $\mathcal{S}_0$ we have used the fact that $\Gamma^r_{tr} == a_{,t}/a = -\alpha K^r_r$. Now if we rewrite (3.48) in terms of (3.50), we get

$$
\begin{aligned}
\rho_{,t} &= \frac{(\mathcal{B}_0/\alpha)(\mathcal{S}_0+\mathcal{S}_\alpha) - (\mathcal{Q}_0/\alpha)(\mathcal{C}_0+\mathcal{C}_\alpha)}{(\mathcal{A}_0\mathcal{Q}_0/\alpha^2) - (\mathcal{L}_0\mathcal{B}_0/\alpha^2)},\\
\rho_{,t} &= \frac{(\mathcal{B}_0\mathcal{S}_0 - \mathcal{Q}_0\mathcal{C}_0) + (\mathcal{B}_0\mathcal{S}_\alpha - \mathcal{Q}_0\mathcal{C}_\alpha)}{\mathcal{A}_0\mathcal{Q}_0 - \mathcal{L}_0\mathcal{B}_0}\ \alpha. \qquad (3.52)
\end{aligned}
$$

Now we show that $\mathcal{B}_0\mathcal{S}_\alpha - \mathcal{Q}_0\mathcal{C}_\alpha = 0$

$$
\begin{aligned}
\mathcal{B}_0\mathcal{S}_\alpha - \mathcal{Q}_0\mathcal{C}_\alpha &= \frac{(\rho+p)u_r}{a^2W}\ (\rho+p)\ \frac{W^2}{a^2}\ \frac{\alpha_{,r}}{\alpha} - \frac{(\rho+p)W}{a^2}\ (\rho+p)\ u^r\frac{\alpha_{,r}}{\alpha} \qquad (3.53)\\
&= \frac{\alpha_{,r}}{\alpha}(\rho+p)^2\Big(\frac{u_rW^2}{a^4W} - \frac{Wu^r}{a^2}\Big) \qquad (3.54)\\
&= \frac{\alpha_{,r}}{\alpha}(\rho+p)^2\Big(\frac{\cancel{u_rW}}{\cancel{a^4}} - \frac{\cancel{W}\ \cancel{u_r}}{\cancel{a^2}\ a^2}\Big) = 0. \qquad (3.55)
\end{aligned}
$$

Therefore $\rho_{,t}$ can be written as

$$
\rho_{,t} = \frac{\mathcal{B}_0\mathcal{S}_0 - \mathcal{Q}_0\mathcal{C}_0}{\mathcal{A}_0\mathcal{Q}_0 - \mathcal{L}_0\mathcal{B}_0}\ \alpha = \Omega_0\ \alpha, \qquad (3.56)
$$

where

$$
\Omega_0 \equiv \frac{\mathcal{B}_0\mathcal{S}_0 - \mathcal{Q}_0\mathcal{C}_0}{\mathcal{A}_0\mathcal{Q}_0 - \mathcal{L}_0\mathcal{B}_0}. \qquad (3.57)
$$

The Aether Pressure

As we saw in Eq. (3.7)

$$\mathcal{T}^{\alpha\beta}{}_{;\beta} = \lambda T^{\alpha}_{,}. \tag{3.58}$$

As $\mathcal{T}_{\alpha\beta}$ is given by Eq. (3.13), the left side of (3.58) contracted with $\mathcal{U}_\alpha$ can be written as

$$\mathcal{U}_\alpha \mathcal{T}^{\alpha\beta}{}_{;\beta} = -\mathcal{P}\, \mathcal{U}^{\beta}{}_{;\beta}, \tag{3.59}$$

where the divergence of the four-velocity of the aether can be written as

$$\mathcal{U}^{\beta}{}_{;\beta} = \frac{1}{\sqrt{-g}}(\sqrt{-g}\, \mathcal{U}^{\beta})_{,\beta}. \tag{3.60}$$

As $\mathcal{U}_\alpha = (-\alpha, 0, 0, 0)$ and $\sqrt{-g} = \alpha a r^2 b^2$

$$\mathcal{U}^{\beta}{}_{;\beta} = \frac{1}{\alpha}(\frac{a_{,t}}{a} + 2\frac{b_{,t}}{b}) = -K^r_r - 2K^\theta_\theta. \tag{3.61}$$

Therefore Eq. (3.59) simplifies to

$$\mathcal{U}_\alpha \mathcal{T}^{\alpha\beta}{}_{;\beta} = \mathcal{P}\ (K^r_r + 2K^\theta_\theta), \tag{3.62}$$

The right side of (3.58) contracted with $\mathcal{U}_\alpha$ can be written as

$$\lambda\, \mathcal{U}_\alpha\ T^{\alpha}_{,} = \lambda\, \mathcal{U}_t\ T^{t}_{,} = -\lambda\ \alpha\ g^{tt}\ T_{,t} = \lambda\alpha(3p_{,t} - \rho_{,t}) = \lambda\alpha(3\frac{\partial p}{\partial \rho} - 1)\rho_{,t}. \tag{3.63}$$

Equations (3.58), (3.62) and (3.63) result in

$$\mathcal{P}\ (K^r_r + 2K^\theta_\theta) = \lambda\alpha(3\frac{\partial p}{\partial \rho} - 1)\rho_{,t}. \tag{3.64}$$

Therefore

$$\mathcal{P} = \lambda\ \frac{3\frac{\partial p}{\partial \rho} - 1}{K^r_r + 2K^\theta_\theta}\ \frac{\rho_{,t}}{\alpha}. \tag{3.65}$$

As $\rho_{,t}$ is given by (3.56) we have

$$\begin{aligned} \mathcal{P} &= \lambda\ \frac{3\frac{\partial p}{\partial \rho} - 1}{K^r_r + 2K^\theta_\theta}\ \frac{\Omega_0\ \cancel{\alpha}}{\cancel{\alpha}} \\ &= \lambda\ \Omega_0\ (3\frac{\partial p}{\partial \rho} - 1)\ \frac{1}{K^r_r + 2K^\theta_\theta}. \end{aligned} \tag{3.66}$$

$$\boxed{\mathcal{P} = \lambda\ (3\frac{\partial p}{\partial \rho} - 1)\ \frac{\Omega_0}{K}} \tag{3.67}$$

where $K = K^r_r + 2K^\theta_\theta$ is the trace of the extrinsic curvature. As we see in Eq. (3.67), $\mathcal{P}$ is given as an "algebraic" function of the spatial parameters of the hypersurface and does not depend explicitly on the lapse function α. In other words we do not have an evolution equation for $\mathcal{P}$ and its evaluated value can be used to calculate the lapse function.

The Lapse Function

Finally we can contract Eq. (3.58) perpendicular to $\mathcal{U}_\alpha$

$$(\delta^\alpha_\lambda + \mathcal{U}^\alpha \mathcal{U}_\lambda)\mathcal{T}^{\lambda\beta}{}_{;\beta} = \lambda(\delta^\alpha_\lambda + \mathcal{U}^\alpha \mathcal{U}_\lambda)T^{,\lambda}_{,}. \tag{3.68}$$

In the radial direction, we have

$$\begin{aligned}
(\delta^r_\lambda + \cancel{\mathcal{U}^r}\mathcal{U}_\lambda)\mathcal{T}^{\lambda\beta}{}_{;\beta} &= \lambda\ (\delta^r_\lambda + \cancel{\mathcal{U}^r}\mathcal{U}_\lambda)\ T^{,\lambda}_{,} \\
\mathcal{T}^{r\beta}{}_{;\beta} &= \lambda\ T^{,r}_{,} \\
(\mathcal{P}U^r\mathcal{U}^\beta + \mathcal{P}g^{r\beta})_{;\beta} &= \lambda\ g^{rr}\ T_{,r} \\
\mathcal{P}_{,t}\ \mathcal{U}^t\ \cancel{\mathcal{U}^r} + \mathcal{P}\ \cancel{\mathcal{U}^r}\ \mathcal{U}^\beta{}_{;\beta} + \mathcal{P}\ \mathcal{U}^\beta\ \mathcal{U}^r{}_{;\beta} + \mathcal{P}_{,r}\ g^{rr} &= \lambda\ g^{rr}\ (3p_{,r} - \rho_{,r}) \\
\mathcal{P}\ \mathcal{U}^t\ \mathcal{U}^r{}_{;t} + \frac{\mathcal{P}_{,r}}{a^2} &= \frac{\lambda}{a^2}\ (3p_{,r} - \rho_{,r}) \\
\mathcal{P}\ \mathcal{U}^t\ (\cancel{\mathcal{U}^r_{,t}} + \Gamma^r_{tt}\ \mathcal{U}^t + \Gamma^r_{tr}\ \cancel{\mathcal{U}^r}) + \frac{\mathcal{P}_{,r}}{a^2} &= \frac{\lambda}{a^2}\ (3p_{,r} - \rho_{,r}) \\
\mathcal{P}\ \frac{1}{\alpha}\ (\frac{\alpha\alpha_{,r}}{a^2}\ \frac{1}{\alpha}) + \frac{\mathcal{P}_{,r}}{a^2} &= \frac{\lambda}{a^2}\ (3p_{,r} - \rho_{,r}) \\
\mathcal{P}\ \frac{\alpha_{,r}}{\alpha} + \mathcal{P}_{,r} &= \lambda(3p_{,r} - \rho_{,r}).
\end{aligned} \tag{3.69}$$

Eq. (3.69) simplifies to

$$\boxed{\Big[\ln(\alpha\mathcal{P})\Big]_{,r} = \lambda\frac{3p_{,r} - \rho_{,r}}{\mathcal{P}}} \tag{3.70}$$

Eq. (3.70) will give us α on each hypersurface given the pressure of aether and other spatial parameters.

3.1.2 1+1 ADM Equations

Constraint Equations

As we saw in Eq. (3.5)

$$G_{\mu\nu} = 8\pi\mathcal{G}\ \tilde{T}_{\mu\nu}, \tag{3.71}$$

where $\mathcal{G} = G_N/(1-\lambda)$ and

$$\tilde{T}_{\mu\nu} \equiv T_{\mu\nu} - \lambda T g_{\mu\nu} + \mathcal{T}_{\mu\nu}. \tag{3.72}$$

The three-density is

$${}^{(3)}\rho \equiv n_\alpha n_\beta \tilde{T}^{\alpha\beta} = \alpha^2 \tilde{T}^{tt} = \rho(W^2-\lambda) + p(W^2+3\lambda-1). \tag{3.73}$$

The three-current is

$$\begin{aligned} S_r &\equiv -(g_{r\alpha} + n_r n_\alpha) n_\beta \tilde{T}^{\alpha\beta} \\ &= (\rho + p)\ u_r\ W, \end{aligned} \tag{3.74}$$

$$\tag{3.75}$$

We also have

$$S^i_j \equiv (\delta^i_\alpha + n^i n_\alpha)(\delta^\beta_j + n^\beta n_j)\tilde{T}^\alpha_\beta = \tilde{T}^i_j \tag{3.76}$$

And the trace $S = S^i_i$ will be

$$S = (\rho+p)\frac{u_r^2}{a^2} + 3p - 3\lambda(3p-\rho) + 3\mathcal{P}. \tag{3.77}$$

We can write the Hamiltonian constraint as

$$\boxed{16\pi\mathcal{G}\ {}^{(3)}\rho = R + 4K^r_r K^\theta_\theta + 2{K^\theta_\theta}^2} \tag{3.78}$$

where the three dimensional Ricci scalar in spherical symmetry is

$$R = \frac{-2}{r^2 a^3 b^2}\Big[-2r a_{,r} b(r b_{,r} + b) + a\big[r^2 {b_{,r}}^2 + 2rb(3b_{,r} + r b_{,r,r}) + b^2\big] - a^3\Big]. \tag{3.79}$$

The momentum constraint in spherical symmetry is

$$\boxed{-4\pi\mathcal{G}\ S_r = K^\theta_{\theta\,,r} + \frac{(r^2b^2)_{,r}}{2r^2b^2}(K^\theta_\theta - K^r_r)} \tag{3.80}$$

Evolution equations

The evolution equations for the metric components a and b and K^r_r and K^θ_θ in spherical symmetry are as follows

$$
\begin{aligned}
a_{,t} &= -\alpha a K^r_r && (3.81)\\
b_{,t} &= -\alpha b K^\theta_\theta && (3.82)\\
K^r_{r\,,t} &= -\frac{1}{a}(\frac{\alpha_{,r}}{a})_{,r} + \alpha\Big[-\frac{2}{arb}\big[\frac{(rb)_{,r}}{a}\big]_{,r} + KK^r_r + 4\pi\mathcal{G}(S - {}^{(3)}\rho) - 8\pi\mathcal{G}S^r_r\Big] && (3.83)\\
K^\theta_{\theta\,,t} &= \frac{\alpha}{(rb)^2} - \frac{1}{a(rb)^2}\big[\frac{\alpha rb}{a}(rb)_{,r}\big]_{,r} + \alpha\Big[KK^\theta_\theta + 4\pi\mathcal{G}(S - {}^{(3)}\rho) - 8\pi\mathcal{G}S^\theta_\theta\Big]. && (3.84)
\end{aligned}
$$

Finally we derive an equation for the evolution of K (the trace of the extrinsic curvature) as follows:

$$
\begin{aligned}
K_{,t} &= K^r_{r\,,t} + 2K^\theta_{\theta\,,t} && (3.85)\\
&= -\frac{1}{a^2}\Big[\alpha_{,r\,,r} + \frac{2\alpha_{,r}}{r} + \alpha_{,r}[\frac{2b_{,r}}{b} - \frac{a_{,r}}{a}]\Big] + \alpha\mathcal{X} && (3.86)\\
&= -\frac{1}{a^2}\Big[\nabla^2\alpha + \alpha_{,r}[\frac{2b_{,r}}{b} - \frac{a_{,r}}{a}]\Big] + \alpha\mathcal{X}, && (3.87)
\end{aligned}
$$

where $\nabla^2\alpha = \alpha_{,r\,,r} + 2\alpha_{,r}/r$ in spherical symmetry and using the Hamiltonian constraint (3.78), $\mathcal{X}$ simplifies to

$$\mathcal{X} = K^{r2}_r + 2K^{\theta 2}_\theta + 4\pi\mathcal{G}(S + {}^{(3)}\rho). \tag{3.88}$$

Therefore the time evolution of K is given by

$$\boxed{K_{,t} = -\frac{1}{a^2}\Big[\nabla^2\alpha + \alpha_{,r}[\frac{2b_{,r}}{b} - \frac{a_{,r}}{a}]\Big] + \alpha\Big[K^{r2}_r + 2K^{\theta 2}_\theta + 4\pi\mathcal{G}(S + {}^{(3)}\rho)\Big]} \tag{3.89}$$

3.1.3 Formulation in Standard Form

After having mapped our quantities on hypersurfaces in the 1+1 ADM formalism described in the previous section, we need to decide which quantities we are evolving in time and which quantities we are obtaining by solving spatial differential equations on the hypersurfaces in each time step. In other words we should build a state vector that will be evolved in time with a set of auxiliary parameters determined at each time step.

The degrees of freedom of the matter fluid are the pressure p and the radial component of the velocity u_r. The matter and energy densities (ρ and ρ_0) are obtained as functions of the

pressure p for a polytropic EOS via Equations (3.15) and (3.19). The pressure and velocity can be used to construct two flux conservative variables that can be evolved numerically in time as we will see in Section 3.1.3.

The geometric degrees of freedom are the three metric components α, a and b and the two extrinsic curvature components K^r_r and K^θ_θ. The spatial metric components a and b as well as the trace of the extrinsic curvature K can be evolved in time using equations in Section 3.1.2. Having K, we can find its components (K^r_r and K^θ_θ) via solving the momentum constraint (3.80). The degree of freedom of the aether is the value of its pressure $\mathcal{P}$ which can be algebraically calculated through Eq. (3.67). Finally, the lapse function will be given by solving Eq. (3.70) on each hypersurface.

The reason we choose to evolve the trace of the extrinsic curvature K alongside solving the momentum constraint, instead of solving for the Hamiltonian and momentum constraints to find the extrinsic curvature, is the fact that near hydrostatic equilibrium (the initial condition of our problem which will be discussed in Section 3.2), the extrinsic curvature and velocity are small. Therefore, while the momentum constraint is of first order in u_r and K, the Hamiltonian constraint (3.78) is of second order in K and therefore devoid of information about the extrinsic curvature near hydrostatic equilibrium.

In Section 3.1.3, we will construct our state vector to be integrated in time, and in Section 3.1.3, we will collect the equations that constrain our auxiliary parameters on each hypersurface.

The State Vector and Time Integrals

The time evolution is given by the following flux-conservative equation where the fluid sector is given by the Valencia formulation (Martí et al., 1991) which can be found in "Numerical Relativity, Solving Einstein's Equations on the Computer" by Baumgarte & Shapiro (2010):

$$\boxed{\partial_t \mathcal{V} + \partial_r \mathcal{F}^r = \mathcal{M}} \tag{3.90}$$

where the *State Vector* $\mathcal{V}$ is defined as

$$\mathcal{V} = \begin{pmatrix} \tilde{S}_r \\ \tilde{\tau} \\ K \\ a \\ b \end{pmatrix} = \begin{pmatrix} \gamma^{1/2}\ \alpha T^t_r \\ \alpha^2\ \gamma^{1/2}\ T^{tt} - \gamma^{1/2}\ W\rho_0 \\ K \\ a \\ b \end{pmatrix}, \tag{3.91}$$

the *Flux Vector* $\mathcal{F}^r$ is given by

$$\mathcal{F}^r = \begin{pmatrix} \alpha\ \gamma^{1/2}\ T^r_r \\ \alpha^2\ \gamma^{1/2}\ T^{tr} - \gamma^{1/2}\ W\rho_0 v^r \\ 0 \\ 0 \\ 0 \end{pmatrix}, \tag{3.92}$$

and the *Source Vector* $\mathcal{M}$ is

$$\mathcal{M} = \begin{pmatrix} \frac{1}{2}\alpha\ \gamma^{1/2}\ T^{\alpha\beta} g_{\alpha\beta,r} \\ \alpha\ \gamma^{1/2}\ (T^{\mu t}\partial_\mu \alpha - {}^{(4)}\Gamma^t_{\alpha\beta} T^{\alpha\beta}\alpha) \\ -\frac{1}{a^2}\Big[\nabla^2\alpha + \alpha_{,r}[\frac{2b_{,r}}{b} - \frac{a_{,r}}{a}]\Big] + \alpha\Big[K_r^{r\,2} + 2K_\theta^{\theta 2} + 4\pi\mathcal{G}(S + {}^{(3)}\rho)\Big] \\ -\alpha a K^r_r \\ -\alpha b K^\theta_\theta \end{pmatrix}, \tag{3.93}$$

where $\gamma = a^2 b^4 r^4 \sin^2(\theta)$ is the determinant of the three-dimensional metric. We also have the following equalities

$$\begin{aligned}
T^t_r &= (\rho + p)\frac{W}{\alpha} u_r, && (3.94)\\
T^{tt} &= (\rho + p)\frac{W^2}{\alpha^2} - \frac{p}{\alpha^2}, && (3.95)\\
T^r_r &= (\rho + p)\frac{(v^r)^2 W^2 a^2}{\alpha^2} + p, && (3.96)\\
T^{tr} &= (\rho + p)\frac{W^2}{\alpha^2} v^r, && (3.97)\\
T^{rr} &= (\rho + p)\frac{W^2}{\alpha^2}(v^r)^2 + \frac{p}{a^2}, && (3.98)\\
T^{\theta\theta} &= T^{\phi\phi}\sin^2(\theta) = \frac{p}{b^2 r^2}, && (3.99)\\
\tilde{S}_r &= \gamma^{1/2}(\rho + p) W u_r, && (3.100)\\
\tilde{\tau} &= \gamma^{1/2}\big[(\rho + p)W^2 - p\big] - \gamma^{1/2}\ W\rho_0, && (3.101)\\
\alpha\ \gamma^{1/2}\ (T^{\mu t}\partial_\mu \alpha - {}^{(4)}\Gamma^t_{\alpha\beta} T^{\alpha\beta}\alpha) &= \gamma^{1/2}(-a a_{,t} T^{rr} - 2r^2 b b_{,t} T^{\theta\theta}) \\
&= \gamma^{1/2}\alpha\ (a^2 K^r_r T^{rr} + 2r^2 b^2 K^\theta_\theta T^{\theta\theta}), && (3.102)
\end{aligned}$$

where $W = \sqrt{1 + u_r^2/a^2}$ is the Lorentz factor and $v^r = u^r/u^t$ is the fluid 3-velocity with respect to a coordinate observer. It simplifies to

$$v^r = \frac{\alpha}{W a^2} u_r. \tag{3.103}$$

Constraints on Auxiliary Parameters

The constraints on our auxiliary parameters can be written as

$$\boxed{\partial_r(\mathcal{H}) = g(\mathcal{H}, \mathcal{N})} \tag{3.104}$$

where the *Auxiliary Parameter Vector* $\mathcal{H}$ is given by

$$\mathcal{H} = \begin{pmatrix} K_\theta^\theta \\ \\ \ln(\alpha) \end{pmatrix}, \tag{3.105}$$

and

$$g(\mathcal{H}, \mathcal{N}) = \begin{pmatrix} -4\pi\mathcal{G}S_r - \Big[(r^2b^2)_{,r}/(2r^2b^2)\Big](K_\theta^\theta - K_r^r) \\ \\ \Big[\lambda(3p_{,r} - \rho_{,r}) - \mathcal{P}_{,r}\Big]/\mathcal{P} \end{pmatrix}, \tag{3.106}$$

where $\mathcal{N} = (p, u_r)$ is the *Primitive State Vector* for the matter fluid and

$$\begin{aligned}
K_r^r &= \frac{16\pi\mathcal{G}\ {}^{(3)}\rho - R - 2K_\theta^{\theta 2}}{4K_\theta^\theta}, && (3.107)\\
K &= K_r^r + 2K_\theta^\theta, && (3.108)\\
R &= -\frac{2\Big[-2rba_{,r}\,(rb_{,r} + b) + a\Big[r^2b_{,r}^2 + 2rb(rb_{,r,r} + 3b_{,r}) + b^2\Big] - a^3\Big]}{r^2a^3b^2}, && (3.109)\\
{}^{(3)}\rho &\equiv n_\alpha n_\beta \tilde{T}^{\alpha\beta} = \alpha^2\tilde{T}^{tt} = \rho(W^2 - \lambda) + p(W^2 + 3\lambda - 1), && (3.110)\\
S_r &\equiv -(g_{r\alpha} + n_r n_\alpha) n_\beta \tilde{T}^{\alpha\beta} \\
&= (\rho + p)\ u_r\ W, && (3.111)\\
\mathcal{P} &= \lambda\ (3\frac{\partial p}{\partial \rho} - 1)\ \frac{\Omega_0}{K}, && (3.112)\\
\Omega_0 &\equiv \frac{\mathcal{B}_0\mathcal{S}_0 - \mathcal{Q}_0\mathcal{C}_0}{\mathcal{A}_0\mathcal{Q}_0 - \mathcal{L}_0\mathcal{B}_0}, && (3.113)\\
\mathcal{A}_0 &= W, && (3.114)\\
\mathcal{B}_0 &= \frac{(\rho + p)\ u_r}{Wa^2}, && (3.115)\\
\mathcal{Q}_0 &= \frac{(\rho + p)\ W}{a^2}, && (3.116)
\end{aligned}$$

$$\mathcal{L}_0 = W \frac{\partial p}{\partial \rho} \frac{u_r}{a^2}, \tag{3.117}$$

$$\mathcal{C}_0 = \frac{\rho + p}{\gamma^{1/2}} (\gamma^{1/2}\ u^r)_{,r} + \rho_{,r} u^r + (\rho + p)\big(- W K^r_r - 2W K^\theta_\theta + \frac{K^r_r {u_r}^2}{a^2 W}\big), \tag{3.118}$$

$$\mathcal{S}_0 = (\rho + p)\Big[\frac{2u_r W K^r_r}{a^2} - 2K^r_r W u^r + \frac{a_{,r}}{a}(u^r)^2 + {u^r}_{,r}\ u^r\Big] + p_{,r}(u^r)^2 + \frac{p_{,r}}{a^2}. \tag{3.119}$$

3.1.4 Boundary Conditions

In this section, we describe the boundary conditions we impose on our system. Our boundary conditions are of two types: the symmetry boundary at the origin $r = 0$ and the outer boundary at the maximum radius, $r = R_{max}$.

Spherical Symmetry

We first discuss symmetry boundary conditions. This is not a "physical" boundary, since it does not correspond to the edge of our physical domain. Indeed, it corresponds to the *centre* of our domain. However, mathematically, the radial coordinate $r \in [0, R_{max}]$ for some R_{max} and we must impose boundary conditions at $r = 0$.

To impose a symmetry boundary condition, we demand that we must be able to analytically continue every function $f(r)$ to $f(-r)$ for $r \geq 0$ in a way that corresponds to the physics we would like to capture.

How we should analytically continue a function depends on the physical quantity it represents. Scalar quantities (in the formal sense) must be the same for positive and negative r and thus they must be even about r. For consistency, *gradients* of scalar quantities, must therefore be odd in r.

Functions that represent fluxes of a conserved quantity must be odd with respect to r. We can understand this in two ways. First, a flow of particles in the $+x$ direction is traveling away from the origin at positive r but traveling towards the origin for negative r. Second, the origin defines a spherical shell of zero area and radius, so any flux through the origin (quantities that correspond to gradients) must vanish.

We can carry our intuition about scalars and fluxes to other quantities as well. The metric quantities a and b; the extrinsic curvature quantities K^r_r and K^θ_θ; the lapse α; the hydrodynamic density ρ, pressure p, and energy density $\tilde{\tau}$; and the pressure of the aether, $\mathcal{P}$, are all "scalar-like" and should be even in r. On the other hand, the radial velocity

of matter u_r and the conserved momentum $\tilde{S}_r$ are "gradient-like" and should be odd in r. Therefore, we demand the following conditions on our quantities, both evolved (3.90) and solved for elliptically (3.104):

$$a_{,r}\Big|_{r=0} = b_{,r}\Big|_{r=0} = (K^r_r)_{,r}\Big|_{r=0} = (K^\theta_\theta)_{,r}\Big|_{r=0} = \alpha_{r=0}\Big|_{r=0} = \mathcal{P}_{,r}\Big|_{r=0} = 0, \tag{3.120}$$

$$\rho_{,r}\Big|_{r=0} = p_{,r}\Big|_{r=0} = \tilde{\tau}_{,r}\Big|_{r=0} = 0, \tag{3.121}$$

$$\text{and } u_r\Big|_{r=0} = \tilde{S}_r\Big|_{r=0} = 0. \tag{3.122}$$

Asymptotic Boundary Conditions

In addition to the non-physical symmetry boundary at the origin, we have a boundary at a maximum radius $r = R_{max}$. This represents the edge of our domain of interest, but not the edge of the universe. Therefore, our outer boundary conditions should represent that the universe continues further away, but is uninteresting.

We encode this "boring" property several ways, depending on the physical quantity in question. For example, for metric quantities like lapse α and space-like terms a and b, we can impose *asymptotic flatness* (Alcubierre, 2008). The idea here is that, far from the origin, the metric should look roughly like the Schwarzschild metric

$$ds^2 = -\left(1 - \frac{C}{r}\right) dt^2 + \left(1 - \frac{C}{r}\right)^{-1} dr^2 + r^2 \left[d\theta^2 + \sin^2(\theta) d\phi^2\right], \tag{3.123}$$

where C is an unknown constant. In this case, we can read the lapse at the outer boundary $r = R_{max}$ off from the Schwarzschild line element (3.123):

$$\alpha\Big|_{r=R_{max}} = 1 - \frac{C}{R_{max}}. \tag{3.124}$$

To eliminate c, we differentiate Eq. (3.124) and relate $\alpha_{,r}$ to α, which gives (Alcubierre, 2008):

$$\alpha_{,r} = \frac{1 - \alpha}{r}. \tag{3.125}$$

If need be, one can proceed similarly for other metric quantities.

Another type of boundary condition is the so-called "radiative" boundary condition (Alcubierre, 2008). Here the idea is that, far from the origin, all propagating degrees of freedom should behave as outgoing spherical waves. In spherical symmetry, this is

$$(ru)_{,t}\Big|_{r=R_{max}} + (ru)_{,r}\Big|_{r=R_{max}} = 0, \tag{3.126}$$

for an arbitrary wave-like variable u (Israeli & Orszag, 1981). This boundary condition is extremely good in spherical symmetry. However, with less symmetry, outgoing modes are only approximately spherical waves. And in this case, energy can be reflected back into the domain from the outer boundary.

A Final Note On Boundary Conditions

We conclude this section by noting that, if the outer boundary is sufficiently far from the domain of interest, it doesn't much matter what boundary condition we choose. Even a simple Dirichlet boundary condition (zero time derivatives of our variables), if well chosen, will suffice. The reason for this is, of course, because any pathologies at the outer boundary will take a long time to propagate to the domain of interest, hopefully longer than the relevant dynamical time scale.

Therefore, we will first report on results without outer boundary conditions and then implement the simplest one that works for our purposes.

3.2 Initial Data

Setting our initial data starts with asking what our hydrodynamical degrees of freedom are. As mentioned previously, the matter fluid has two degrees of freedom, the pressure p and the radial velocity u_r. The aether pressure $\mathcal{P}$ is then dynamically fixed as a function of these matter variables (with a proper choice of the initial condition for the trace of the extrinsic curvature K, which as we will see will determine the initial velcity u_r). We choose the initial pressure profile of the star to correspond to one of a neutron star in hydrostatic equilibrium which mass resides near the maximum mass in the mass-radius relationship of neutron stars[1]. This is done because a neutron star which mass is close to the maximum

[1]Every point on such a mass-radius relationship corresponds to a neutron star with a specific value of central pressure $p_{(r=0)}$ and in our current units, setting $p_{(r=0)} = 0.012$ will give us a neutron star which mass is slightly lower than the maximum mass allowed and which radius is slightly higher than the radius of the neutron star with the maximum mass.

mass in the mass-radius relationship is more prone to instabilities, and therefore, a small perturbation will cause its dynamical evolution away from hydrostatic equilibrium. Such a hydrostatic profile was calculated by Kamiab & Afshordi (2011) for the aether theory. There, a shooting method was employed, and the profile was calculated by numerically integrating the Einstein equations from the outside-in. For the purposes of this work, the radial derivatives need to be of very high accuracy at the center of the star, and as a shooting method from the outside-in, results in errors at the center of the star, we find a new way of calculating hydrostatic profiles by integrating from the inside-out. This scheme which comprises a derivation of the "Tolman-Oppenheimer-Volkoff (TOV) equation(s)" for the aether theory will be explained in Section 3.2.1.

In order to give the star an initial velocity u_r and have it evolve in time, we choose an initial radially constant trace of the extrinsic curvature K and based on that calculate the corresponding velocity profile of the star to linear order. This calculation will be presented in Section 3.2.3.

3.2.1 TOV Equations for the Aether Theory

We start by defining two parameters based on the metric components

$$A = g_{rr} = a^2, \tag{3.127}$$

$$B = -g_{tt} = \alpha^2. \tag{3.128}$$

We set the metric variable $b = 1$ on the initial hypersurface as it can be absorbed into the definition of the radius r. Therefore the metric can be written as

$$g_{\mu\nu} = \begin{pmatrix} -B(r) & 0 & 0 & 0 \\ 0 & A(r) & 0 & 0 \\ 0 & 0 & r^2 & 0 \\ 0 & 0 & 0 & r^2 \sin^2(\theta) \end{pmatrix}. \tag{3.129}$$

The generalized Einstein equation for the aether can be written as

$$G_{\mu\nu} = 8\pi \tilde{T}_{\mu\nu}, \tag{3.130}$$

where $G_N = 1$ in our units. The gravitational constant of the theory $\mathcal{G} = 1/(1-\lambda)$ is absorbed into the the effective energy-momentum tensor $\tilde{T}_{\mu\nu}$ which is given by

$$\tilde{T}_{\mu\nu} = \frac{1}{1-\lambda}\Big[T_{\mu\nu} - \lambda T g_{\mu\nu} + \mathcal{P}(\mathcal{U}_\mu \mathcal{U}_\nu + g_{\mu\nu})\Big]. \tag{3.131}$$

Based on this effective energy momentum tensor, we can define an effective energy density and pressure for the aether theory as

$$\tilde{T}^{\mu}_{\nu} = \begin{pmatrix} -\tilde{\rho} & 0 & 0 & 0 \\ 0 & \tilde{p} & 0 & 0 \\ 0 & 0 & \tilde{p} & 0 \\ 0 & 0 & 0 & \tilde{p} \end{pmatrix}, \tag{3.132}$$

where

$$\tilde{\rho} = \rho + \frac{3\lambda}{1-\lambda}\, p, \tag{3.133}$$

$$\tilde{p} = \frac{1-3\lambda}{1-\lambda}\, p + \frac{\lambda}{1-\lambda}\, \rho + \frac{1}{1-\lambda}\, \mathcal{P}. \tag{3.134}$$

As the static aether theory is equivalent to general relativity with an effective energy density and pressure given by Eqs. (3.133) and (3.134), the angular component of the Riemann tensor $R_{\theta\theta}$ in the static Einstein equation, like general relativity, is given by (Weinberg, 1972):

$$R_{\theta\theta} = -1 + \frac{r}{2A}(-\frac{A_{,r}}{A} + \frac{B_{,r}}{B}) + \frac{1}{A} = -4\pi(\tilde{\rho} - \tilde{p})r^2, \tag{3.135}$$

and the conditions of energy momentum conservation for matter and for the effective energy momentum tensor (required by Bianchi identity) give (Weinberg, 1972):

$$T^{\mu\nu}{}_{;\mu} = 0 \;\rightarrow\; \frac{B_{,r}}{B} = -\frac{2\; p_{,r}}{\rho + p}, \tag{3.136}$$

$$\tilde{T}^{\mu\nu}{}_{;\mu} = 0 \;\rightarrow\; \frac{B_{,r}}{B} = -\frac{2\; \tilde{p}_{,r}}{\tilde{\rho} + \tilde{p}}. \tag{3.137}$$

In spherical symmetry, A is given in terms of the mass m enclosed inside radius r as

$$A = (1 - \frac{2m}{r})^{-1}, \tag{3.138}$$

and m is related to the effective energy density as

$$m(r) = \int_0^r \tilde{\rho}(r')\; 4\pi r'^2 dr'. \tag{3.139}$$

Therefore we have

$$A_{,r} = -(1 - \frac{2m}{r})^{-2}\; (\frac{-2m_{,r}r + 2m}{r^2}). \tag{3.140}$$

Using the fact that $m_{,r} = 4\pi\tilde{\rho}\, r^2$ we have

$$A_{,r} = -(1 - \frac{2m}{r})^{-2}\ (-8\pi\tilde{\rho}\, r + \frac{2m}{r^2}). \tag{3.141}$$

Using the above equality in Eq. (3.135) we get

$$\begin{aligned}
\frac{B_{,r}}{B} &= (R_{\theta\theta} - \frac{1}{A} + 1)\ \frac{2A}{r} + \frac{A_{,r}}{A} \\
&= \Big[-4\pi(\tilde{\rho} - \tilde{p})\ r^2 \cancel{-1} + \frac{2m}{r} \cancel{+1} \Big] \frac{2(1 - 2m/r)^{-1}}{r} + \\
&\quad -(1 - \frac{2m}{r})^{-1}\ (-8\pi\tilde{\rho}\, r + \frac{2m}{r^2}) \\
&= (1 - \frac{2m}{r})^{-1} (\cancel{-8\pi\tilde{\rho}\, r} + 8\pi\tilde{p}\, r + \frac{4m}{r^2} - \frac{2m}{r^2} \cancel{+8\pi\tilde{\rho}\, r}) \\
&= 2\ (1 - \frac{2m}{r})^{-1}\ (4\pi\tilde{p}\, r + \frac{m}{r^2})
\end{aligned} \tag{3.142}$$

Equations (3.136), (3.137) and (3.142) combined will give the two TOV equations for the aether theory:

$$\boxed{
\begin{aligned}
-\frac{p_{,r}}{\rho + p} &= (1 - \frac{2m}{r})^{-1}\ (4\pi\tilde{p}\, r + \frac{m}{r^2}) && (3.143) \\
-\frac{\tilde{p}_{,r}}{\tilde{\rho} + \tilde{p}} &= (1 - \frac{2m}{r})^{-1}\ (4\pi\tilde{p}\, r + \frac{m}{r^2}) && (3.144) \\
m(r) &= \int_0^r \tilde{\rho}(r')\ 4\pi r'^2 dr' && (3.145)
\end{aligned}
}$$

Equations (3.143), (3.144) and (3.145) can be integrated numerically from the inside-out, starting at the center of the star ($r = 0$), given proper boundary conditions and assuming an EOS that would relate the energy density of matter to its pressure, in other words the function $\rho(p)$ given by Eq. (3.19). About boundary conditions, we assume a value for the central pressure, for example $p_{(r=0)} = 0.012$ (which in our units, corresponds to a neutron star which mass lies near the maximum mass allowed) and we also know that

$$m\Big|_{r=0} = 0, \tag{3.146}$$

$$p_{,r}\Big|_{r=0} = 0, \tag{3.147}$$

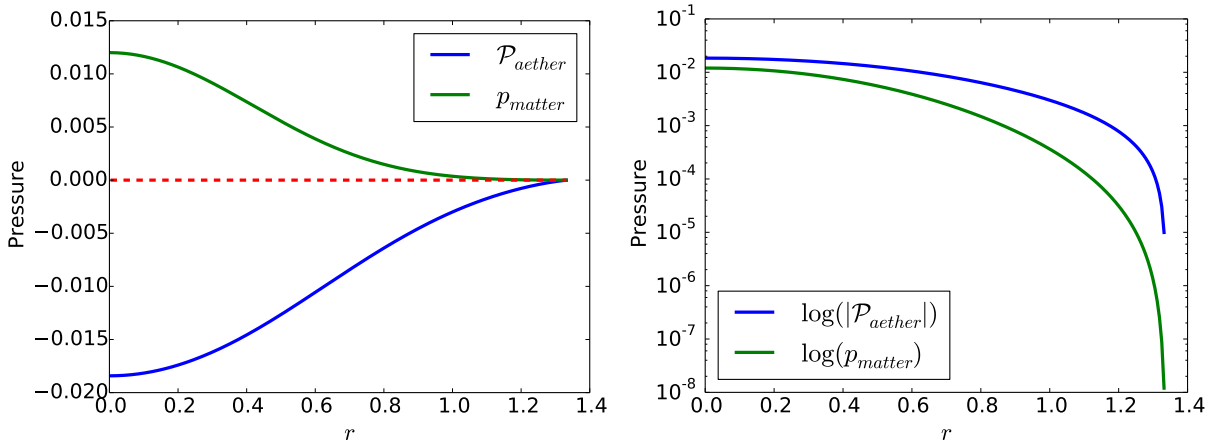

Figure 3.1: Pressure profiles of matter and aether for a neutron star in hydrostatic equilibrium with $p_{(r=0)} = 0.012$.

$$\tilde{p}_{,r}\Big|_{r=0} = 0. \tag{3.148}$$

The one remaining unknown boundary condition is the value of $\tilde{p}_{(r=0)}$ (in other words the central value of the aether pressure $\mathcal{P}_{(r=0)}$) corresponding to the value of $p_{(r=0)}$. In order to find this, we first attempted using a shooting method, trying different values of $\tilde{p}_{(r=0)}$; for each value integrating the equations numerically and choosing the value for which the radii where p and $\tilde{p}$ tend to zero coincide. In other words the value of $\tilde{p}_{(r=0)}$ for which

$$r\Big|_{p\to 0} = r\Big|_{\tilde{p}\to 0} = R_{NS}, \tag{3.149}$$

where R_{NS} is the radius of the neutron star. We find that the density profile calculated using this value of $\tilde{p}_{(r=0)}$ is not accurate and satisfies the Hamiltonian constraint (Eq. 3.78 with zero extrinsic curvature terms) only up to a few percent. The reason for this can be seen in Figure 3.1. As seen in the logarithmic figure, changing the central value of the aether pressure slightly does not affect the value of the radius at which that pressure tends to zero to a great extent, as it falls very sharply around that radius. Therefore, the shooting method's condition (3.149) does not do a good job at determining the precise value of $\tilde{p}_{(r=0)}$.

This incited us to use a different method for calculating the value of $\tilde{p}_{(r=0)}$. This method is based on a result found originally in a previous work (Kamiab & Afshordi,

2011), which established that the structure of a neutron star in aether theory, is equivalent to the structure found in general relativity with an effective equation of state, which can give us $\tilde{p}(p)$ and thus determine $\tilde{p}_{(r=0)}$, based on the value of the central pressure of matter $p_{(r=0)}$. Combining equations (3.136) and (3.137) we get

$$-\frac{p_{,r}}{\rho+p} = -\frac{\tilde{p}_{,r}}{\tilde{\rho}+\tilde{p}}, \tag{3.150}$$

$$\frac{dp}{\rho+p} = \frac{d\tilde{p}}{\tilde{\rho}+\tilde{p}}, \tag{3.151}$$

$$\rightarrow \frac{d\tilde{p}}{dp} = \frac{\tilde{\rho}(p)+\tilde{p}}{\rho(p)+p} = \frac{\rho(p)+\frac{3\lambda}{1-\lambda}\,p+\tilde{p}}{\rho(p)+p} = \frac{p^{\frac{1}{\Gamma}}+\frac{p}{\Gamma-1}+\frac{3\lambda}{1-\lambda}\,p+\tilde{p}}{p^{\frac{1}{\Gamma}}+\frac{p}{\Gamma-1}+p}, \tag{3.152}$$

where the last line uses Eqs. (3.133) (the effective energy density of aether) and (3.19) (the EOS of matter). Eq. (3.152) can be integrated numerically to find $\tilde{p}(p)$ using the boundary condition

$$\tilde{p}\Big|_{p=0} = 0. \tag{3.153}$$

The numerical methods used for dealing with differential equations like Eq. (3.152) where

$$\frac{d\tilde{p}}{dp}\Big|_{p\rightarrow 0} \rightarrow \frac{0}{0} \rightarrow C \tag{3.154}$$

will be described in Section 3.4. Having the function $\tilde{p}(p)$ will allow us to find the correct $\tilde{p}_{(r=0)}$ and integrating the TOV Eqs. (3.143) and (3.144) along with (3.145) will give us pressure profiles $p(r)$ and $\tilde{p}(r)$ for the neutron star that satisfy the Hamiltonian constraint with a much higher accuracy[2]. The numerical method used for integrating the TOV equations will also be explained in Section 3.4.

3.2.2 Adding an Atmosphere to the Star

The equations described in Section 3.1.3 break down in vacuum. In particular, if ρ and p vanish, we can not evolve the conserved variables $\tilde{S}_r$ and $\tilde{\tau}$. Worse, in vacuum $\mathcal{P}$ vanishes, making the lapse α undefined. To handle this, we add an artificial atmosphere of small density to the exterior of the star (Toro, 2009). Ideally the atmosphere is small enough that it induces a negligible error in the physical result but it still allows us to evolve our system outside the star.

[2]Close to numerical precision values for resolution of 1000 radial grid points.

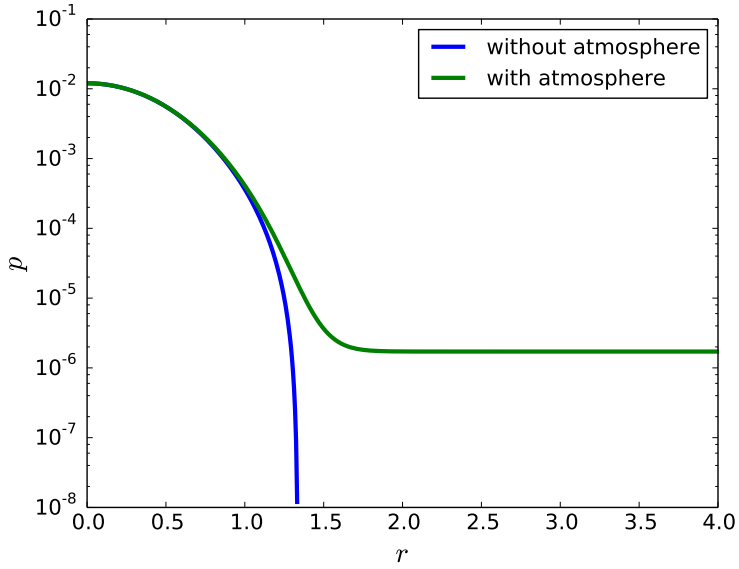

Figure 3.2: Pressure profile of matter on initial hypersurface obtained integrating the TOV Eqs. (3.143) and (3.144) (blue curve) and the TOV Eqs. (3.155) and (3.156) with atmosphere (green curve).

The way we add the atmosphere is by exponentially truncating our radial pressure derivatives in the TOV Eqs. (3.143) and (3.144) in the following way:

$$p_{,r} = -(\rho + p)(1 - \tfrac{2m}{r})^{-1} \left(4\pi\tilde{p}\, r + \tfrac{m}{r^2}\right) \times F_{trunc}(r), \tag{3.155}$$

$$\tilde{p}_{,r} = -(\tilde{\rho} + \tilde{p})(1 - \tfrac{2m}{r})^{-1} \left(4\pi\tilde{p}\, r + \tfrac{m}{r^2}\right) \times F_{trunc}(r), \tag{3.156}$$

where F_{trunc} is given by

$$F_{trunc}(r) = \frac{1}{2} + \frac{1}{2} \tanh\left[S_{trunc}[(R_{NS})^2 - r^2]\right], \tag{3.157}$$

where S_{trunc} controls the slope of the exponential truncation and R_{NS} is the radius of the neutron star (found through solving the original TOV equations without atmosphere). The reason we have the squares of radius in the above expression is the fact we need our pressure profiles to remain *even* with a zero radial derivative at the center of the star. The results of integrating Eqs. (3.155) and (3.156) assuming $S_{trunc} = 1.5$ are shown in Figures 3.2 and 3.3.

It is expected that such an exponential truncation will cause a violation of the Hamiltonian constraint as the Einstein equations are no longer satisfied. However if this truncation

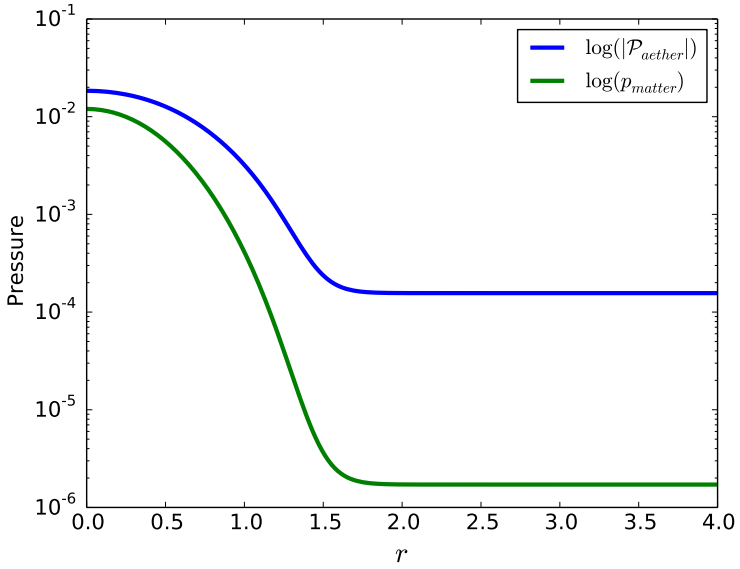

Figure 3.3: Pressure profiles of matter and aether on initial hypersurface obtained integrating the TOV Eqs. (3.155) and (3.156) with atmosphere.

takes effect near the radius of the star (in other words at very low values of energy density and pressure), the resulting violation of the Hamiltonian constraint will be small[3].

As the system evolves, special care must be taken to ensure that the atmosphere remains well-behaved. The density and pressure of the system must remain positive and the velocity of the atmosphere must remain small.

3.2.3 Initial Extrinsic Curvature and Velocity

As mentioned in Section 3.1.1, the aether pressure is given by

$$\mathcal{P} = \lambda \left(3\frac{\partial p}{\partial \rho} - 1\right) \frac{\Omega_0}{K}, \tag{3.158}$$

where $\Omega_0 = \rho_{,t}/\alpha$. One immediate consequence of this equation is that in the limit of hydrostatic equilibrium (our initial condition)

$$\left.\frac{\Omega_0}{K}\right|_{t\to 0} \to \frac{0}{0} \to \mathcal{P}_{hydrostatic}, \tag{3.159}$$

[3]The Hamiltonian constraint is satisfied up to 10^{-6} with a resolution of 200 radial grid points and up to 10^{-9} for 1000 grid points.

where $\mathcal{P}_{hydrostatic}$ is the pressure of the aether found by solving the TOV Eqs. (3.143) and (3.144). We would like to start with a small radially constant trace of the extrinsic curvature K on the initial hypersurface so that the above limit is still satisfied. This will result in a correspondingly small value for Ω_0 which will in turn give the initial velocity profile for the star. The reason we start by assuming K and then find u_r is that we would like K not to cross zero in the star as that may cause complications in solving our equations. One problem arising from K crossing zero is the $\frac{0}{0}$ limit in calculating $\mathcal{P}$ which will make things complicated numerically. A more fundamental complication is related to the sign of K. As we will demonstrate in the next section, the sign of K is of fundamental importance in determining the nature of the differential equations at the center of the star, and only one sign is allowed for physical stability, therefore K crossing zero might have pathological consequences for our system of equations. Therefore starting with

$$K\Big|_{t=0} = K_0, \tag{3.160}$$

where $|K_0| = \text{constant} > 0$, Eq. (3.158) gives

$$\Omega_0 = \frac{K_0 \mathcal{P}}{\lambda(3\frac{\partial p}{\partial \rho} - 1)}, \tag{3.161}$$

where $\mathcal{P} = \mathcal{P}_{hydrostatic}$, $p = p_{hydrostatic}$ and ρ is related to p through the polytropic EOS. In order to find u_r from Ω_0, we linearize Ω_0 and only keep terms of first order in u_r and K. As mentioned previously, Ω_0 is given by

$$\Omega_0 = \frac{\mathcal{B}_0 \mathcal{S}_0 - \mathcal{Q}_0 \mathcal{C}_0}{\mathcal{A}_0 \mathcal{Q}_0 - \mathcal{L}_0 \mathcal{B}_0}. \tag{3.162}$$

To linear order in u_r and K we have

$$\mathcal{B}_0 = (\rho + p)\, \frac{u_r}{a^2}, \tag{3.163}$$

$$\mathcal{A}_0 = 1, \tag{3.164}$$

$$\mathcal{Q}_0 = \frac{\rho + p}{a^2,} \tag{3.165}$$

$$\mathcal{L}_0 = \frac{\partial p}{\partial \rho}\, \frac{u_r}{a^2}, \tag{3.166}$$

$$\mathcal{C}_0 = \frac{\rho + p}{\gamma^{1/2}} (\gamma^{1/2} u^r)_{,r} + \rho_{,r} u^r - (\rho + p) K_0, \tag{3.167}$$

$$\mathcal{S}_0 = \frac{p_{,r}}{a^2}. \tag{3.168}$$

Therefore Ω_0 simplifies to

$$\Omega_0 = (p_{,r} - \rho_{,r})\ u^r + (\rho + p)\Big[K_0 - \frac{1}{\gamma^{1/2}}(\gamma^{1/2}u^r)_{,r}\Big]. \tag{3.169}$$

If we define the variable $\mathcal{Z} = \gamma^{1/2}u^r$ and combine Eqs. (3.161) and (3.195), we get the following differential equation for $\mathcal{Z}$:

$$\mathcal{Z}_{,r} \ = \ \frac{p_{,r} - \rho_{,r}}{\rho + p}\ \mathcal{Z} \ + \ K_0\gamma^{1/2}\ \Big[1 - \frac{\mathcal{P}}{\lambda(3\frac{\partial p}{\partial \rho} - 1)(\rho + p)}\Big]. \tag{3.170}$$

Solving the above differential equation with the boundary condition[4]

$$\mathcal{Z}\Big|_{r=0} = 0, \tag{3.171}$$

will give us the initial velocity profile of the star u_r corresponding to the choice of K_0. The results of this calculation for different values of K_0 are shown in Figure 3.4. As can be seen in the Figure, $u_r \propto r$ near the center of the star. As expected, the atmosphere has a higher velocity compared to the inside of the star as it does not satisfy the static Einstein equations. In order to see which sign and order of magnitude of K_0 is suitable for our initial conditions, it is time to look at the nature of our dynamical equations at the center of the star.

3.2.4 The Nature of Equations at the Center

Before studying the evolution numerically, it is suitable to investigate analytically the nature of our equations at the center of the star. Near the center, at $r = \epsilon$, where ϵ is a small number, the order of magnitude of the radial derivatives of the fluid's pressure and energy are

$$\rho_{,r} \ = \ \mathcal{O}(\epsilon), \tag{3.172}$$
$$p_{,r} \ = \ \mathcal{O}(\epsilon). \tag{3.173}$$

Near hydrostatic equilibrium, if we choose a trace of the extrinsic curvature of order

$$K = \mathcal{O}(\epsilon'), \tag{3.174}$$

[4] As the radial velocity needs to be zero at the center of the star in spherical symmetry.

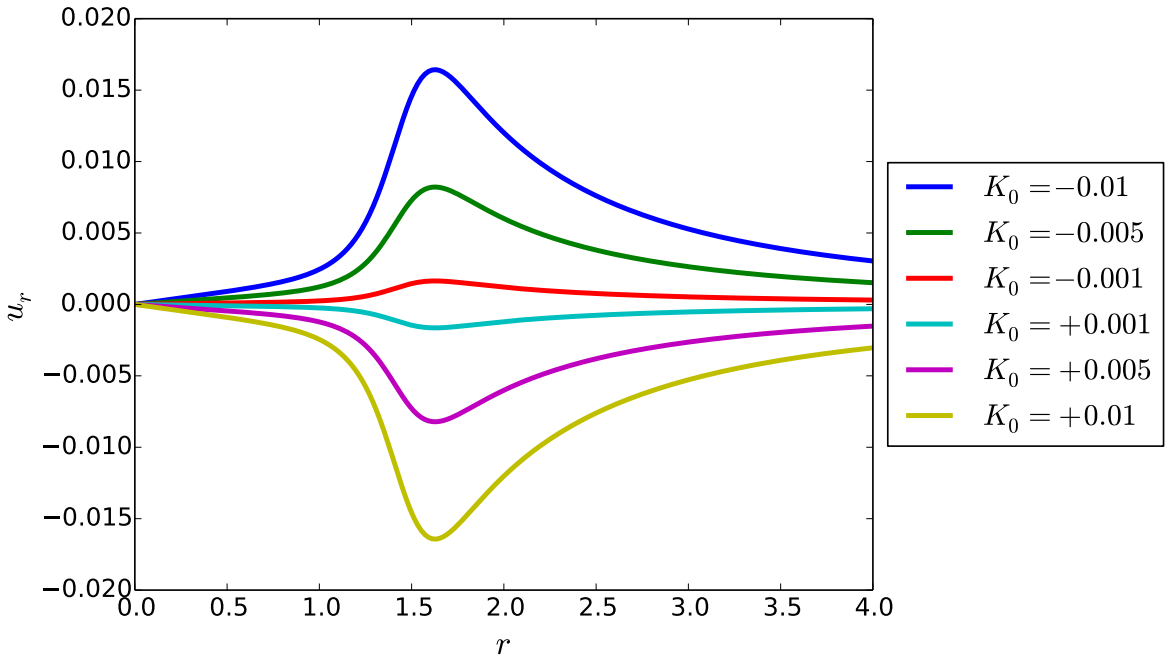

Figure 3.4: Velocity profiles u_r found by integrating Eq. (3.170) assuming different values of K_0.

and as near the center we have $u_r = rH$, where H is a constant, then Eq. (3.170) gives

$$3H \sim K\left[1 - \frac{\mathcal{P}}{\lambda(3\frac{\partial p}{\partial \rho} - 1)(\rho + p)}\right], \tag{3.175}$$

which demonstrates what we already saw in Figure (3.4) that

$$H = \mathcal{O}(K) = \mathcal{O}(\epsilon'). \tag{3.176}$$

In deriving Eq. (3.175) from (3.170), and also from now on in our calculation, we neglect terms like $\rho_{,r}u^r = \mathcal{O}(\epsilon \times \epsilon') \to 0$. We also assumed that near the center of the star and close to hydrostatic equilibrium $a \sim 1$.

Combining Eqs. (3.67) and (3.70) gives the following differential equation relating the lapse function and the extrinsic curvature:

$$\boxed{(\Omega\alpha)_{,r} = \Omega\alpha\frac{K_{,r}}{K} + (3p_{,r} - \rho_{,r})K\alpha} \tag{3.177}$$

where

$$\Omega \equiv (3\frac{\partial p}{\partial \rho} - 1)\ \Omega_0 \tag{3.178}$$

$$\Omega_0 = \frac{\mathcal{B}_0\mathcal{S}_0 - \mathcal{Q}_0\mathcal{C}_0}{\mathcal{A}_0\mathcal{Q}_0 - \mathcal{L}_0\mathcal{B}_0}, \tag{3.179}$$

$$\mathcal{A}_0 = W, \tag{3.180}$$

$$\mathcal{B}_0 = \frac{(\rho + p)\ u_r}{W a^2}, \tag{3.181}$$

$$\mathcal{Q}_0 = \frac{(\rho + p)\ W}{a^2}, \tag{3.182}$$

$$\mathcal{L}_0 = W\ \frac{\partial p}{\partial \rho}\ \frac{u_r}{a^2}, \tag{3.183}$$

$$\mathcal{C}_0 = \frac{\rho + p}{\gamma^{1/2}}(\gamma^{1/2}\ u^r)_{,r} + \rho_{,r}u^r + (\rho + p)\big(-WK^r_r - 2WK^\theta_\theta + \frac{K^r_r {u_r}^2}{a^2 W}\big), \tag{3.184}$$

$$\mathcal{S}_0 = (\rho + p)\Big[\frac{2u_r W K^r_r}{a^2} - 2K^r_r W u^r + \frac{a_{,r}}{a}(u^r)^2 + {u^r}_{,r}\ u^r\Big] + p_{,r}(u^r)^2 + \frac{p_{,r}}{a^2}. \tag{3.185}$$

In Eq. (3.177), we can neglect the second term as it is of order $\mathcal{O}(\epsilon \times \epsilon')$ and have

$$\frac{(\Omega\alpha)_{,r}}{\Omega\alpha} = \frac{K_{,r}}{K}, \tag{3.186}$$

$$\boxed{\Omega\alpha = CK}\ , \tag{3.187}$$

where C is an integration constant. In the limits where $\rho_{,r} \sim p_{,r} \sim \mathcal{O}(\epsilon)$ and $u_r/r = H \sim K \sim \mathcal{O}(\epsilon')$, and neglecting second order terms in ϵ and ϵ' and terms of order $\epsilon \times \epsilon'$, we get

$$\mathcal{A}_0 = 1, \tag{3.188}$$

$$\mathcal{B}_0 = (\rho + p)Hr, \tag{3.189}$$

$$\mathcal{Q}_0 = \rho + p, \tag{3.190}$$

$$\mathcal{L}_0 = \frac{\partial p}{\partial \rho}Hr, \tag{3.191}$$

$$\mathcal{C}_0 = (\rho + p)(3H - K), \tag{3.192}$$

$$\mathcal{S}_0 = p_{,r}. \tag{3.193}$$

Therefore Ω becomes

$$\Omega = (3\frac{\partial p}{\partial \rho} - 1)\ \Omega_0 = (3\frac{\partial p}{\partial \rho} - 1)\frac{\mathcal{B}_0\mathcal{S}_0 - \mathcal{Q}_0\mathcal{C}_0}{\mathcal{A}_0\mathcal{Q}_0 - \mathcal{L}_0\mathcal{B}_0} \tag{3.194}$$

$$= \quad (3\frac{\partial p}{\partial \rho} - 1)(\rho + p)(K - 3H). \tag{3.195}$$

Combining Eqs. (3.187) and (3.195), and evaluating K we get

$$K = \frac{3H(3\frac{\partial p}{\partial \rho} - 1)(\rho + p)\alpha}{(3\frac{\partial p}{\partial \rho} - 1)(\rho + p)\alpha - C}. \tag{3.196}$$

As we saw in Eq. (3.89), the time derivative of K is given as a function of the lapse function as

$$K_{,t} = -\nabla^2 \alpha + ... \tag{3.197}$$

Taking the time derivative of Eq. (3.196), and only keeping terms with time derivatives of the lapse function, and using Eq. (3.197), we get

$$\boxed{\frac{3\ CH\ (3\frac{\partial p}{\partial \rho} - 1)(\rho + p)}{\Big[(3\frac{\partial p}{\partial \rho} - 1)(\rho + p)\alpha - C\Big]^2}\ \alpha_{,t}\ + ...\ =\ \nabla^2 \alpha\ + ...} \tag{3.198}$$

Near the center of the star where the first radial derivatives of the lapse function are small, the above equation has the structure of a "*diffusion equation*" and is not a wave equation. This is a fundamental property of the aether equations near the center of the star and near hydrostatic equilibirum. Diffusion equations like $w\alpha_{,t} = \nabla^2 \alpha$ are well-posed when $w > 0$ and not well-posed when $w < 0$. Therefore, the sign of the coefficient of $\alpha_{,t}$ in Eq. (3.198) is of fundamental importance for the stability of the problem. The sign is determined by

$$CH(3\frac{\partial p}{\partial \rho} - 1) = \frac{\Omega \alpha}{K}\ H\ (3\frac{\partial p}{\partial \rho} - 1) = (3\frac{\partial p}{\partial \rho} - 1)^2(\rho + p)(K - 3H)\ \frac{H}{K}\ \alpha, \tag{3.199}$$

and as $H = u_r/r$ and K have opposite signs as seen in Figure 3.4, and as $\alpha > 0$, ultimately the above expression will be positive only when $K - 3H < 0$, which as K and H have opposite signs is equivalent to the conditions

$$\boxed{K < 0} \tag{3.200}$$

and

$$\boxed{H > 0} \tag{3.201}$$

To summarize, the lesson learned from this analytical approximation, is that the aether theory can be evolved in a well-posed way only when matter is "*expanding*" in the frame of aether and the problem of collapse of matter in the frame of aether is not be well-posed. This theoretical expectation was confirmed by our numerical evolution preliminary results as will be discussed in the following section.

3.3 Time Evolution

This section comprises work which is still in progress. In Section 3.3.1, the time evolution algorithm (the order in which we solve equations described in Section 3.1.3) will be described. We will briefly report on the preliminary results we found from the time evolution in Section 3.3.2. Much work has yet to be done in obtaining further results, testing and analyzing them.

3.3.1 Evolution Algorithm

The steps to take in order to evolve the system of equations formulated in standard form (described in Section 3.1.3) are as follows:

1. Obtain initial matter pressure $p_{(t=0)}$, aether pressure $\mathcal{P}_{(t=0)}$ and mass $m_{(t=0)}$ from integrating the TOV equations (3.143), (3.144) and (3.145).

2. Use the mass $m_{(t=0)}$ to obtain initial radial metric component $a_{(t=0)} = \sqrt{g_{rr}} = (1 - 2m_{(t=0)}/r)^{-1/2}$ and set $b_{(t=0)} = 1$.

3. Assume an initial value for the trace of the extrinsic curvature $K_{(t=0)} = K_0$, which will be radially constant on the initial hypersurface.

4. Use the values of $K_{(t=0)}$, $p_{(t=0)}$, $\mathcal{P}_{(t=0)}$, $a_{(t=0)}$ and $b_{(t=0)}$ to find the initial velocity profile $u_{r\,(t=0)}$ through integrating Eq. (3.170).

5. Having the initial *Primitive State Vector* $\mathcal{N}_{(t=0)} = [p_{(t=0)}, u_{r\,(t=0)}]$, $a_{(t=0)}$, $b_{(t=0)}$ and $K_{(t=0)}$, build the *State Vector* $\mathcal{V}_{(t=0)} = [\tilde{S}_{r\,(t=0)},\ \tilde{\tau}_{(t=0)},\ K_{(t=0)},\ a_{(t=0)},\ b_{(t=0)}]$ through the algebraic equations given in Section 3.1.3. The matter EOS equations given in Section 3.1.1 need to be used to relate the pressure, energy density and rest-mass density of matter.

6. Input the initial conditions into the *State Vector* $\mathcal{V}_{(t)} = \mathcal{V}_{(t=0)}$ to be evolved.

7. Define function $\mathcal{K}$ that takes the *State Vector* $\mathcal{V}_{(t)} = [\tilde{S}_{r\,(t)},\ \tilde{\tau}_{(t)},\ K_{(t)},\ a_{(t)},\ b_{(t)}]$ and gives

$$\mathcal{K}\Big[\mathcal{V}_{(t)}\Big] = \Big[p_{(t)},\ u_{r\,(t)},\ K^{r}_{r\,(t)},\ K^{\theta}_{\theta\,(t)},\ \mathcal{P}_{(t)},\ \alpha_{(t)}\Big], \tag{3.202}$$

where the matter pressure and velocity are found from $\tilde{S}_r$ and $\tilde{\tau}$ through the algebraic relations given in Section 3.1.3. The radial and angular extrinsic curvature components are found through solving the momentum constraint (3.80). The pressure of aether $\mathcal{P}$ is found through the algebraic Eq. (3.67). Finally, the lapse function α is found through integrating Eq. (3.70). Calculating the extrinsic curvature components and the lapse function forms our *Auxiliary Parameter Vector* $\mathcal{H}$ (3.105).

8. Having $\mathcal{V}_{(t)}$ and $\mathcal{K}\Big[\mathcal{V}_{(t)}\Big]$, calculate the *Flux and Source Vectors* (${\mathcal{F}^r}_{(t)}$ and $\mathcal{M}_{(t)}$) using equations given in Section 3.1.3.

9. Define a function f that numerically integrates the *State Vector* as

$$f\Big[\mathcal{V}_{(t)},\ {\mathcal{F}^r}_{(t)},\ \mathcal{M}_{(t)}\Big] = \mathcal{V}_{(t+\delta t)}, \tag{3.203}$$

   using $\partial_t \mathcal{V} + \partial_r \mathcal{F}^r = \mathcal{M}$ (3.90).

10. Input the evolved vector $\mathcal{V}_{(t+\delta t)}$ into the *State Vector* $\mathcal{V}_{(t)} = \mathcal{V}_{(t+\delta t)}$ to be evolved.

11. Repeat steps 7, 8, 9 and 10.

3.3.2 Preliminary Results

The dynamical time of our problem $1/\sqrt{G\bar{\rho}}$ (where $\bar{\rho}$ is the average mass density of the star) is of order unity. Our numerical results confirm our theoretical expectations about the role of initial conditions in the well-posedness of the equations (the analytic limit of our equations at the center of the star near hydrostatic equilibrium presented in Section 3.2.4). We do indeed find that for contracting matter initial conditions ($H < 0$ and $K_0 > 0$), the numerical results show an instability appearing at the center of the star in time scales $t > 10^{-5}$. For expanding matter initial conditions ($H > 0$ and $K_0 < 0$), the equations are hyperbolic at the center of the star. As can be seen in Figures 3.7 to 3.6, evolving the system to times $t \sim 10^{-3}$ exposes a problem with our outer boundary. The root of this problem is that we have not yet imposed an outer boundary condition on our system and have only fixed boundary conditions at the center of the star based on spherical symmetry as mentioned in Section 3.1.4. At the outer boundary, there will be in-going modes of propagation and out-going ones. The in-going modes will insert energy into the system and by violating energy conservation, tiny numerical errors will grow exponentially. We need to impose a boundary condition so that our problem is well-posed, thus damping the exponential growth of these modes. We choose the simplest outer boundary conditions,

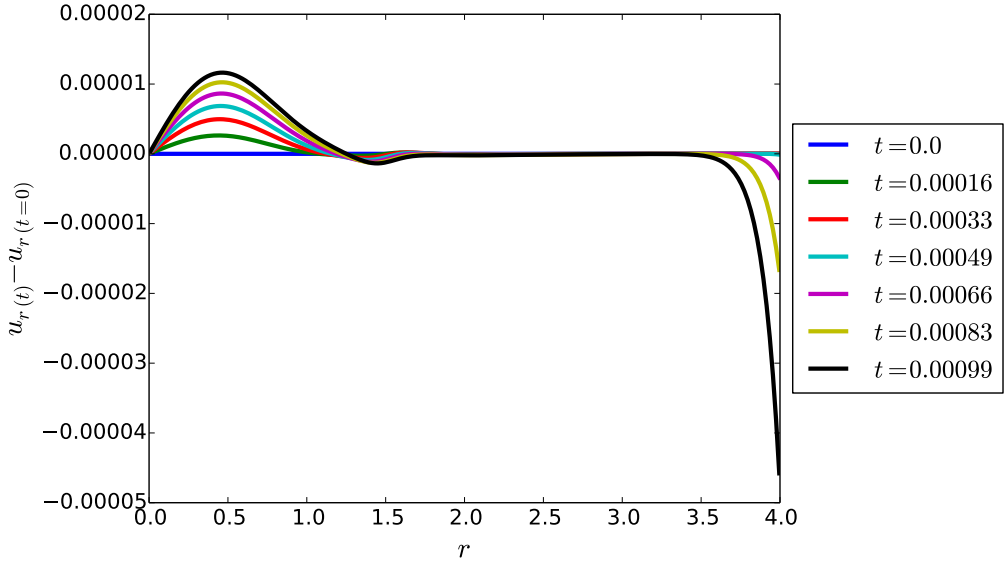

Figure 3.5: Effect of not fixing boundary conditions at the outer edge of the grid on the evolution of the radial velocity of matter u_r.

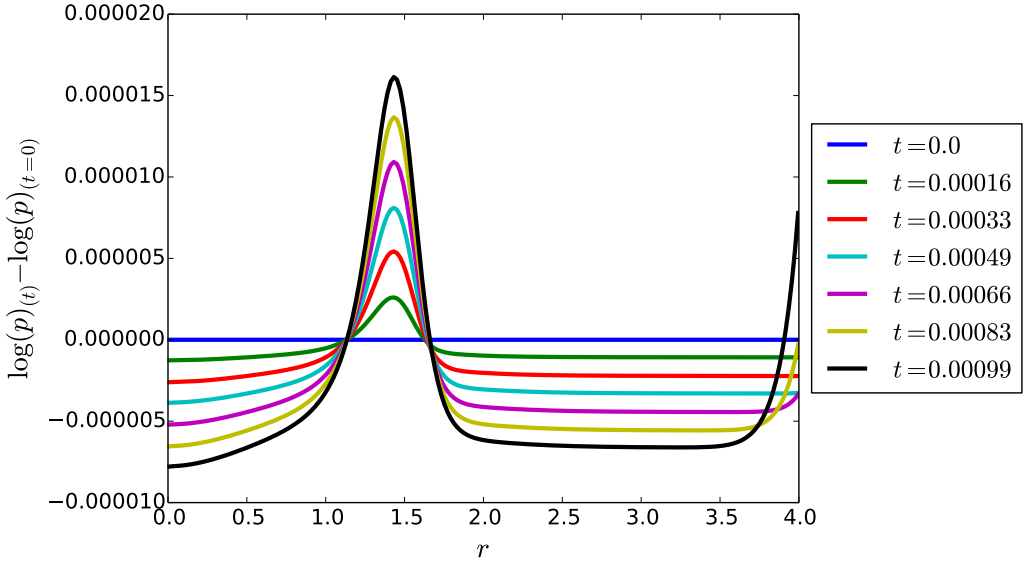

Figure 3.6: Effect of not fixing boundary conditions at the outer edge of the grid on the evolution of the pressure of matter p.

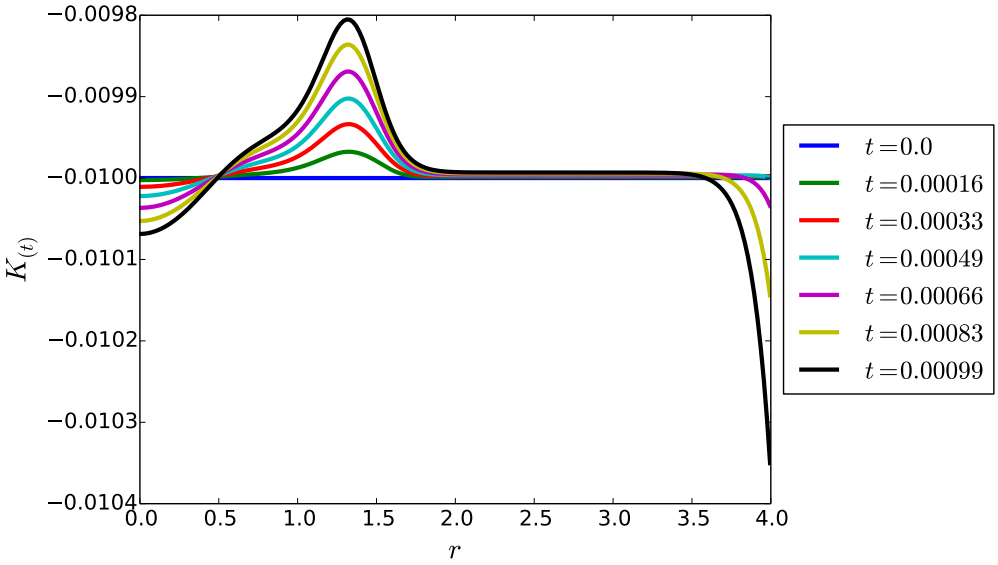

Figure 3.7: Effect of not fixing boundary conditions at the outer edge of the grid on the evolution of the trace of extrinsic curvature K.

namely Dirichlet conditions, where we set the time derivatives of our variables to zero at the outer boundary. This obviously violates the Einstein equations, however, as the boundary is far away, the effects will not have time to propagate inward in our running times.

3.3.3 Final Results

Having set our outer boundary conditions, we can now evolve our variables to longer time-scales. Figures 3.8 to 3.16 show the time evolution of our variables up to time scales $t > 0.05$ with the initial trace of the extrinsic curvature set to $K_0 = -0.01$.

As can be seen in Figure 3.8, the trace of the extrinsic curvature reaches zero near the radius of the star. This prevents us from running our code for longer times, for a number of reasons: First and foremost, K crossing zero and becoming positive takes us to the not well-posed regime discussed in Section 3.2.4, and second, the aether pressure given by Eq. (3.67) can not be numerically calculated any more when its numerator and denominator both tend to zero.

While the second problem is purely numerical, the first problem can not be necessarily

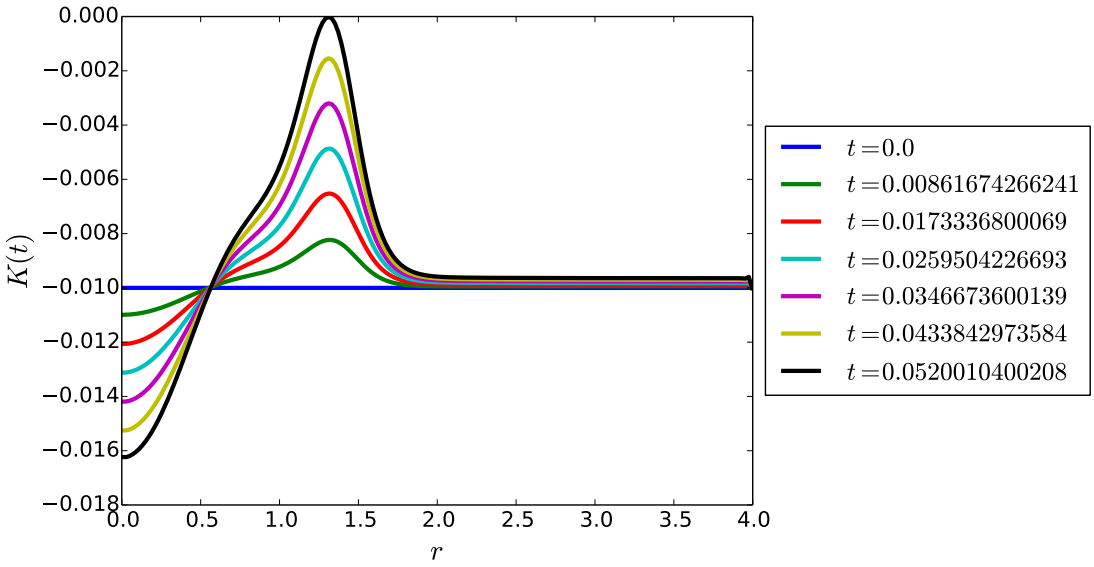

Figure 3.8: Evolution of the trace of the extrinsic curvature K.

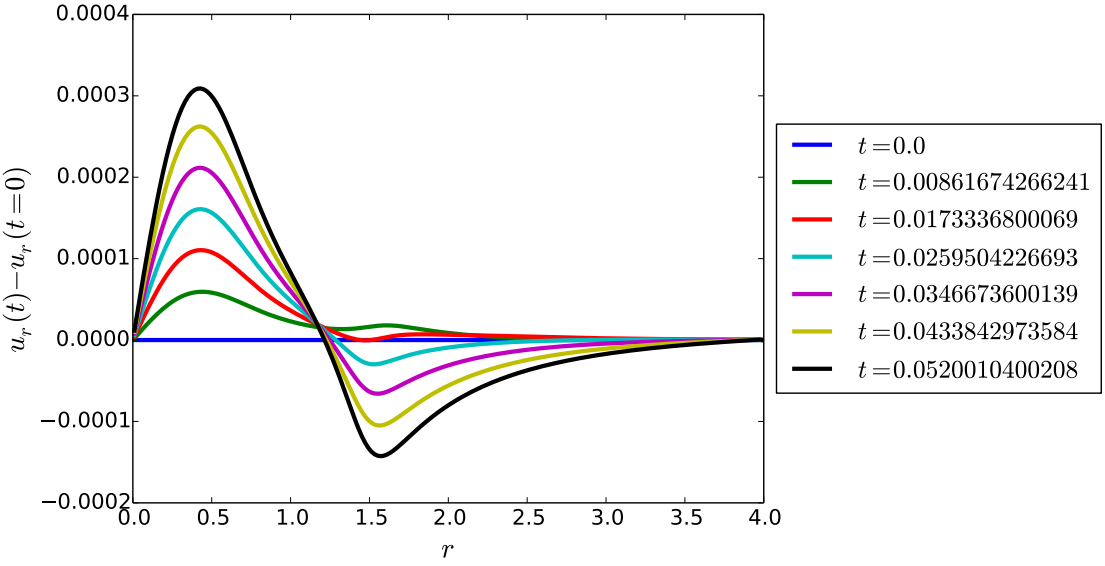

Figure 3.9: Evolution of the radial velocity of matter u_r.

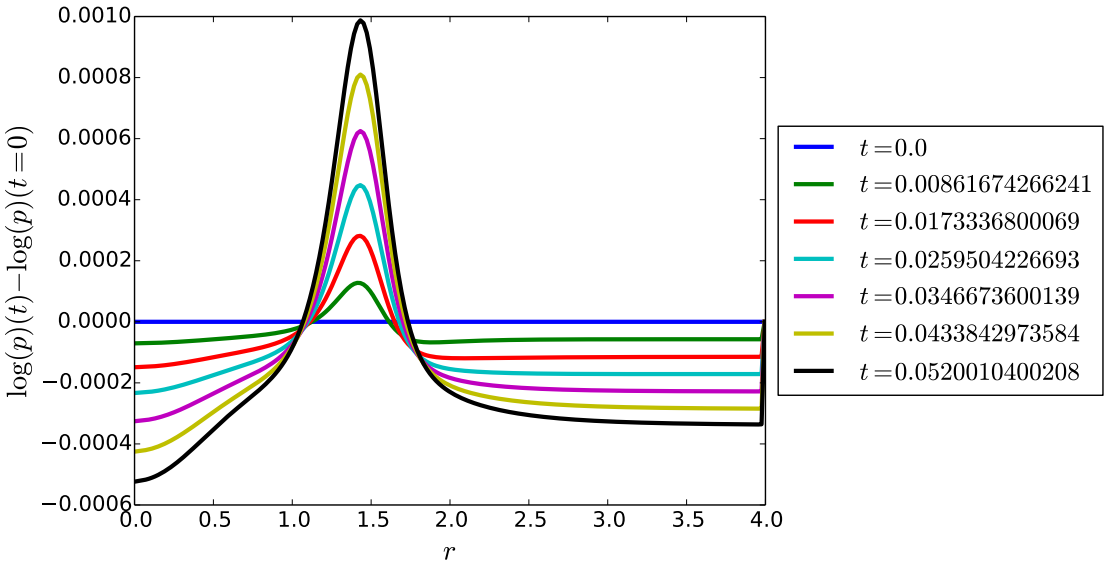

Figure 3.10: Evolution of the log of the pressure of matter p.

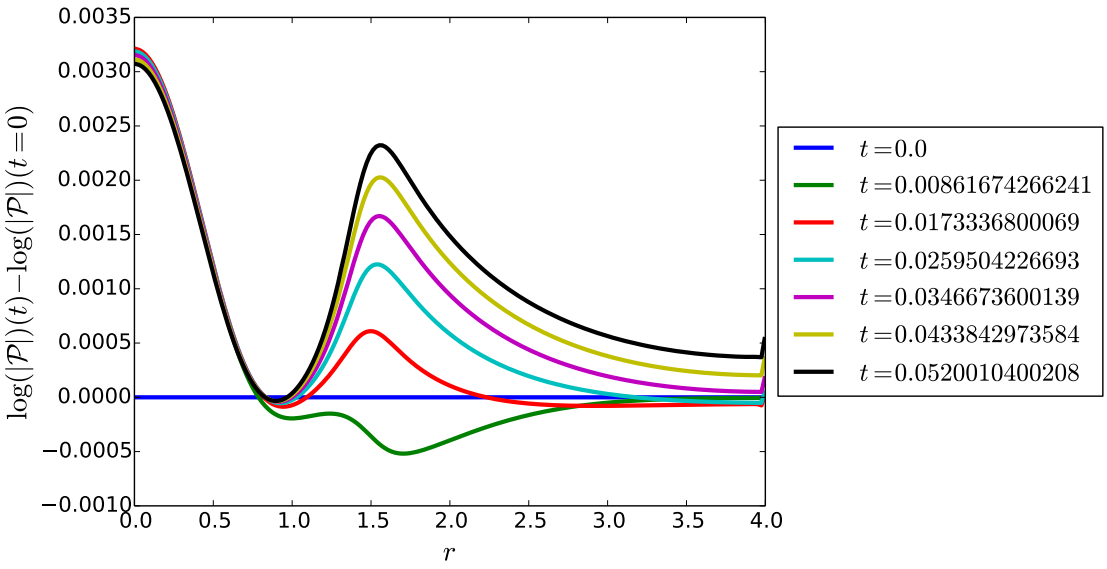

Figure 3.11: Evolution of the log of the absolute value of the aether pressure $\mathcal{P}$ (as $\mathcal{P} < 0$).

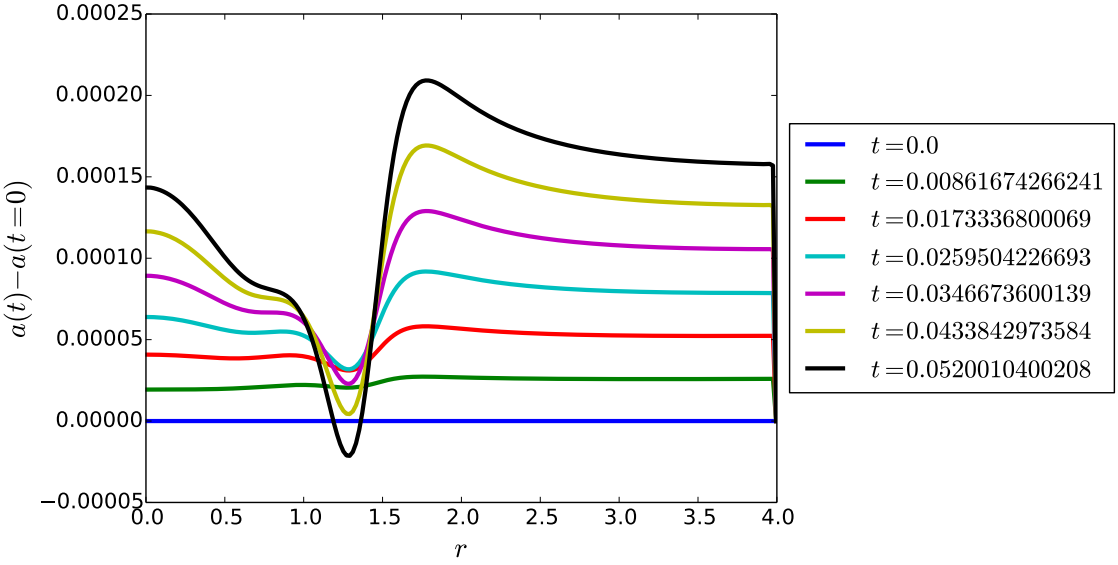

Figure 3.12: Evolution of the metric component a.

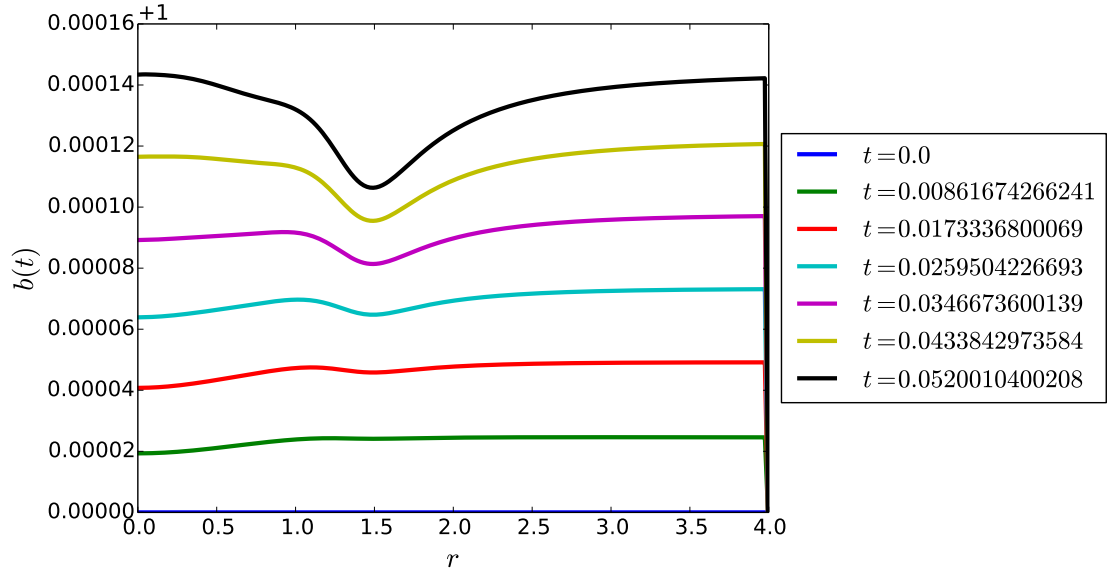

Figure 3.13: Evolution of the metric component b.

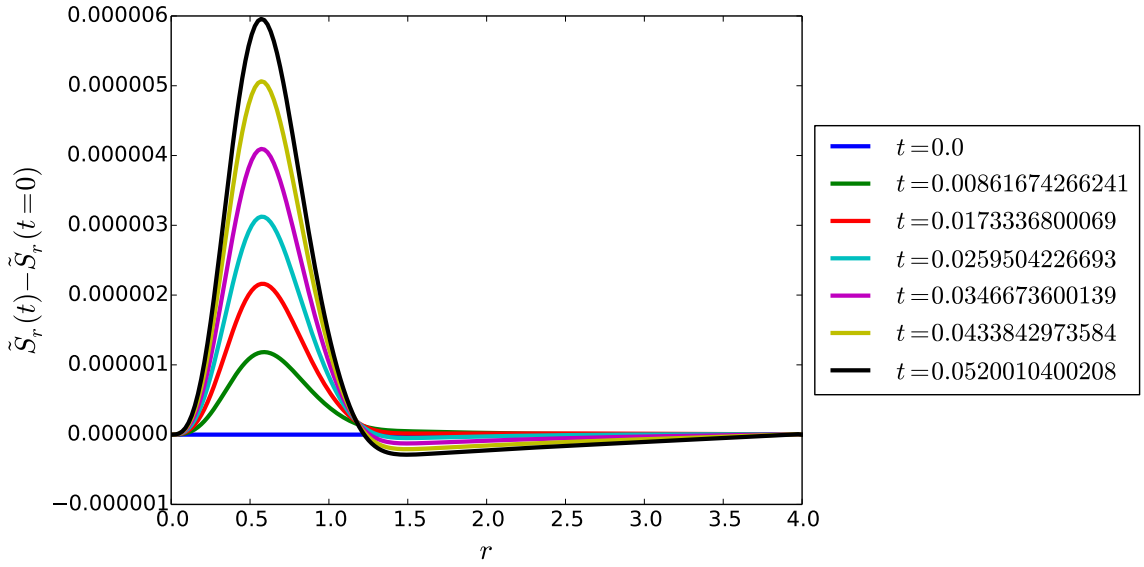

Figure 3.14: Evolution of the state vector component $\tilde{S}_r$.

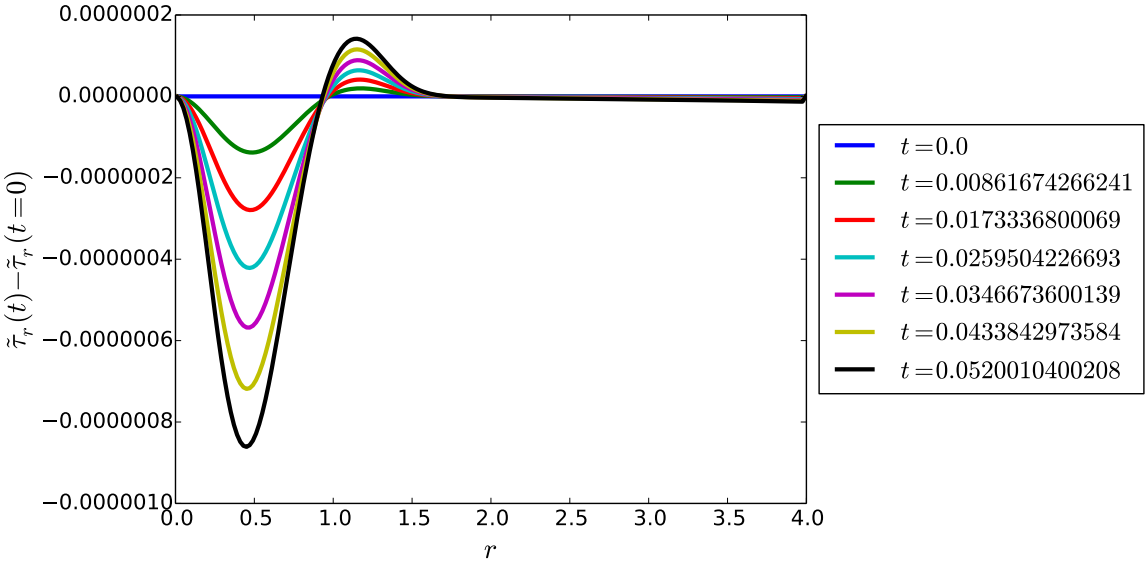

Figure 3.15: Evolution of the state vector component $\tilde{\tau}$.

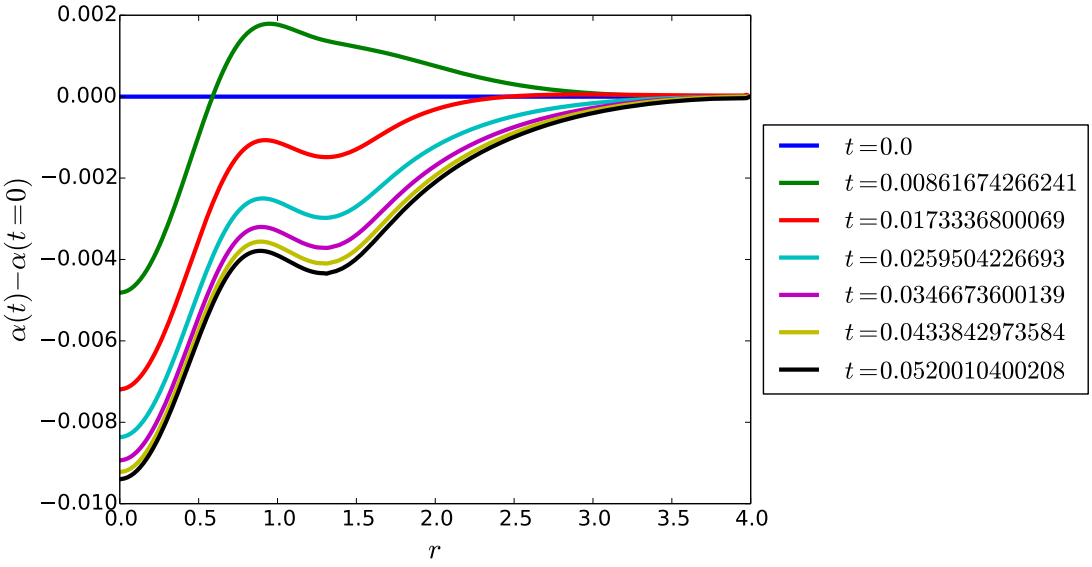

Figure 3.16: Evolution of the lapse function α.

over-come by using numerical techniques and may be a fundamental problem with the theory. We can summarize the problem in the following way: We found that a collapse of matter in the frame of the aether is not well-posed. We also find that starting with expanding conditions, our variables evolve towards a collapse in certain regions of the grid, which is not well-posed.

3.3.4 Convergence Test

A necessary test for the evaluating the validity of our results is a convergence test. We perform this test for one of our most important variables, the trace of the extrinsic curvature. If the grid spacing is given by h, the numerical value of the trace of the extrinsic curvature K_h can be expressed in terms of the true value K as

$$K_h = K + hE_1 + h^2E_2 + h^3E_3 + ... \tag{3.204}$$

The leading term in the above expansion is given by the order of the numerical method as

$$K_h - K \sim h^pE, \tag{3.205}$$

where p is the order parameter. We can therefore write

$$K_{h/4} - K_h \quad = \quad \left[\, (\frac{h}{4})^p - h^p \, \right] E = Eh^p \left[\, (\frac{1}{4})^p - 1 \, \right], \tag{3.206}$$

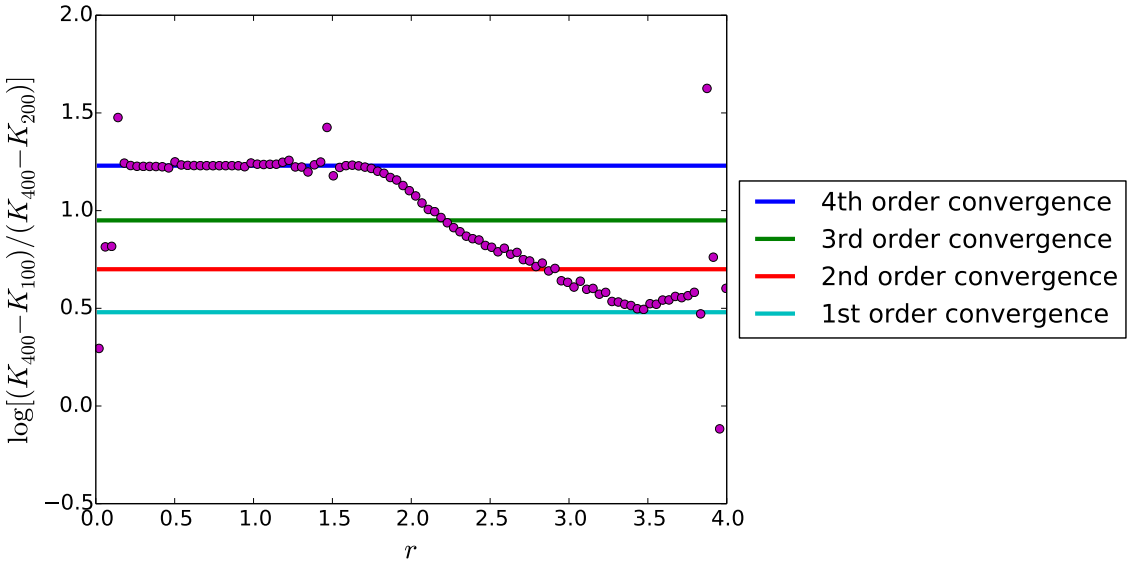

Figure 3.17: The convergence of the trace of extrinsic curvature.

$$K_{h/4} - K_{h/2} \;=\; \left[\ (\frac{h}{4})^p - (\frac{h}{2})^p\ \right]E = Eh^p\left[\ (\frac{1}{4})^p - (\frac{1}{2})^p\ \right]. \tag{3.207}$$

As a result

$$\begin{aligned} \log\left(\frac{K_{h/4}-K_h}{K_{h/4}-K_{h/2}}\right) = \log\left[\frac{(\frac{1}{4})^p-1}{(\frac{1}{4})^p-(\frac{1}{2})^p}\right] &= 0.48 \quad \text{for} \quad p=1 \\ &= 0.70 \quad \text{for} \quad p=2 \\ &= 0.95 \quad \text{for} \quad p=3 \\ &= 1.23 \quad \text{for} \quad p=4 \end{aligned} \tag{3.208}$$

We ran our code with three resolutions of 100, 200 and 400 grid points (where the number of grid points scales inversely with the grid spacing h). Figure 3.17 shows the convergence results for the trace of the extrinsic curvature near the time 0.03 (the K subscripts are now number of grid points). We see that we are obtaining fourth-order convergence inside the star with the exception of the center. The convergence order drops in the atmosphere, which is expected, due to our unphysical outer boundary conditions. The fact we are not seeing convergence at the center of the star is due to our derivative operator's inability to calculate divergences accurately at the center in spherical symmetry. This results in an inaccurate Laplacian (e.g. in Eq. 3.89). This problem will be discussed in more detail in Section 3.5.1.

3.3.5 The Hamiltonian Constraint

One of the equations we are not directly solving in our time evolution scheme is the Hamiltonian constraint (3.78) given by

$$16\pi\mathcal{G}\ {}^{(3)}\rho = R + 4K^r_r K^\theta_\theta + 2K^{\theta 2}_\theta. \tag{3.209}$$

It should stay valid during the course of evolution and therefore serves as a useful verification method for our numerical scheme. We define the dimensionless parameter $\mathcal{H}$ as

$$\mathcal{H} \equiv \frac{\left|16\pi\mathcal{G}\ {}^{(3)}\rho - R - 4K^r_r K^\theta_\theta - 2K^{\theta 2}_\theta\right|}{16\pi\mathcal{G}\ {}^{(3)}\rho}. \tag{3.210}$$

This dimensionless number gives us a fractional measure of the violation of the Hamiltonian constraint at each radius of the grid. At each time step of the evolution, we define a volume averaged quantity $\bar{\mathcal{H}}$ as

$$\bar{\mathcal{H}} \equiv \int \mathcal{H}\ 4\pi r^2 dr \Big/ \int 4\pi r^2 dr. \tag{3.211}$$

Figure 3.18 shows the time evolution of $\bar{\mathcal{H}}$ for three resolutions. We see that the results converge as we go to higher resolution. We also see that we start with an average Hamiltonian constraint violation of less than 0.1955% and the violation decreases as time goes. The initial violation is to be expected, as we are assuming hydrostatic initial pressure and density profiles for the neutron star (in other words profiles satisfying $16\pi\mathcal{G}\ {}^{(3)}\rho = R$) but also assuming an initial extrinsic curvature ($K_0 = -0.01$). The violation is mainly caused by these extrinsic curvature terms in the Hamiltonian constraint. One may argue that a 0.1955% initial violation is small, comforted by the fact its value decreases with time during the evolution of the system.

3.4 Numerical Methods

In this section we consider the problem of solving numerically the equations described so far. We describe general problems that we must consider when solving our problem numerically and how we handle these issues.

3.4.1 Choosing a Derivative Method

The equations described in Section 3.1.3 are, of course, *differential* equations. We solve them by *discretizing* each derivative operator in some way and replacing it by a finite-

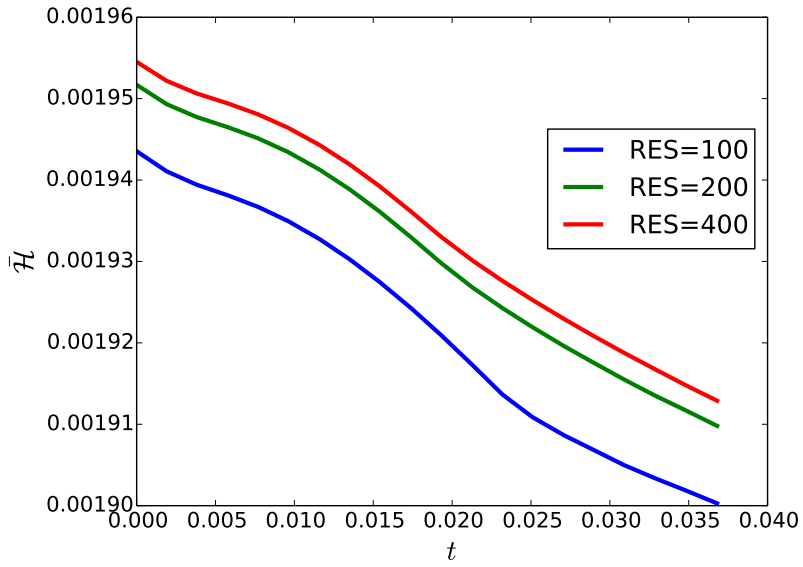

Figure 3.18: The time evolution of the dimensionless variable $\bar{\mathcal{H}}$, giving a volume averaged fractional measure of the violation of the Hamiltonian constraint.

dimensional linear operator. We would like to distinguish between *space-like* derivatives, which are derivatives with respect to the radius r for example, and *time-like* derivatives, which describe evolution in time. For now, we will describe only the space-like derivatives. Our approach for the time-like derivatives will be described in Section 3.4.4. To approximate space-like derivatives, we approximate space as a grid of discrete points, each separated by a distance Δr. At each grid point, we approximate our function as a piecewise p^{th}-order polynomial which interpolates smoothly between the $p/2$ adjacent grid points. The derivative of a polynomial is known and we therefore attain an approximation of the derivative of our quantity of interest. This technique is called *finite differences*.[5]

One important consideration is that, through equations (3.70) and (3.67), the lapse α depends on the aether pressure $\mathcal{P}$, which depends on the derivative of the matter velocity u_r. And through Eq. (3.89), the Laplacian of the lapse appears in our evolution equations. Therefore, *implicitly*, our system of equations depends on the *third* derivative of the matter velocity u_r. We found that this implicit dependence required us to use high-order approximations of our derivative operators, such the error in the derivative operator is of order

[5]There are, of course, other techniques than finite differences. And there are many subtleties to finite differences approximations. Our current technique is relatively naive. We discuss the possible advantages of using more sophisticated techniques in Section 3.5.

$\mathcal{O}(\Delta r^4)$, where Δr is the distance between two discrete grid points. Otherwise we found that this implicit repeated differentiation introduced errors of order $\mathcal{O}(1)$ in our solutions. We therefore chose a fourth-order finite-differences scheme to represent derivatives in all of our quantities (Press et al., 1989).

3.4.2 Approximating Derivatives in Spherical Symmetry

A typical finite differences scheme approximates the computational domain by evenly spaced discrete points separated by a distance Δr. For example, the domain $r \in [0, R_{max}]$ might be approximated as

$$r_i = i(\Delta r),\ i = 0, 1, 2, ..., N$$

such that $r_N = R_{max}$. However, we would like our approximate derivative to respect the symmetry boundary conditions described in Section 3.1.4. To effect this, we use so-called "ghost points." Formally our computational domain is only on the domain $r \in [0, R_{max}]$, and therefore our discrete grid points exist only for $r > 0$. However, we add additional grid points at $r < 0$ and analytically continue all functions to negative r in such a way that satisfies whether they should be even or odd in r. Our derivative operator then correctly uses the correct symmetry (or antisymmetry) to differentiate our functions at or near the origin (Alcubierre & González, 2005). With these additional symmetry conditions a grid $r \in [0, R_{max}]$ would be approximated as

$$r_i = i(\Delta r),\ i = -2, -1, 0, .., N \text{ s.t. } r_N = R_{max}. \tag{3.212}$$

for reasons that will become clear, we call this our *unstaggered grid.*

An additional difficulty in spherical symmetry is that many quantities (in particular, the primitive hydrodynamic variables) are define as

$$f(t, r) = \frac{g(t, r)}{r^p},$$

where $p > 0$ is some power and f and g are functions such that g/r^p has a well defined limit as $r \to 0$. This is not a problem analytically, but we must decide how to calculate f at $r = 0$ given $g(t, r)$. One strategy is to use L'hopital's rule so that

$$f(t, r = 0) = \frac{1}{p!} \frac{\partial^p}{\partial r^p} g(t, r) \bigg|_{r=0}.$$

Another strategy is to use the symmetry properties of the function. We can analytically continue $f(|r|)$ to $f(-|r|)$, which is well defined, and approximate $f(r = 0)$ by the polynomial that interpolates to $f(r)$ near the origin, i.e., for $0 < |r| < \epsilon$ for some $\epsilon > 0$. Both

of these approaches induce an error at the origin which, depends on the accuracy of the derivative operator or the polynomial interpolant.

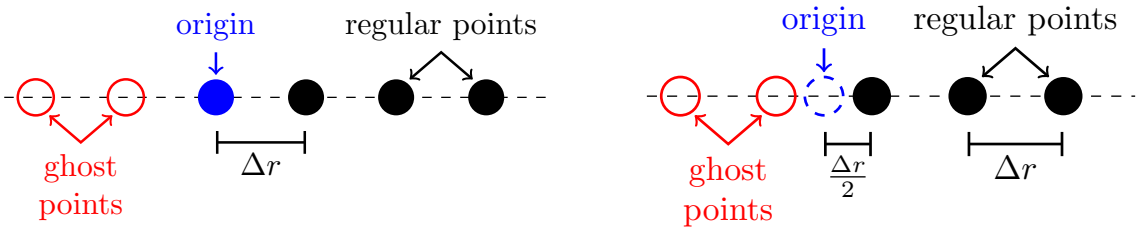

(a) The unstaggered grid.

(b) The staggered grid.

Figure 3.19: Our unstaggered and staggered grids. Both grids approximate our continuous variable r as a discrete set of points, separated by Δr. However, the unstaggered grid includes the origin while the staggered grid does not. This Figure was made by Jonah Miller.

We can also avoid this regularization problem entirely by *removing* the origin from the computational grid. In this case, we don't approximate $r \in [0, R]$. We approximate $r \in (, R]$. To keep the distance between all grid points the same, we *stagger* our grid about the origin (Alcubierre & González, 2005). We therefore approximate the domain $r \in (0, R]$ as

$$r_i = i(\Delta r),\ i = -\frac{3}{2}, -\frac{1}{2}, \frac{1}{2}, ..., N \text{ s.t. } r_N = R_{max}. \tag{3.213}$$

Figure 3.19 schematically compares the staggered and unstaggered grids. The staggered grid allows us to avoid regularizing quantities, and therefore additional errors, at the origin. However it makes analyzing our numerical solutions for different Δr more difficult, since the grid points r_i don't line up with each other. Our current implementation uses a staggered grid.

3.4.3 Integrating in Space

When solving for the initial data and when solving for the auxiliary variables 3.105, we often solve ODE systems of the form

$$\frac{d\mathcal{Y}}{dx} = \frac{\mathcal{A}(x, \mathcal{Y})}{\mathcal{B}(x, \mathcal{Y})} \tag{3.214}$$

such that $\mathcal{A}(x_0, \mathcal{Y}) = \mathcal{B}(x_0, \mathcal{Y}) = 0$ for some $x = x_0$. If $\mathcal{A}/\mathcal{B}$ has a well defined limit as $x \to x_0$, then there is no problem analytically. However, if we wish to solve Eq. (3.214) in the neighborhood of x_0, we need to regularize somehow.

A generic solution is to solve the related equation

$$\mathcal{B}(x, \mathcal{Y})\frac{d\mathcal{Y}}{dx} = \mathcal{A}(x, \mathcal{Y}) \tag{3.215}$$

for $\mathcal{Y}$. To solve (3.215), we use the so-called *direct method* (Press et al., 1989). In this approach, we put x on a grid and approximate our derivative as described and in Section 3.4.2. This transforms the *differential* Eq. into a *linear system* of equations–one for each grid point–which we solve using a standard root-finding method such as the Newton-Raphson method (Press et al., 1989). We note that the solution to Eq. (3.215) may be highly non-unique at $x = x_0$. However, because our discrete approximation of the derivative operator is non-local, the solution at $x = x_0 + \Delta x$ depends on the solution at $x = x_0$ and the *discrete* version of the equation becomes unique. Importantly, if x is a radial coordinate, this technique respects the spherical symmetry conditions at the origin.

3.4.4 Integrating in Time

To evolve our system in time, we use the method of lines Press et al. (1989). By putting our system on a grid and approximating our space operator, we transform our partial differential equation into a coupled system of ordinary differential equations for the state vector (3.91) at each grid point r_i. We solve this system using a standard numerical integrator such as an explicit (or implicit) Runge-Kutta method Press et al. (1989). Note that each time we calculate the right-hand side of Eq. (3.90), we must also calculate the quantities (3.105). We currently use the explicit fourth-order adaptive Runge-Kutta method developed by Dormand & Prince (1980).

3.5 Future Numerical Improvements

The results so far presented in this chapter are products of on-going work. Here we describe the potential improvements we would like to see in our numerical approach.

3.5.1 Summation By Parts in Spherical Symmetry

Consider the first-order hyperbolic system of equations,

$$\partial_t \mathcal{Y} = M^i \partial_i \mathcal{Y}, \tag{3.216}$$

where each M^i is a matrix and $\mathcal{Y}$ is a large collection of functions of both space and time which we are interested in evolving. One powerful way to prove that system (3.216) is well-posed is to find an *energy norm*. Roughly, an energy norm is a non-negative functional that depends in a non-trivial way on every component of $\mathcal{Y}$. If one can find such an energy norm and show that it is *non-increasing*, then the energy[6] is bounded from above and below and the system 3.216 is *symmetric hyperbolic* and thus well-posed Alcubierre (2008). If a suitable energy norm can be found, the proof that it is non-decreasing usually relies heavily on integration by parts,

$$\int_a^b u dv = uv\Big|_{a^b} - \int_a^b v du, \tag{3.217}$$

where u and v are arbitrary functions, which plays a key role in translating information encoded in Eq. (3.216) into information about the time evolution of the energy norm.

The discrete analog of well-posedness is *stability*. If a continuum equation is ill-posed, it holds little predictive power. Similarly, if the discrete approximation of a continuum equation is unstable, there is little hope of solving it numerically. One way to show that the discrete approximation of a symmetric hyperbolic system is well-posed is show that the discrete approximation of the corresponding energy norm is non-decreasing. And a key tool in proving that the discrete energy is non-decreasing is the discrete analog of integration by parts, *summation by parts* (SBP):

$$\sum_{i=0}^{N} w_i \left[u_i (Dv)_i + (Du)_i v_i\right] = u_N v_N - u_0 v_0, \tag{3.218}$$

where $u_i = u(r_i)$ and $v_i = v(r_i)$ are the discrete approximations of u and v, D is a discrete approximation of a derivative operator, and w_i is a weight matrix such that the sum $\sum_i w_i f_i$ is an approximation of the integral $\int f(r) dr$ (Strand, 1994). Therefore, to ensure stability, it is highly desirable that any discrete derivative operator satisfy summation by parts.

[6] The energy norm does not have to correspond to a physical energy. It just has to be a non-negative functional.

As described in Section 3.4.1, we use a standard fourth order finite differences operator. In Cartesian coordinates, this operator satisfies summation by parts in the bulk and only requires modification at the boundaries of the domain. Unfortunately, in spherical coordinates, this is not the case. This means that special care must be taken to ensure stability of our system. In particular, the Laplacian operator in spherical coordinates requires special care and must be regularized analytically in some way. Unfortunately, as of the writing of this chapter, we have not found a way to regularize the Laplacian of the lapse α as it appears in Eq. (3.89). This means our solutions may diverge in finite time.

Recently, in the context of the wave equation in spherical coordinates, Gundlach et al. (2013) derived a modified fourth-order finite differences approximation of the Laplacian operator that satisfies summation by parts in spherical symmetry. We would like to modify our scheme to utilize this operator, which we hope will provide improved stability and robustness.

3.5.2 High-Resolution Shock Capturing

The relativistic Euler equations are prone to shocks, discontinuities in the velocity, density, or pressure. These shocks, naturally, present numerical difficulties. High-order finite differences approximations of shocks tend to exhibit instabilities and numerical ringing (Press et al., 1989). This can be cured by artificial dissipation—special linear operators which pull energy out of the system without disturbing the continuum limit—but at the price of accuracy. The shock smoothes out and spatial resolution near the shock is lost.

We would like to have the capacity to capture shocks: partly because one may develop, and partly because the surface of a star is very much like a shock and tracking the surface with high resolution is essentially shock capturing.

The typical solution is to use first and second-order high-resolution shock-capturing schemes. These methods reduce the evolution of a system to a series of Riemann problems (Toro, 2009), which are toy models for a hydrodynamical shock with an exact analytic solution. Unfortunately, because our system implicitly depends on third-order derivatives in space, low-order methods are not an option. This is why we are using a fourth-order finite differences scheme, as described in 3.4.1.

There are, however, high-order methods capable of capturing shocks. Perhaps the most straightforward technique is to use the high-order weighted essentially non-oscillatory (WENO) finite differences methods developed by Liu et al. (1994) based on the work of Harten & Osher (1987) and others. These derivative operators respect conservation laws

in such a way that shocks are accurately represented without excess artificial dissipation.[7]

Another approach is to change, on a fundamental level, the approximation we make of our function and the system it should solve. Spectral methods approximate a function u as a linear combination of known, *globally defined* basis functions, in which case the derivative of u is analytically know. Spectral methods can attain so-called *evanescent accuracy* where the numerical error in a solution decays exponentially as a function of the number of modes used (Grandclément & Novak, 2009). This has obvious advantages in a case where low-order derivatives are highly undesirable.

Unfortunately, spectral methods are also notoriously bad at handling discontinuous solutions, including shocks. Indeed, spectral representation of a function with a shock will suffer $\mathcal{O}(1)$ errors. This is because, at their heart, spectral methods rely on a Fourier series expansion, and a Fourier series develops $\mathcal{O}(1)$ errors in the presence of a discontinuity. This is the well-known Gibbs phenomenon (Tadmor, 1989).

However, in a series of papers Gottlieb et al. (1992) developed a technique for removing the $\mathcal{O}(1)$ errors in post-processing, after a simulation has been run. Combined with other techniques such as the spectral viscosity developed by Tadmor (1990) and spectral edge detection developed by Gelb & Tadmor (1999), this opens the door to spectral simulations of shocks with evanescent accuracy.

These techniques are an active area of research and not yet robust. In particular, the post-processing requires foreknowledge of the position of the shock, which is difficult to attain in more than one dimension (Parfrey et al., 2012). For the moment, however, our problem is a one-dimensional problem. This makes it an ideal application for these powerful techniques. We note that spectral methods offer us significant flexibility in terms of representing our system. We can choose spectral basis functions that respect spherical symmetry and, if we like, extend all the way to $r = \infty$. Therefore, if we need additional accuracy, spectral methods are extremely appealing.

3.5.3 Implicit Time Stepping

As derived Section 3.2.4, the character of the evolution Eq. (3.89) for the extrinsic curvature K is not necessarily hyperbolic. In particular, at the origin and near hydrostatic equilibrium, the equation is indeed *parabolic*, i.e., like the heat equation

$$u_{,t} = k u_{,xx}.$$

[7] For a review, see the article by Shu (2003).

As described in Section 3.4.4, we use an explicit Runge-Kutta integrator to integrate in time. Unfortunately, because information propagates infinitely fast through a parabolic system, the stability of an explicit integration parabolic system depends very strongly on the discrete time steps one takes as one advances in time; the time steps must be much smaller than for a hyperbolic system. This make computation time extremely long.

One remedy to this is to integrate in time *implicitly* Press et al. (1989). Consider the simple ordinary differential equation

$$\frac{d}{dt}y = f(t, y). \tag{3.219}$$

We can discretize the derivative on the left-hand-side of Eq. (3.219) by taking Newton's definition and simply failing to take a limit:[8]

$$\frac{dy}{dt} = \frac{y(t + \Delta t) - y(t)}{\Delta t}$$

so that Eq. (3.219) becomes

$$\frac{y(t + \Delta t) - y(t)}{\Delta t} = f(t, y). \tag{3.220}$$

To step forward in t, we simply solve Eq. (3.220) for $y(t + \Delta t)$. However, there is an ambiguity in Eq. (3.220): at what time do we evaluate the right-hand-side, $f(t, y)$. We have two choices. We could solve the equation

$$\frac{y(t + \Delta t) - y(t)}{\Delta t} = f(t, y(t)), \tag{3.221}$$

or we could solve the equation

$$\frac{y(t + \Delta t) - y(t)}{\Delta t} = f(t + \Delta t, y(t + \Delta t)). \tag{3.222}$$

Both choices are equally valid because they have the same limit as $\Delta t \to 0$. Solving Eq. (3.221) leads to a *explicit* scheme, while solving Eq. (3.222) leads to a *implicit* scheme. The two schemes described here are first-order. However higher-order, more accurate schemes can be constructed (Press et al., 1989).

Implicit schemes are more robust in the sense that they are often stable (as described in Section 3.5.1) no matter how large Δt is.[9] However, implicit schemes also often involve

[8] There are more sophisticated ways to take a derivative. We use this method simply as a clear example.

[9] Note that this does not mean they are *accurate* no matter the size of Δt! The accuracy of an implicit scheme depends on Δt and on the order of the method, just like an explicit scheme.

solving a large system of linear equations and they can therefore be computationally costly. Therefore, the choice between using an implicit and explicit scheme for time integration is a balance between stability and computational cost. If a system is purely hyperbolic, explicit schemes are usually better. However, we know that our system is not purely hyperbolic. We may therefore gain the ability to take substantially larger time steps and evolve our system in much less walltime by using an implicit scheme.

3.6 Conclusions and Future Prospects

In this chapter, we have studied the dynamics of a neutron star in the gravitational aether theory. As the theory violates Lorentz invariance, it introduces a preferred frame. This preferred frame which is the frame of the aether is a logical choice of a coordinate system. Going in the frame of aether, along with setting the shift vector to zero, gives the lapse function based on the aether conservation equations and fully determines the gauge. We formulated our equations in standard form suitable for numerical evolution. The hydrodynamical equations were put in a flux-conservative form ensuring numerical stability. We work in spherical symmetry ensuring that even functions have zero radial derivatives at the origin and odd functions have zero values at the origin. As outer boundary conditions, we chose Dirichlet conditions, setting the time derivative of our variables to zero at the outer boundary. Due to adding an atmoshere to the star, the outer boundary is sufficiently far so that the effects of unphysical conditions at this boundary do not propagate inside in our running times. We chose an equilibrium configuration of a neutron star as our initial condition, perturbing it by adding a small extrinsic curvature (and thus by adding radial velocity). In finding our hydrostatic configuration, we improved the method used in Chapter 2, by deriving the Tolman-Oppenheimer-Volkoff equations for the aether theory. By analyzing the nature of our equations near hydrostatic equilibrium, we found a diffusion-type equation that is well-posed when matter is expanding in the frame of the aether and not well-posed when matter is collapsing. This finding constrained the choice of initial conditions to the expanding mode.

Using the numerical methods described in Section 3.4, we evolved our system of equations based on the evolution algorithm described in Section 3.3.1 up to a time $t \sim 0.052$ in units where $G_N = 1$, $c = 1$ and the polytropic EOS factor $K = 1$. Near this time, the trace of the extrinsic curvature crosses zero. We can not presently evolve past this point. The reasons for this may be numerical or more fundamentally rooted in the physics of the theory. Numerically, when the trace of the extrinsic curvature goes to zero, the time derivative of the energy density (or the value of Ω_0) also goes to zero, and therefore it

becomes challenging to calculate the value of the pressure of aether given by Eq. (3.67) as it goes to 0/0. This is a numerical issue, as there is a well-defined limit to this ratio.

A more fundamental issue however is that starting in the well-posed (expanding matter in the frame of aether) mode, we seem to be evolving towards the not well-posed regime (collapse).

To evaluate the validity of our numerical results, we performed a convergence test and found that inside the star (with the exception of the origin), we are achieving fourth-order convergence. The problem at the origin is related to our derivative operator's not giving a good apporximation of the divergence (and thus of the Laplacian) at the origin. This, as mentioned in Section 3.5.1 can be resolved, taking into account the recent results of Gundlach et al. (2013) that derived a modified fourth-order finite differences approximation of the Laplacian operator that satisfies summation by parts in spherical symmetry. We also calculated the volume averaged fractional measure of the violation of the Hamiltonian constraint, and saw the constraint is violated at most by 0.2% and the violation decreases with time.

In addition to improvements in our numerical methods mentioned in Section 3.5, an immediate next step for this work would be to compare these results, with the results from General Relativity. To do this, we can for example, calculate a frame-independent scalar variable such as the redshift at the surface of the star, both in General Relativity and in the aether theory. In Section 3.1.1, we mentioned that the aether theory can be generalized, replacing the 1/4 factor in the Einstein field equations with a more general λ parameter. Taking λ to zero would smoothly move the theory towards General Relativity. The numerical results reported in this chapter were for $\lambda = 1/4$ for which the aether theory solves the old comsological constant problem. One could calculate a range of results for different values of λ and verify that the results tend towards General Relativity in the $\lambda \to 0$ limit. A possible numerical complication is that in the $\lambda \to 0$ limit, our current gauge conditions become ill defined as we are in the frame of aether, and aether's pressure vanishes in this limit. Therefore, as one moves towards $\lambda \to 0$ the gauge freedom increases and needs to be taken into consideration.

One of the main outcomes of this work has been to find that the regime of collapse of matter in the aether frame is not well-posed. A similar feature of the aether had been previously found in the context of perturbation theory for FRW cosmology by Aslanbeigi et al. (2011). Our results confirm that earlier finding on numerical grounds. However, the main achievement in this work, has been to establish that a Cauchy problem can be defined for the aether theory, and the aether equations can be evolved numerically in the expanding mode up to a time when one enters the collapse mode. Evolving towards the not well-posed

regime (collapse), would pose a serious challenge to our initial value formulation of the aether theory. Of course, whether an alternative formulation can handle the collapsing neutron stars is a question of utmost importance for the viability of the aether theory.

Chapter 4

The Mass and Radii of Strongly Magnetized Neutron Stars

The purpose of this chapter is to study the effect of various assumptions about the nature and configuration of the magnetic field (in particular, the force-free model of Broderick & Narayan, 2008) on the M-R distribution of neutron stars. For the effects of the magnetic field on the nuclear EOS, we base our work on the calculations of Broderick et al. (2000, 2002) which will be briefly described in Section 4.1. In Section 4.2 we will motivate the particular magnetic field profile we consider, based on a simplified model of neutron star formation and magnetic field amplification that results in a local magnetic field strength fixed to a fraction of the equipartition value. By varying the fraction of equipartition we are able to study the effect of different field strengths on the M-R distribution. In Section 4.3 we will calculate the M-R relation of neutron stars, assuming different strengths of a statistically isotropic magnetic field, based on different models for the nuclear EOS. In Section 4.4 we will study the structure of neutron stars with a force-free magnetic field profile (which is anisotropic). Finally, we will conclude in Section 4.5.

4.1 Magnetized Nuclear Equation of State

In this work, we employ the EOS calculated by Broderick et al. (2000), which includes the effects of very strong magnetic fields in multicomponent, interacting matter. This is obtained via a field-theoretical approach in which the baryons (neutrons, n, and protons, p) interact via the exchange of σ-ω-ρ mesons. They consider two classes of models that differ

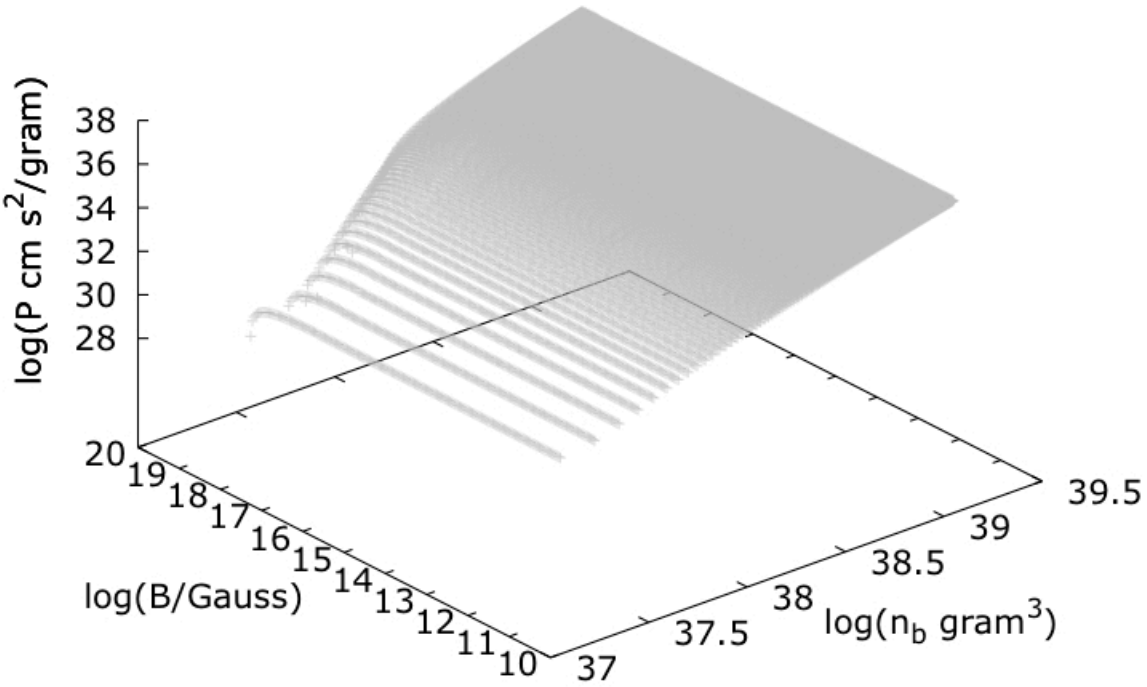

Figure 4.1: EOS - pressure (P) versus number density of baryons (n_b) for different values of the magnetic field strength (B) assuming no anomalous magnetic moments. Strong magnetic fields soften the EOS because of Landau quantization.

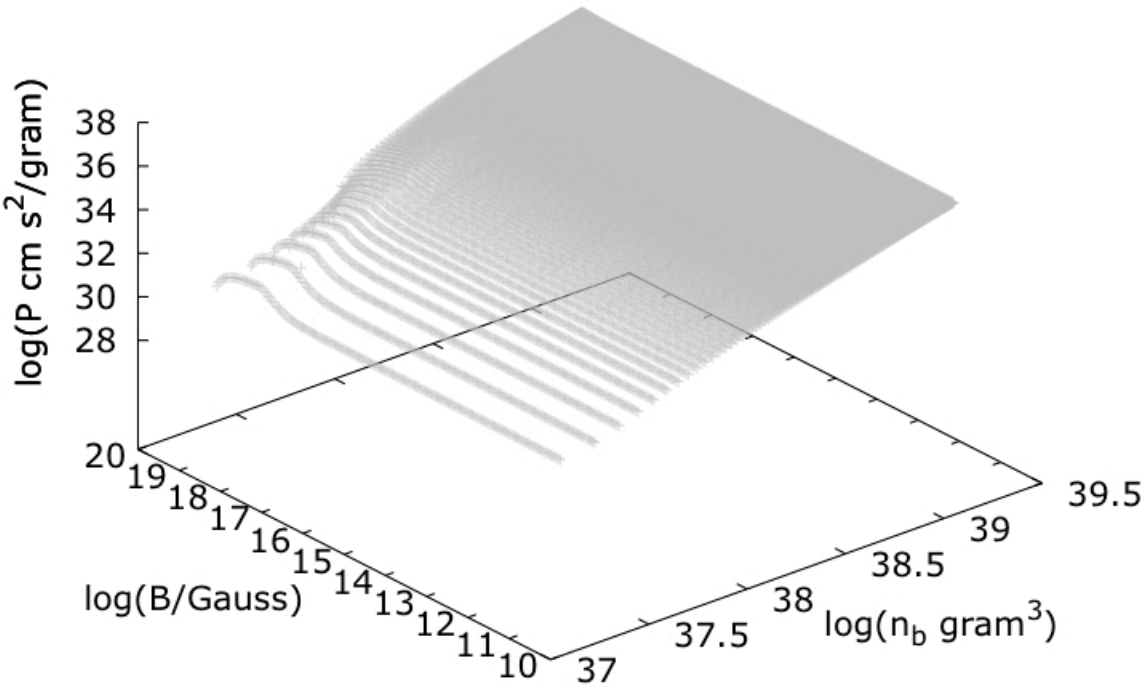

Figure 4.2: Same as Fig. 4.1, but now including the effect of anomalous magnetic moments. The magnetic field stiffens the EOS due to the polarization of the anomalous moments until complete spin polarization occurs ($B > 10^{18}$ G). From that point on, the effect of Landau quantization takes over and softens the EOS.

in their high densities behavior. In these models, the effects of the anomalous magnetic moments of the nucleons are introduced via a covariant coupling of the baryons to the electromagnetic field tensor, presumed to be the result of of an appropriate high-energy theory. The magnetic fields affect the EOS in two ways. In strong fields ($B > 10^{14}$ G), the orbital motion of the charged particles is quantized (Landau quantization), resulting in a reduction in the electron chemical potential and a substantial increase in the proton fraction. This produces a softening of the EOS. However, if the anomalous moments are considered, the authors find that for very strong fields ($B > 10^{18}$ G), complete spin polarization of the neutrons occurs. This produces an overall stiffening of the EOS that overwhelms the softening induced by Landau quantization. These effects are illustrated in Figures 4.1 and 4.2.

Broderick et al. (2002) have also studied the effects of hyperons on the magnetic EOS. Their EOS with hyperons, in the absence of a magnetic field is equivalent to the GM3 EOS calculated by Glendenning & Moszkowski (1991) where hyperons are introduced as free baryons, interacting only through weak interaction so that the system maintains nuclear statistical equilibrium. Typically, the introduction of the additional degrees of freedom associated with the new baryon species produces a net softening of the equation of state.

Since the pressure is now generally a function of both the matter density and magnetic field strength, explicit construction of a neutron star requires some knowledge about the magnetic field profile.

4.2 A Tangled Magnetic Field

The primary processes responsible for the amplification of the magnetic field are believed to be dynamos driven by differential rotation and convection Duncan & Thompson (1992); Thompson & Duncan (1993). These necessarily produce a tangled magnetic field inside the neutron star. Since for simplicity we assume spherical symmetry throughout this work, we must model the dependence of the strength of this tangled magnetic field on radius. We do this approximately by making a handful of simplifying assumptions regarding the outcome of the dynamo process.

As we discussed in the Introduction, various studies suggest that the dynamos naturally saturate at locally equipartition magnetic field strengths during the initial formation of a proto-magnetar (e.g., Price & Rosswog, 2006; Naso et al., 2008). That is, we expect the energy density in the magnetic field, ϵ_B, to be proportional to that in the gas, ϵ_g:

$$\epsilon_B \propto \epsilon_g. \tag{4.1}$$

Since $P_g \approx \epsilon_g/3$ at this time, this immediately implies

$$\beta \frac{B^2}{8\pi} = P_g, \tag{4.2}$$

where β is the standard proportionality factor relating the gas and magnetic pressures.

As the proto-magnetar cools, β will be approximately conserved. During the cooling process the star will maintain hydrostatic equilibrium and hence for each spherical shell within the star

$$\frac{P_g}{r} \sim \rho \frac{GM}{r^2}, \tag{4.3}$$

where r is the shell radius, M is the enclosed mass, ρ is the matter density, and G is Newton's constant. Assuming that the magnetic field has grown sufficiently strong to suppress any further convection, M will remain constant and the proto-magnetar will contract homologously. Thus ρ will grow roughly proportional to r^{-3} during the subsequent proto-magnetar evolution, and thus $P_g \propto r^{-4}$. Similarly, the flux conservation implies B will grow $\propto r^{-2}$, and thus $B^2/8\pi \propto r^{-4}$ as well. Therefore, we expect β to remain fixed during the proto-magnetar's formation following the quenching of the dynamos.

This relation naturally provides a profile for the magnetic field which is proportional to the pressure of matter; given a global value of β we may identify a unique pressure at each density. Examples of the EOS found by imposing Eq. (4.2) on the results of Broderick et al. (2000) assuming anomalous magnetic moments are shown in Figure 4.3.

In addition to the modification of the nuclear equation of state, the strong interior magnetic fields may produce magnetic stresses directly. However, the nature of these stresses depend on the local geometry of the field as well as its strength. Assuming that the outcome of the dynamo processes is a small-scale, tangled field that is weakly uncorrelated with the generating currents, the resulting stresses may be completely described by a magnetic pressure, which after assuming statistical isotropy is given by

$$P_B = \frac{1}{3} \frac{B^2}{8\pi}. \tag{4.4}$$

The factor of 1/3 arises from the impact of magnetic tension; that it must be present is immediately evident from the fact that the electromagnetic stress-energy tensor is traceless. In Eq. (4.2), $\beta = 1/3$ (giving the EOS lying between the cyan and blue curves in Figure 4.3), corresponds to a neutron star with equal pressure of magnetic field and matter. Smaller values of β, for which the pressure of the magnetic field will be larger than the one of matter, are not generically expected in turbulent MHD dynamos, as magnetic energy is

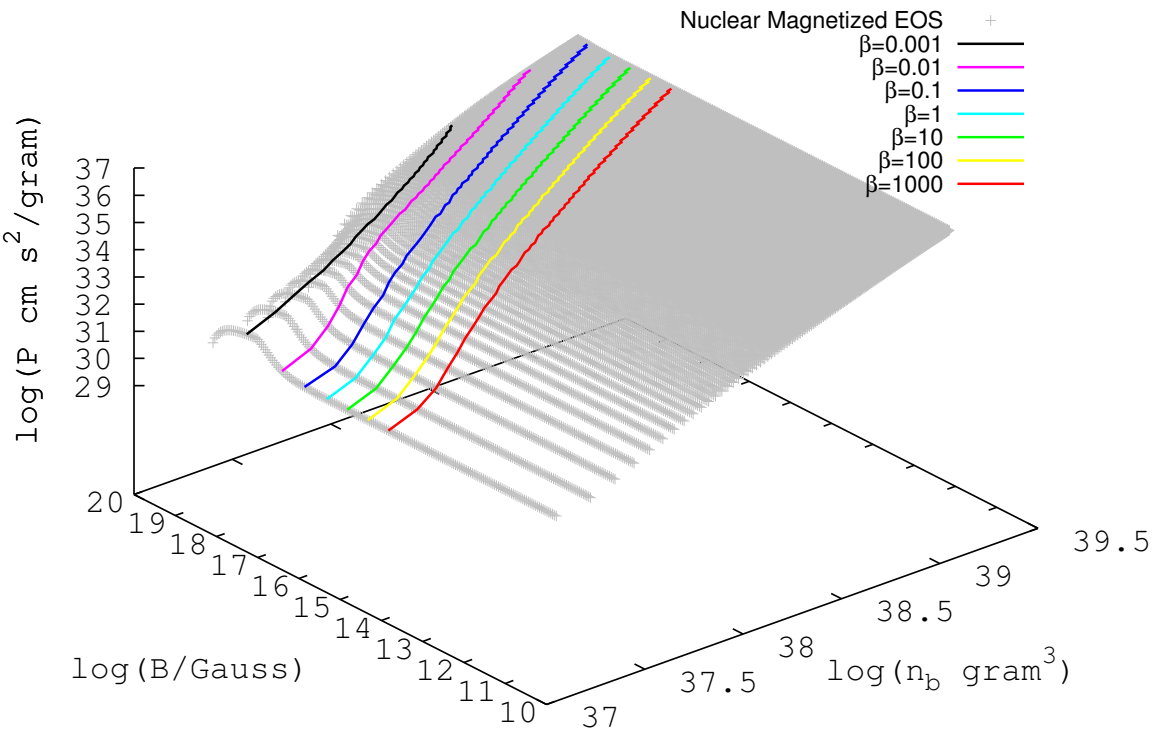

Figure 4.3: EOS - pressure (P) versus number density of baryons (n_b) for different values of the magnetic field strength (B) assuming the existence of magnetic anomalous moments. The solid lines are the EOS found by imposing the equipartition condition (Eq. 4.2) using different values of β. Smaller values of β are associated with higher values of magnetic field strength.

converted back into thermal energy through magnetic reconnection. As we see in Figure 4.3, complete spin polarization of neutrons (due to their anomalous magnetic moments) occurs at $\beta = 0.001$. Therefore, it is expected that at values of β equal to, or larger than $1/3$, the anomalous magnetic moments will not have a considerable effect on the nuclear EOS and consequently in the M-R relations. We will see this explicitly in the next section.

We note in passing that the assumptions made above regarding the correlation between the generating currents and the magnetic field need not be typically satisfied. An extreme alternative are the force-free configurations described in Broderick & Narayan (2008), with a corresponding impact on the nature of the magnetic stresses. However, we will postpone a detailed discussion of this until Section 4.4.

Before describing our M-R calculation, it is worth mentioning that the magnetized EOS of Broderick et al. (2000, 2002) describes the nuclear matter inside the neutron star. For the crust, i.e., densities below the nuclear saturation density (baryon rest-mass density of $\rho_{\rm ns} \sim 2.7 \times 10^{14}$ g cm^3), we use the SLy (Skyrme Lyon) EOS calculated by Douchin & Haensel (2001), which is based on the effective nuclear interaction SLy of the Skyrme type, which is useful in describing the properties of very neutron rich matter.

4.3 M-R relations with an isotropic magnetic field

As choosing a magnetic field configuration given by Eq. (4.2), allows us to calculate a unique magnetized EOS (as seen in Figure 4.3), we can now proceed to calculating M-R relations for neutron stars. As we are assuming spherical symmetry and isotropy, the Einstein equations in hydrostatic equilibrium, simplify to the Tolman-Oppenheimer-Volkoff (TOV) equation:

$$\frac{dP}{dr} = -\frac{G}{r^2}\left[\epsilon + \frac{P}{c^2}\right]\left[M + 4\pi r^3 \frac{P}{c^2}\right]\left[1 - \frac{2GM}{c^2 r}\right]^{-1}, \tag{4.5}$$

where c is the speed of light, and ϵ and P are the total energy density and pressure:

$$\epsilon = \epsilon_g + \epsilon_B, \tag{4.6}$$

$$P = P_g + P_B, \tag{4.7}$$

where ϵ_g and P_g (the energy density and pressure of the gas), are related by imposing Eq. (4.2) (with a fixed choice of β), on the various magnetized nuclear EOS models of Broderick et al. (2000, 2002) (as shown in Figure 4.3 for one particular nuclear EOS). Where stated we include the physics of the crust, by using the SLy EOS of Douchin & Haensel (2001)

below nuclear saturation density. The energy density of the magnetic field is given by $\epsilon_B = B^2/8\pi$, where again B is fixed by the choice of β. The pressure of the magnetic field is given by Eq. 4.4 (statistically isotropic force-inducing magnetic field). The mass enclosed inside radius R is is related to local energy density by

$$M(R) = \int_0^R \epsilon(r)\ 4\pi r^2 dr. \tag{4.8}$$

We integrate Eq. (4.5) numerically, starting from the centre of the star and assuming different values of central pressure $P_g(r = 0)$. Figure 4.4 shows the M-R relations resulting from this integration in the absence of hyperons and crust physics. Increasing the magnetic field strength (decreasing β) in the absence of hyperons has only a small effect on the neutron star maximum mass. However, larger magnetic field strengths are associated with larger neutron star radii.

Figure 4.5 shows the M-R relations in the presence of hyperons, again ignoring the crust physics. In the presence of strong magnetic fields, all of the hyperons are susceptible to spin polarization. As we discussed in Section 4.1, spin polarization counteracts the effects of Landau quantization, by stiffening the EOS. Although assuming the existence of hyperons gives a smaller maximum mass in the absence of a magnetic field ($\beta \to \infty$ in Figure 4.5), increasing the magnetic field strength (decreasing β), now increases the maximum mass. Assuming equal pressures of magnetic field and matter ($\beta = 1/3$), we get a maximum mass which is 26% larger than the one with no magnetic field ($\beta \to \infty$).

Figure 4.6 shows similar results, now incorporating the physics of the crust by using the SLy EOS calculated by Douchin & Haensel (2001) at densities below nuclear saturation density. In this case, the M-R relation found by assuming zero magnetic field strength ($\beta \to \infty$), is similar to the well-known GM3 EOS calculated by Glendenning & Moszkowski (1991). A similar increase in neutron star maximum mass with magnetic field strength is seen here.[1]

We are also interested in the effects of the anomalous magnetic moments of nucleons on the M-R relations. Figure 4.7 shows these results for the magnetized nuclear EOS with hyperons and crust physics included. As we see, the effect of including the anomalous magnetic moments is small. We expected this from applying the condition given by Eq. (4.2) on the magnetic EOS of Broderick et al. (2000, 2002) with anomalous moments. As can be seen in Figure 4.3, complete spin polarization of the anomalous moments (which

[1]For another recent study of the effects of strong magnetic fields on the population of hyperon stars, see Gomes et al. (2014).

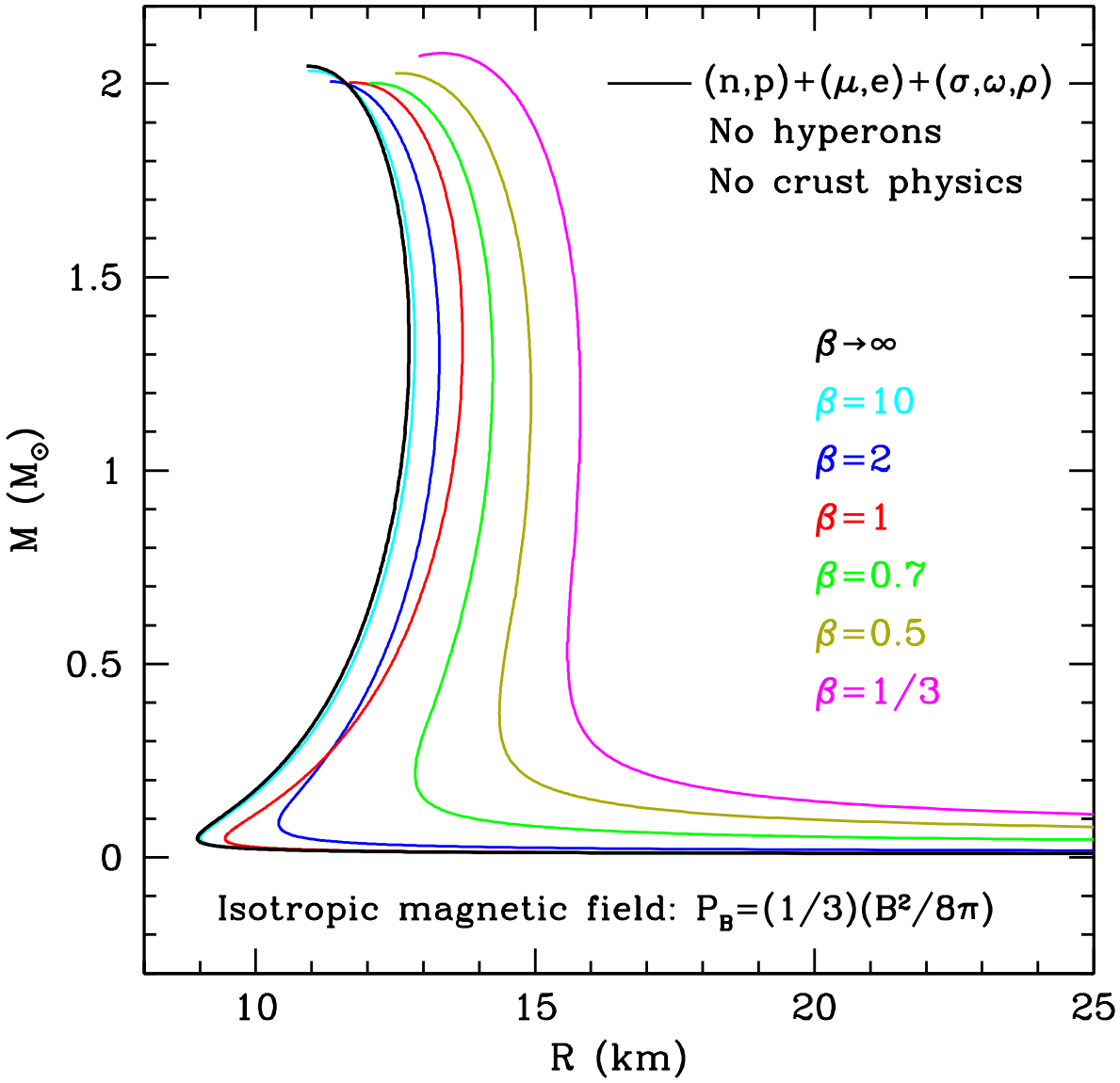

Figure 4.4: The M-R relation for the magnetized EOS (Broderick et al., 2000) with no crust physics included. Here, the magnetic field provides hydrostatic support for the star by entering globally in the Einstein equations as $P_B = (1/3)(B^2/8\pi)$. The calculation has been done for different values of β in Eq. (4.2). Smaller values of β are associated with higher values of magnetic field strength in the neutron star. $\beta = 1/3$ corresponds to a neutron star with equal pressure of magnetic field and matter.

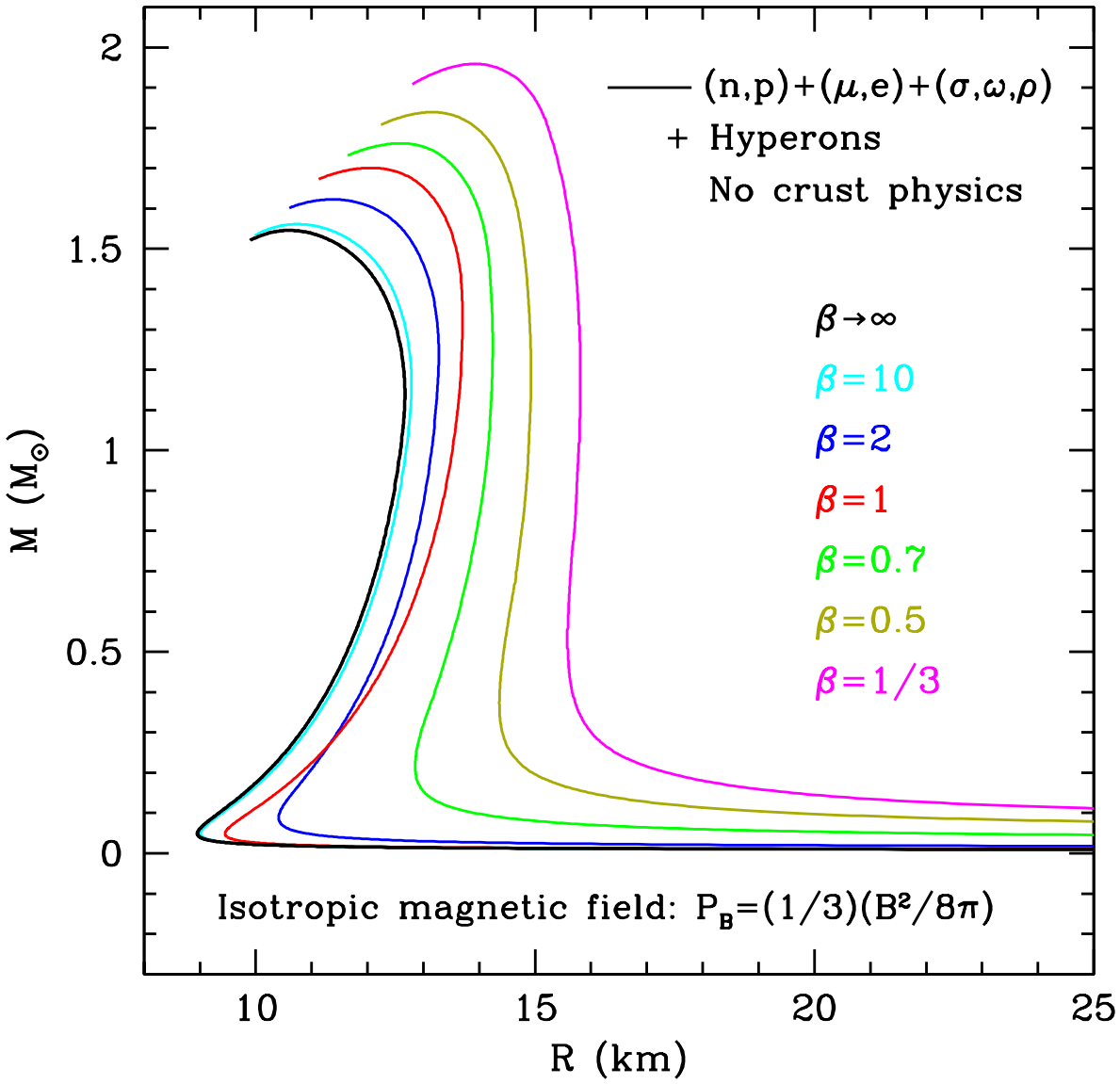

Figure 4.5: Same as Figure 4.4, but now including the effect of hyperons.

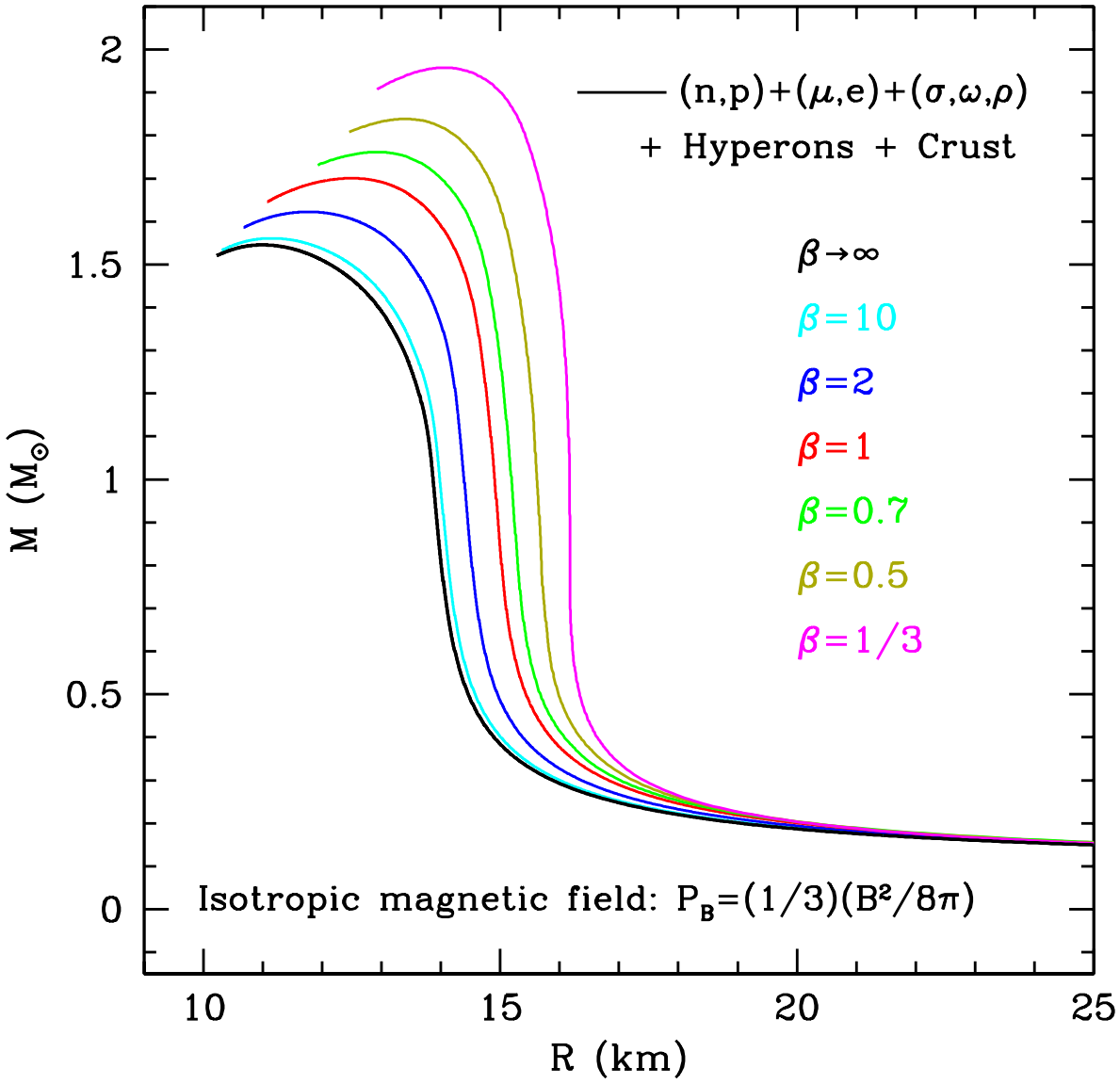

Figure 4.6: Same as Figure 4.5, but now also including the crust physics via the SLy EOS (Douchin & Haensel, 2001). The black curve, corresponding to negligible magnetic field strength, is equivalent to the GM3 EOS (Glendenning & Moszkowski, 1991).

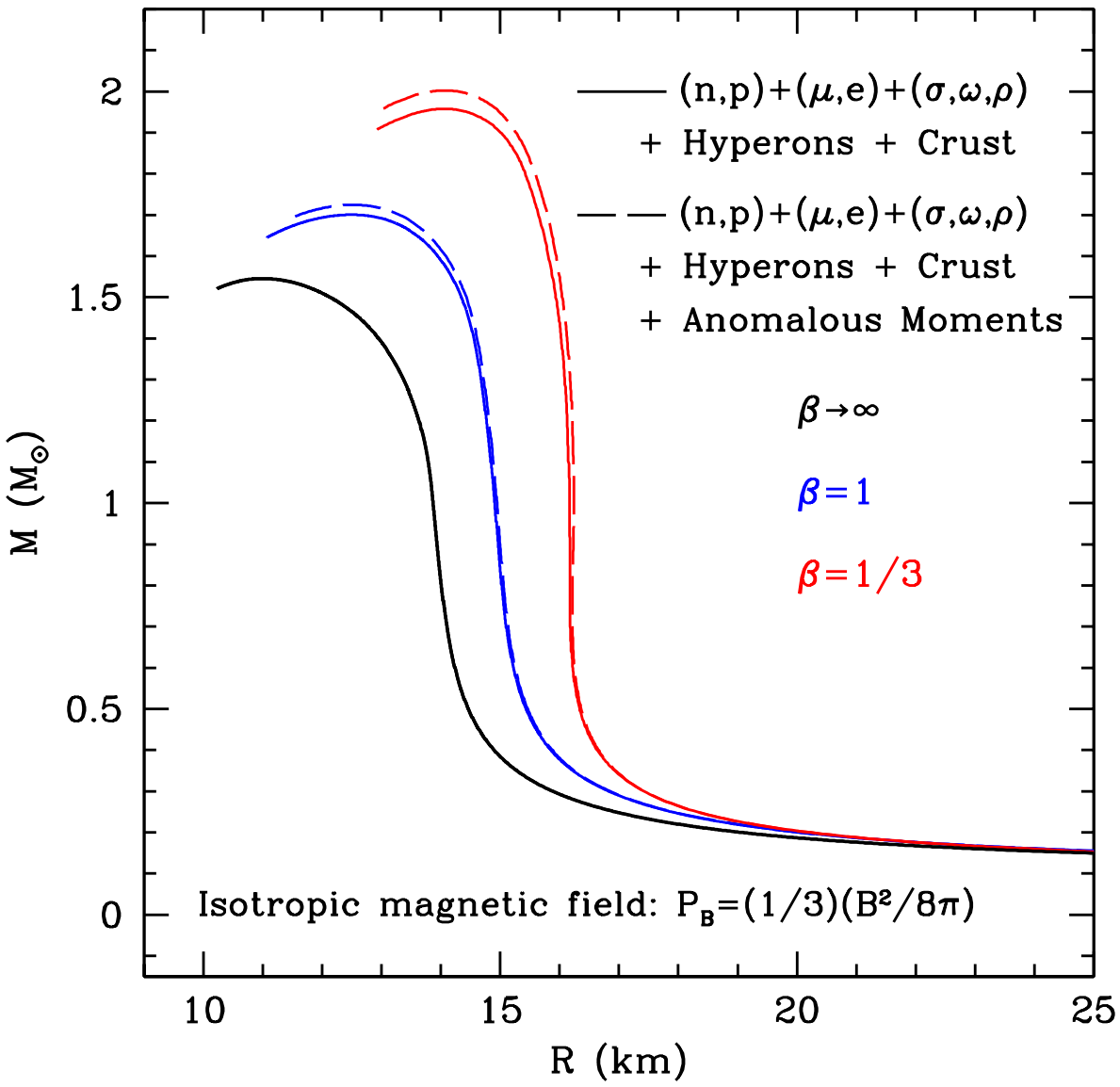

Figure 4.7: The M-R relation for the magnetized EOS with hyperons (Broderick et al., 2002) and the crust physics included via the SLy EOS (Douchin & Haensel, 2001). The solid curves have been calculated assuming no anomalous magnetic moments and the dashed curves have been calculated assuming the existence of anomalous moments.

is where we would expect their effects to be considerable) occurs at values of $\beta \sim 0.001$, in other words when the pressure of the magnetic field is 1000 times larger than pressure of matter, which are not expected to arise in dynamos, as discussed above. Therefore the strongest magnetic field strength we considered was one for which the magnetic pressure equals the pressure of matter ($\beta = 1/3$). The effect of including magnetic anomalous moments under this magnetic field strength is a 2% change in the neutron star maximum mass as seen in Figure 4.7.

Finally, to better illustrate the effect of the magnetic field strength on the maximum mass and radius of neutron stars, Figures 4.8 and 4.9 show the maximum mass and inflection point in radius (where the second derivative of mass versus radius changes sign) as a function of $1/\beta$, for the mass radius relationship shown in Figure 4.6. We specify the radius by the inflection point in the M-R relation, where mass is nearly independent of radius, giving a characteristic value across a wide range of neutron star masses. We see that these relative changes are well fit by

$$\frac{\Delta M_{\rm max}}{M_{\rm max}} \simeq 0.1\ \beta^{-1},\ \text{and}\ \frac{\Delta R_{\rm inf}}{R_{\rm inf}} \simeq 0.06\ \beta^{-0.94}, \tag{4.9}$$

for an *isotropic* tangled magnetic field distribution.

4.4 M-R relations with a force-free magnetic field

Despite the production of small-scale, turbulent fields by the dynamos initially, the final magnetic field configuration remains unclear. After the dynamos quench and before the formation of a crust that can balance shear stresses the neutron star will reconfigure the magnetic field geometry via bulk fluid motions on a timescale measured in Alfvén crossing times, resulting in a linked, nearly force-free geometry dictated by the initial magnetic helicity (Braithwaite & Spruit, 2004, 2006). This is a natural consequence of helicity conservation during reconnection, corresponding to the minimum energy state at fixed magnetic helicity (Broderick & Narayan, 2008), which is fully defined by

$$\nabla \times \mathbf{B} = \alpha \mathbf{B}\,, \tag{4.10}$$

from which it is clear that $\mathbf{j} \times \mathbf{B} = 0$ where $\mathbf{j}$ is the current density, i.e., the Lorentz force vanishes. In the above, α is a constant set by the boundary conditions at the stellar surface, setting a scale length for the resulting magnetic geometries.

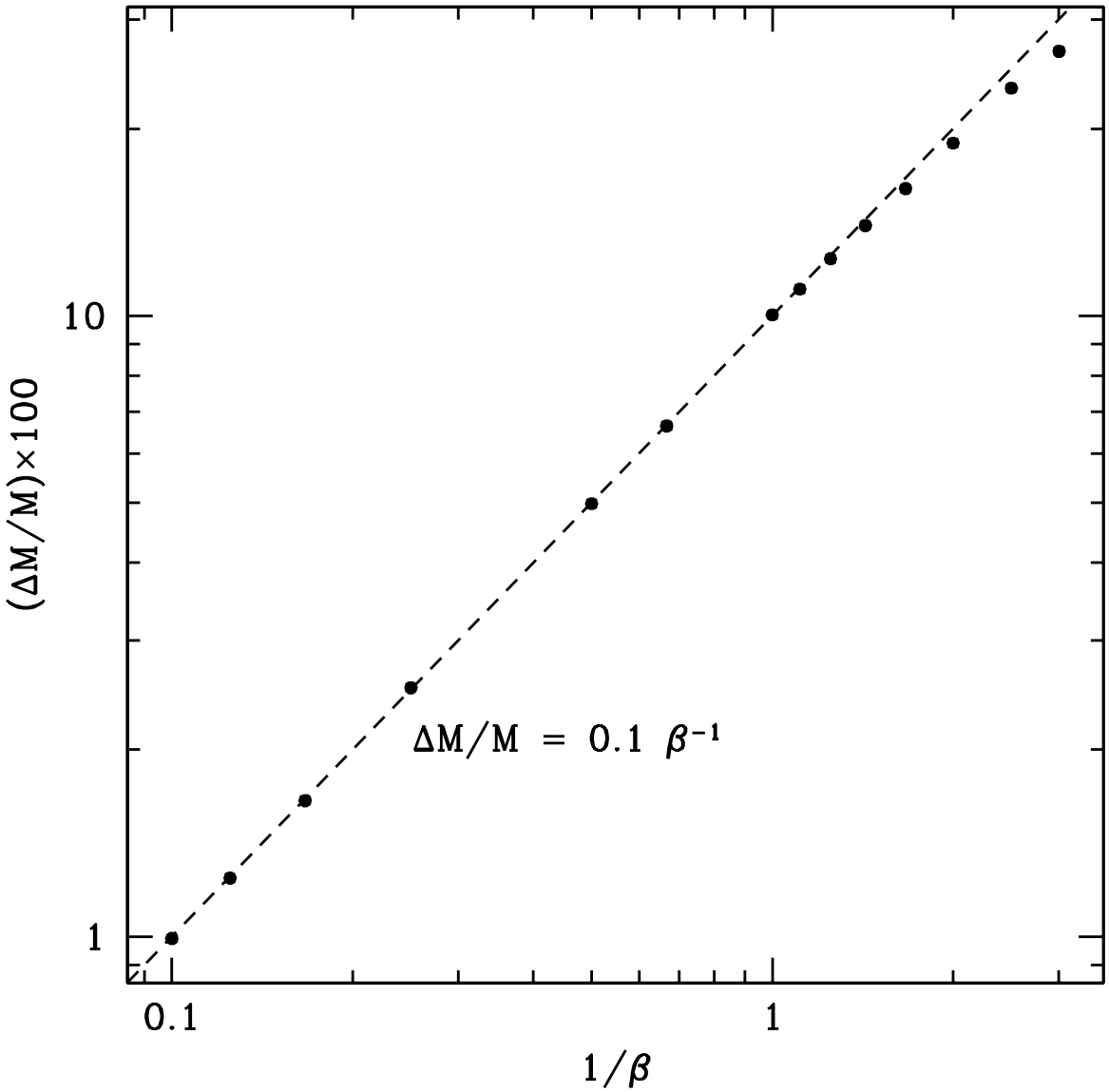

Figure 4.8: Change in maximum mass of neutron stars as a function of $1/\beta$ (see Eq. (4.2) for definition of β) for the mass-radius relation shown in Figure 4.6.

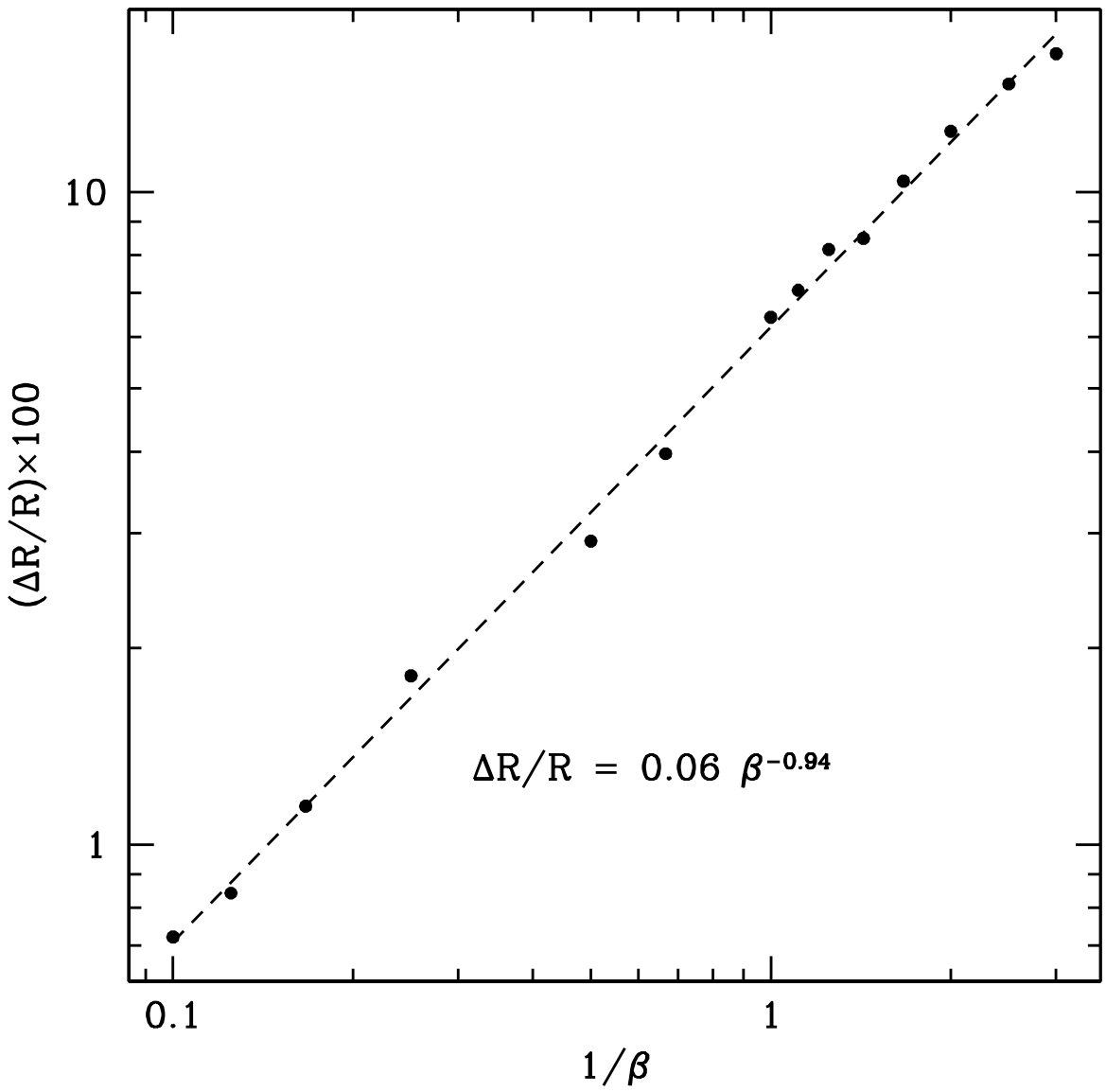

Figure 4.9: Change in radius of the deflection point in the M-R curve of neutron stars as a function of $1/\beta$ (see Eq. (4.2) for definition of β) for the mass-radius relation shown in Figure 4.6.

This gives axisymmetric and anisotropic configurations for the magnetic field. This configuration in the interior of the star, in terms of the vector spherical harmonics Y_l, Ψ_l and Φ_l is:

$$\mathbf{B} = \sum_l \left\{ -\left[\frac{l(l+1)}{r} d_l j_l(\alpha r)\right] \mathrm{Y}_l \; - \left[\frac{1}{r}\partial_r r d_l j_l(\alpha r)\right] \Psi_l + \alpha d_l j_l(\alpha r)\Phi_l \right\}, \tag{4.11}$$

where l is the spherical harmonic degree, j_l is the spherical Bessel function, and d_l is a constant giving the strength of each harmonic mode.

To assess the consequence of the force-free condition on the hydrostatic equilibrium of the star, we can start by looking at the Newtonian Euler equation and impose static conditions:

$$\rho \frac{d\mathbf{v}}{dt} = -\nabla P_g - \rho \nabla \Phi + \mathbf{j} \times \mathbf{B} = -\nabla P_g - \rho \nabla \Phi = 0, \tag{4.12}$$

where ρ is the density and Φ is the Newtonian potential given by the Possion equation:

$$\nabla^2 \Phi = 4\pi G \rho. \tag{4.13}$$

Therefore, we have:

$$\nabla P_g = -\rho \nabla \Phi, \tag{4.14}$$

which is the Newtonian equation for hydrostatic equilibrium with no effect of the magnetic field in it. This means that in Newtonian mechanics, the force-free condition implies that the magnetic field will play no global role in supporting the star, even though it might still change the nuclear equation of state via the effects mentioned above (e.g., Landau quantization, spin polarization, etc.).

In general relativity, the force-free condition can be written in its covariant form:

$$j_\nu F^{\mu\nu} = 0 \rightarrow F^{\mu\nu} \nabla_\alpha F^\alpha_\nu = 0, \tag{4.15}$$

where $F_{\mu\nu}$ is the electromagnetic tensor. The electromagnetic stress-energy tensor is given by

$$4\pi T_{EM}{}^\mu_\nu = F^{\mu\alpha} F_{\nu\alpha} - \frac{1}{4} \delta^\mu_\nu F^{\alpha\beta} F_{\alpha\beta}. \tag{4.16}$$

The full stress-energy tensor is given by:

$$T^{\mu\nu} = {T_{gas}}^{\mu\nu} + {T_{EM}}^{\mu\nu}, \tag{4.17}$$

from which the Euler equation is obtained by $\nabla_\nu T^{\mu\nu} = 0$. The contribution from ${T_{EM}}^{\mu\nu}$ is generally, after some manipulation and application of Maxwell's equations,

$$\nabla_\nu {T_{EM}}^{\mu\nu} = \frac{1}{4\pi} F^{\mu\alpha} \nabla_\nu F^\nu_\alpha = j_\nu F^{\mu\nu} = 0, \tag{4.18}$$

therefore as in the Newtonian limit the direct impact of the electromagnetic forces vanish, i.e., $\nabla_\nu T^{\mu\nu} = \nabla_\nu {T_{gas}}^{\mu\nu} = 0$.

Gravity is now described by the Einstein equation:

$$G^{\mu\nu} = 8\pi G\big({T_{gas}}^{\mu\nu} + {T_{EM}}^{\mu\nu}\big). \tag{4.19}$$

Unlike the Newtonian case, now the electromagnetic field can contribute by sourcing gravity. In practice, it is necessary to solve for the full magnetic field configuration and metric simultaneously. However, we might imagine that since gravity is a long-range force and the structure of the initially highly turbulent electromagnetic field should exhibit mostly small-scale structure that we may spatially average the electromagnetic configuration. That is to solve:

$$G^{\mu\nu} = 8\pi G\big({T_{gas}}^{\mu\nu} + \langle {T_{EM}}^{\mu\nu}\rangle\big), \tag{4.20}$$

where $\langle ...\rangle$ is a local spatial average, i.e., an average over scales large in comparison to the scale of the electromagnetic field fluctuations and small in comparison to the gravitational scales. The stress energy tensor for this average field is

$$\langle {T_{EM}}^{\mu\nu}\rangle = \begin{pmatrix} -\epsilon_B & & & \\ & P_B^{(r)} & & \\ & & P_B^{(\theta)} & \\ & & & P_B^{(\phi)} \end{pmatrix},$$

where

$$\begin{aligned} \epsilon_B &= \langle B^2\rangle/8\pi, \\ P_B^{(r)} &= \langle B^2\rangle/8\pi - \langle B^r B_r\rangle/4\pi, \\ P_B^{(\theta)} &= \langle B^2\rangle/8\pi - \langle B^\theta B_\theta\rangle/4\pi, \\ P_B^{(\phi)} &= \langle B^2\rangle/8\pi - \langle B^\phi B_\phi\rangle/4\pi. \end{aligned}$$

The anisotropy of this average configuration may be quantified via an anisotropy parameter,

$$\Delta \equiv \frac{[P_B^{(\theta)} + P_B^{(\phi)}]/2 - P_B^{(r)}}{\langle B^2\rangle/8\pi}. \tag{4.21}$$

An anisotropy parameter $\Delta = -1$ corresponds to a purely tangential magnetic field configuration $\big(\langle B^r\rangle = 0\big)$ and $\Delta = 2$ corresponds to a purely radial field $\big(\langle B^r\rangle = \langle B\rangle\big)$. An isotropic average field will have $\Delta = 0$.

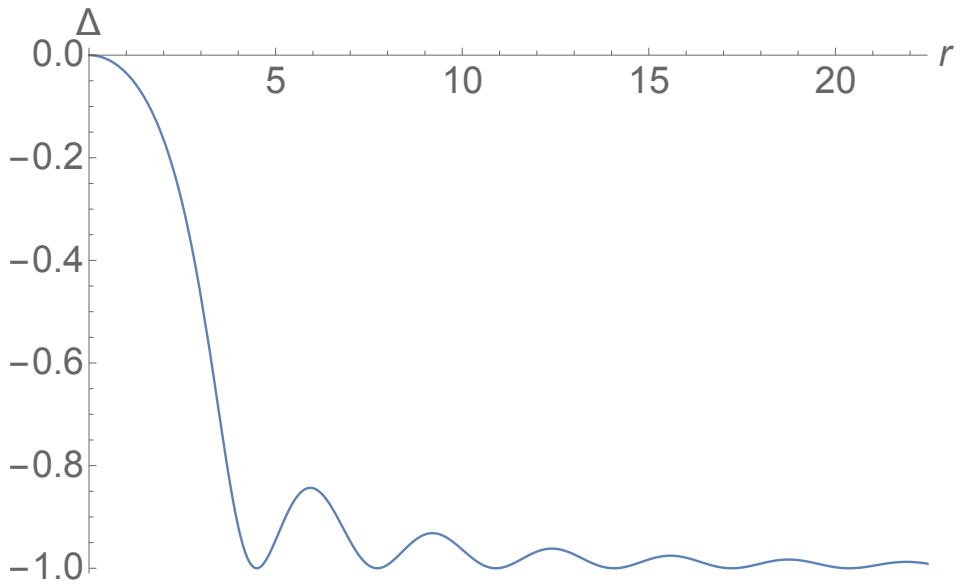

Figure 4.10: Anisotropy parameter for the average force-free configuration for the $l = 1$ spherical harmonic degree. Units of radius are set so that $\alpha = 1$ in Eq. (4.11).

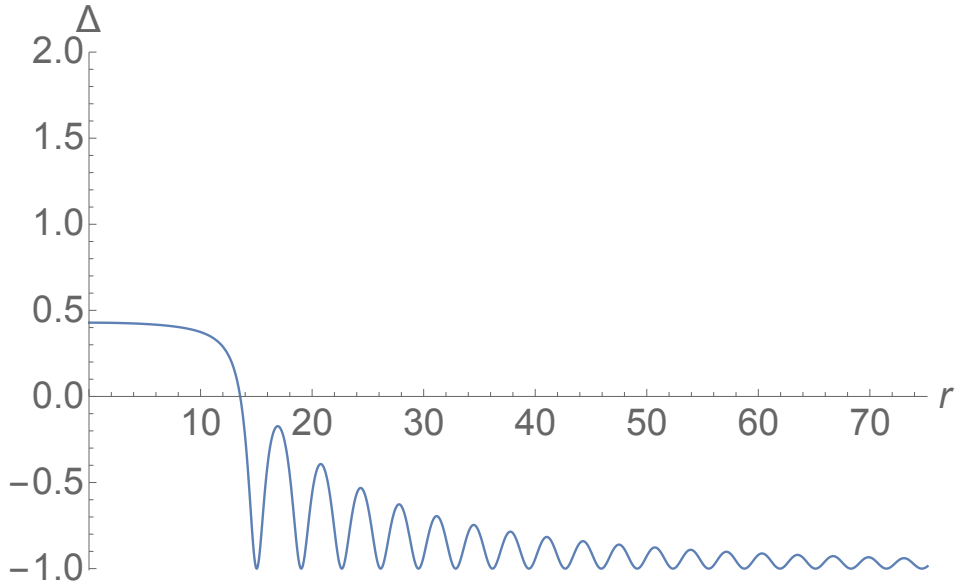

Figure 4.11: Anisotropy parameter for the average force-free configuration for the $l = 10$ spherical harmonic degree. Units of radius are set so that $\alpha = 1$ in Eq. (4.11).

Figures 4.10 and 4.11 show the anisotropy parameter calculated for the average force-free magnetic field configuration given by Eq. (4.11) for two spherical harmonic degrees of $l = 1$ and $l = 10$. At the centre of the star, there is a region with an isotropic average field ($\Delta = 0$) for $l = 1$ and as we go to higher spherical harmonic degrees $\Delta \to 0.5$ at the centre as can be seen in Figure 4.11. As we see in both Figures 4.10 and 4.11, Δ drops to -1 towards the outside of the star. This matches our expectation of field lines closing and the magnetic field becoming tangential in the outside. In the calculations below, we will refer to the radius of the isotropic core with $\Delta = 0$ as $R_\star$ (having chosen the anisotropy parameter of the first harmonic degree, as the magnetic field strength is dominated by the first harmonic degree at the centre).

To calculate the mass-radius relationship of the star, we will assume spherical symmetry and continue using an equipartition magnetic field (Eq. (4.2)). In order to write the hydrostatic equilibrium equations coming from general relativity for the force-free model, we use Eq. (4.18) (in other words the fact that the Euler equation is simply given by the energy momentum conservation of the gas). As an approximation, we will solve the Einstein equation given by Eq. (4.20). It is worth clarifying that solving Eq. (4.20) alongside the energy momentum conservation of the gas ($\nabla_\nu {T_{gas}}^{\mu\nu} = 0$), would formally require

$$\nabla_\mu \langle {T_{EM}}^{\mu\nu} \rangle = 0, \tag{4.22}$$

while by using the force-free condition Eq. (4.18) we are only assuming that

$$\nabla_\mu {T_{EM}}^{\mu\nu} = 0. \tag{4.23}$$

As we will show in the Appendix, solving Eq. (4.22) alongside with the Euler equation for the gas, would uniquely determine the anisotropy parameter. As spherical symmetry only allows isotropy ($\Delta = 0$) at the centre of the star, solving Eq. (4.22) will result in $\Delta \to 0$ throughout most of the star. This will change the final mass-radius relationship results we obtain from using the anisotropy parameter coming directly from the force-free configuration (satisfying Eq. (4.23)) at most by 9%. This anisotropy parameter based on the results shown in Figure 4.10 will have a core with $\Delta = 0$ of size $R_\star$ and in our approximation, Δ will drop to -1 at $R_\star$.

In dimensions where $G = 1$ and $c = 1$, the Euler equation coming from $\nabla_\nu {T_{gas}}^{\mu\nu} = 0$ is given by

$$\frac{dP_g}{dr} = -(\epsilon_g + P_g)\, g, \tag{4.24}$$

where g is

$$g \equiv \frac{M + 4\pi \left(P_g + P_B^{(r)}\right) r^3}{r^2(1 - 2M/r)}. \tag{4.25}$$

The enclosed mass is still given by Eq. (4.8), which still includes the magnetic contribution to the energy density.

Based on the definition of Δ and the assumption of spherical symmetry $\langle B^\theta B_\theta \rangle = \langle B^\phi B_\phi \rangle$, from which

$$P_B^{(r)} = \frac{1-2\Delta}{3} \langle B^2 \rangle / 8\pi. \tag{4.26}$$

Using this and the equipartition assumption the total radial pressure becomes

$$P_g + P_B^{(r)} = (1 + \frac{1-2\Delta}{3\beta}) P_g, \tag{4.27}$$

requiring only the specification of P_g and Δ. The pressure and energy density of the gas are related through the nuclear equation of state which is itself affected by the magnetic field. The resulting mass-radius relationships from this numerical integration are shown in Figure 4.12. The solid curves correspond to the force-free mass-radius calculation based on the magnetized EOS with hyperons (Broderick et al., 2002) and the crust physics included via the SLy EOS (Douchin & Haensel, 2001). This calculation has been done for two different values of β. The range in each curve is due to assuming a range in $R_\star$ (radius of the isotropic core with $\Delta = 0$) from 0 to 3 km. The previously found mass-radius relationships based on an isotropic magnetic field are also plotted for comparison (dashed curves).

In stark contrast to the case of tangled, isotropic magnetic fields, a force-free configuration produces a substantial *decrease* in the maximum neutron star mass. This is not surprising – force-free magnetic field geometries contribute to the energy density, and therefore gravity, but not to the supporting pressure. This conclusion is only weakly dependent on the details of the force-free configuration under consideration, showing little sensitivity to the size of our assumed isotropic core, $R_\star$. However, even for large values of β, e.g., $\beta = 1$, the magnitude of the effect is constrained to 20%, similar in size if not direction to that associated with the isotropic tangled geometry.

The dependence on magnetic field strength of the size of the effects on mass and radius are illustrated in Figures 4.13 and 4.14. Note that unlike Figures 4.8 and 4.9, the change in mass and radii are now negative. As before, the change in mass and radii are well fit by power laws over at least an order of magnitude in β, for maximum mass and inflection point radius

$$\frac{\Delta M_{\rm max}}{M_{\rm max}} \simeq -0.13\ \beta^{-0.9}, \text{ and } \frac{\Delta R_{\rm inf}}{R_{\rm inf}} \simeq -0.03\ \beta^{-0.94}, \tag{4.28}$$

assuming a *force-free* tangled magnetic field distribution.

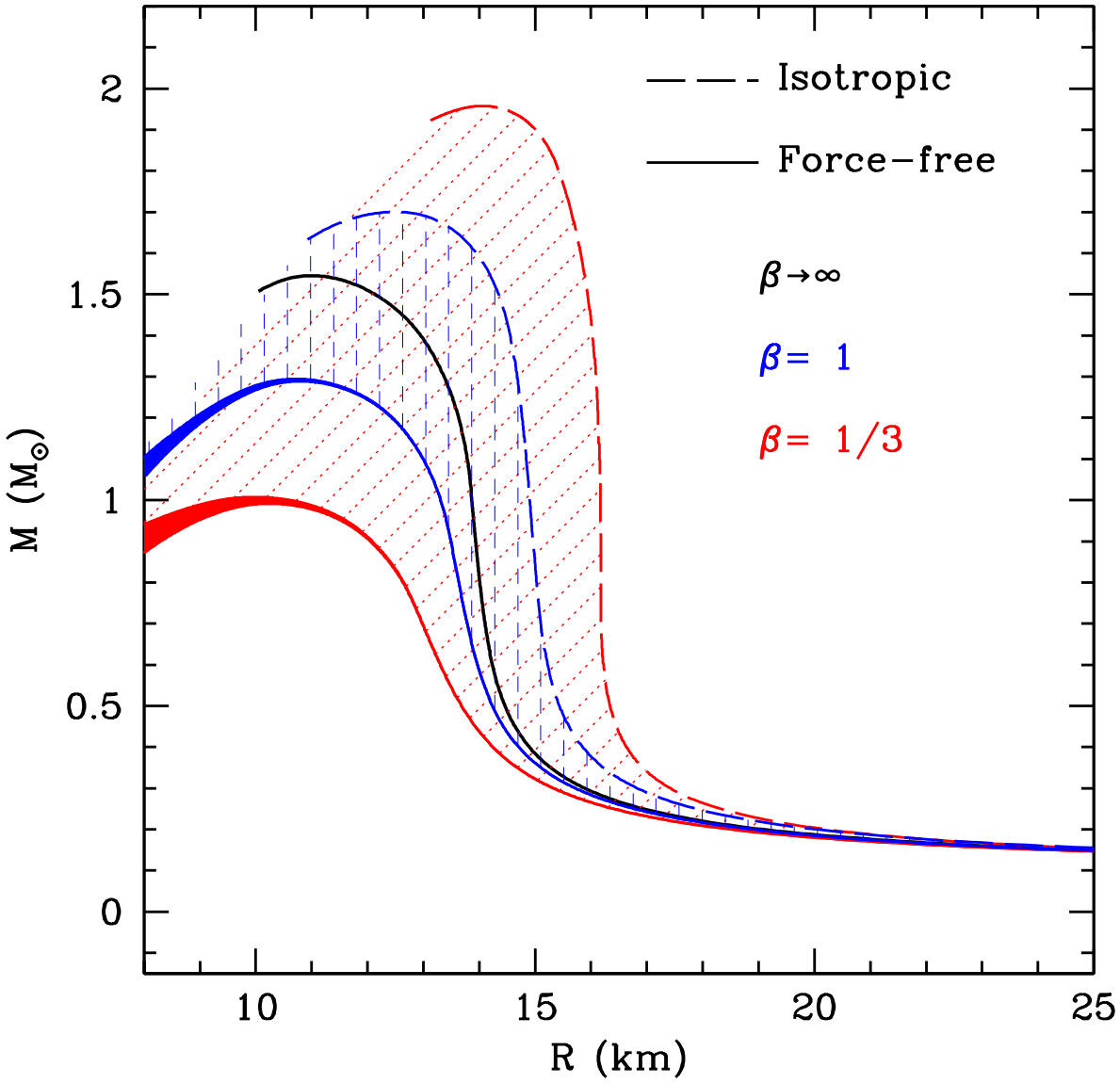

Figure 4.12: The M-R relations for the magnetized EOS with hyperons (Broderick et al., 2002) and the crust physics included via the SLy EOS (Douchin & Haensel, 2001). The dashed curves are for an isotropic magnetic field and the the solid curves correspond to the force-free model. Results are shown for two values of β. The range in the force-free (solid) curves is due to assuming a range in $R_\star$ (radius of the isotropic core with $\Delta = 0$) from 0 to 3 km.

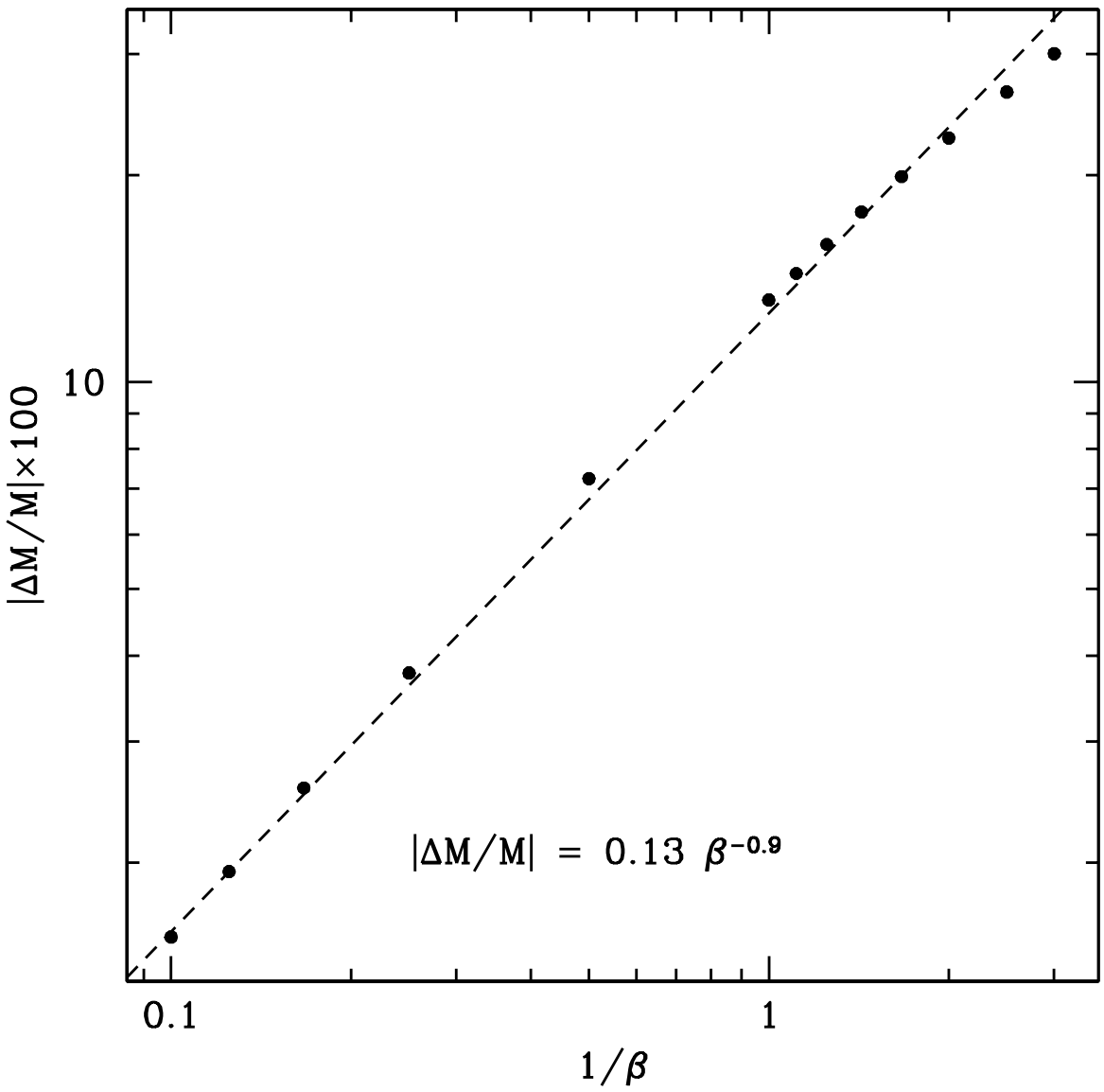

Figure 4.13: Change in maximum mass (absolute value for the logarithmic scale as the mass is decreasing) of neutron stars as a function of $1/\beta$ (see Eq. (4.2) for definition of β) for the force-free mass-radius relations shown in Figure 4.12.

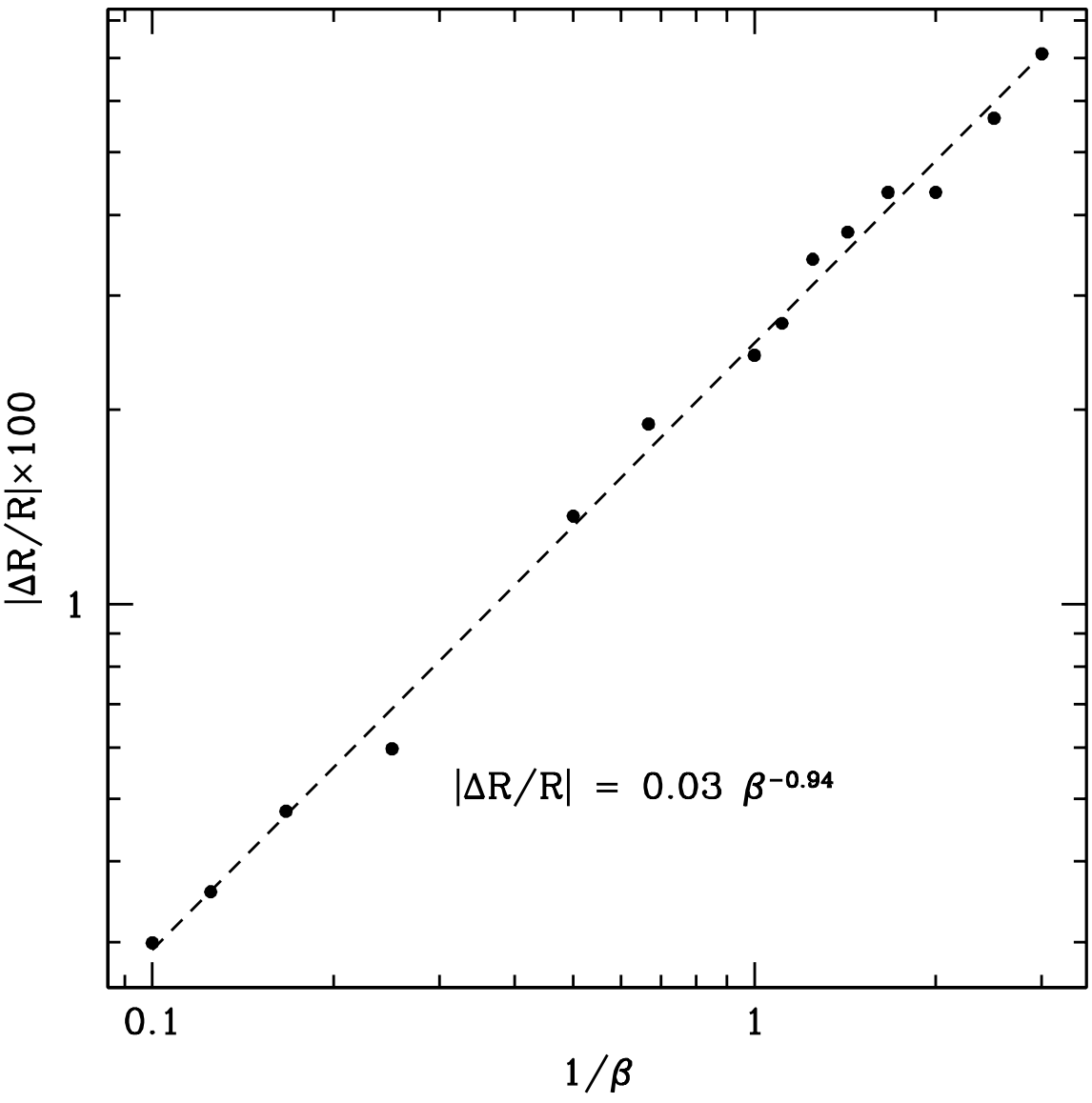

Figure 4.14: Change in radius of the deflection point in the M-R curve of neutron stars (absolute value for the logarithmic scale as the radius is decreasing) as a function of $1/\beta$ (see Eq. (4.2) for definition of β) for the force-free mass-radius relations shown in Figure 4.12.

4.5 Conclusions

In this chapter, we have demonstrated that the assumed geometry of interior neutron star magnetic fields is at least as important as the field strengths themselves when assessing the impact on masses and radii, capable of *qualitatively* modifying their effect. Highly tangled, isotropic magnetic configurations do result in an increase in the maximum mass, typical of results often found in the literature (e.g., see Astashenok et al., 2014a). However, force-free configurations, motivated by dynamical studies of magnetic field evolution in proto-neutron stars, produce a *decrease* in the maximum neutron star mass. For both configurations of the equipartition strength fields, the magnitude of the impact on the maximum mass is limited to 30%. The impact of anomalous magnetic moments for equipartition magnetic field strengths at best modify the maximum mass by 2%, suggesting that they are sub-dominant to the global magnetic field geometry.

This immediately challenges the assertion that magnetic fields provide a means to reconcile the recent observations of very massive neutron stars with unmagnetized equations of state whose maximum mass is otherwise precluded. In the absence of some credible mechanism for producing super-equipartition magnetic fields, the maximum deviation in the maximum mass of order 20%-30% means that at best these can impact only marginal cases. For example, this is unable to bring the GM3 EOS we employed into consistency with the existing 2 $M_\odot$ mass measurements. We expect this to be generic for models of neutron star formation in which the interior magnetic fields are produced by turbulent processes, providing an optimistic upper limit on the mass-limit enhancement achievable via the introduction of electromagnetic support. Of course, the existence of well-motivated magnetic field configurations in which the maximum neutron star mass actually decreases (i.e., force-free configurations) calls into question the value of invoking magnetic support altogether in order to increase maximum neutron star masses.

We note that the observed anomalous braking indices for the spin-down of pulsars can be interpreted as evidence for sub-surface toroidal magnetic fields of $10^{14} - 10^{15}$ G, *substantially* stronger than the observed dipole fields, which are slowly diffusing out of the crust due to transport processes (e.g., see Gourgouliatos & Cumming, 2015, and references therein). Even if taken at face value, it is unclear if these fields can reach the viral level of $\sim 10^{18}$ G in the core. However, as we have argued above, this is anticipated by simple astrophysical dynamo processes during the formation of the neutron star, followed by subsequent cooling in (quasi-)hydrostatic equilibrium.

An interesting possibility is that, depending on their initial conditions, different neutron stars might have dynamos of varying efficiency during their formation process. Therefore,

future observations of Mass-Radius relationship of neutron stars may exhibit an intrinsic scatter due to variations in internal magnetic field. An even more exciting possibility is finding a surface measure of this internal magnetic field (e.g., through modelling the braking indices), which could then correlate with (and thus effectively reduce) this scatter, following our simple scalings (Figs. 4.8-4.9,4.13-4.14). In particular, the sign of the correlation will be indicative of the (force-free v.s. isotropic) field configuration.

In typical MHD turbulence, and in lieu of an active dynamo, one expects the magnetic field to relax to a force-free configuration within an Alfvén crossing time, through subsequent reconnections that conserve helicity (Braithwaite & Spruit, 2006; Broderick & Narayan, 2008). Therefore, one may expect the force-free configuration to be preferred. However, if the interior of neutron stars transitions into type II superconductor, as hypothesized in the literature (e.g., see Haskell et al., 2013, and references therein), then it can support a frustrated network of flux tubes, which do *not* reconnect (Brandt, 1995). Such a configuration can support tangled (statistically) isotropic magnetic fields.

Finally, one may further speculate that reconnection is not completely halted, but is only significantly slowed (e.g., due to the presence of a mixture of type I and II superconducting phases in the interior). Therefore, the field configuration will slowly transition from isotropic to force-free, leading to a reduction in the maximum mass. Via this mechanism a subset of isolated neutron stars, those with masses between those that can be supported by force-free and tangled magnetic field configurations, could undergo a delayed collapse, surviving for a time scale set by the evolution of the internal magnetic geometry. Such an event may present an attractive alternate candidate for energetic, short-time scale phenomena, e.g., short gamma-ray bursts and the recently detected fast radio bursts.

Chapter 5

Epilogue

Most of this thesis was focused on how to use neutron stars as phenomenological laboratories for testing the validity of a modification of General Relativity, called "the gravitational aether theory". The theory was suggested by Afshordi (2008) as a solution to the old cosmological constant problem. As the theory makes predictions different from General Relativity in the presence of relativistic pressure (for previous phenomenological analysis of the aether theory for black holes and cosmology see Prescod-Weinstein et al., 2009; Aslanbeigi et al., 2011; Narimani et al., 2014), neutron stars will have a different hydrostatic structure and dynamical evolution in the aether theory. We calculated the mass-radius relationship of hydrostatic (non-rotating) neutron stars in the aether theory, assuming two equations of state of nuclear matter. For one of these equations of state, the mass-radius relationships given by General Relativity and the aether theory were both compatible with the Demorest et al. (2010) binary pulsar mass measurement, with the aether theory predicting a maximum mass 16% lower than the one given by General Relativity. It is interesting to compare this result with a similar calculation performed for the Einstein-Aether theory (another Lorentz-violating theory in which a dynamical unit time-like vector field is coupled to gravity) by Eling et al. (2007), that showed maximum masses 6-15% smaller than in General Relativity.

While the aether theory makes different predictions compared to General Relativity for static neutron stars, the degeneracy due to various nuclear equations of state, prevents us from making definitive claims about the validity of the aether theory. To break this degeneracy, we need either more progress in constraining the equation of state of matter beyond nuclear saturation density, or we need more observable constraints such as the ones from neutron star radius measurements or potentially from future gravitational wave measurements. Another interesting path to learning about distinct features of the aether,

is the study of the theory in dynamical situations, namely the time evolution of a neutron star.

This was the next step in our studies. We first succeeded at defining a Cauchy problem and obtaining a system of dynamical equations for the aether theory. Then, we studied the dynamics of a neutron star in the gravitational aether, starting with near hydrostatic initial configurations (with small radial velocities). We found that our equations had a well-posed (expanding) mode and a not well-posed (collapsing) mode, which confirmed similar results found by Aslanbeigi et al. (2011) in the context of cosmological perturbation theory for the aether theory. The results of numerically integrating our equations in the well-posed (expanding) mode, show that the system evolves toward the not well-posed (collapsing) mode. These results pose a challenge to our attempt to formulate an initial value problem for the aether theory. Whether alternative formulations are feasible remains an open question of vital importance for the viability of the theory.

The last chapter of this thesis was concerned with the effects of the assumed geometry of interior neutron star magnetic fields on the masses and radii of neutron stars. Most studies in the literature are focused on the effects of the field strengths, and the question of the field configurations often is ignored. We showed that highly tangled, isotropic magnetic configurations result in an increase in the maximum mass, typical of results often found in the literature (e.g., see Astashenok et al., 2014a), while force-free configurations, motivated by dynamical studies of magnetic field evolution in proto-neutron stars, produce a *decrease* in the maximum neutron star mass (changes up to 30% for both configurations). This challenges the commonly held belief that magnetic fields can save some nuclear equations of state by increasing their predicted maximum masses for neutron stars and making them compatible with recent mass measurements.

To summarize the premise of this thesis, in addition to illustrating the richness of the physical phenomena involved in neutron stars (an interplay of all the fundamental forces: electro-magnetism, strong and weak nuclear forces and gravitation), we showed how the study of neutron stars can shed light, not only on nuclear physics, but also on the nature of gravitation. It can do so, either by acting as a means of testing gravitational physics against observational data (e.g. comparing mass-radius relationships to measured masses), or by providing a theoretical framework (e.g. dynamical evolution of a neutron star) for the study of certain features of the gravitational models. By shedding light on the nature of gravity in extreme conditions, the study of neutron stars can play an important role in the quest for solutions to fundamental challenges of physics such as the cosmological constant problem.

Appendices

A Self-consistent anisotropy

As mentioned in Section 4.4, solving the average Einstein equation (4.20):

$$G^{\mu\nu} = 8\pi G\big({T_{gas}}^{\mu\nu} + \langle {T_{EM}}^{\mu\nu}\rangle\big), \tag{5.1}$$

along with the energy momentum conservation of the gas:

$$\nabla_\nu {T_{gas}}^{\mu\nu} = 0, \tag{5.2}$$

requires:

$$\nabla_\mu \langle {T_{EM}}^{\mu\nu}\rangle = 0. \tag{5.3}$$

This equation results in the anisotropic TOV equation for the average magnetic field:

$$\frac{dP_B^{(r)}}{dr} = -(\epsilon_B + P_B^{(r)})\ g + \frac{2\ \Delta\ \langle B^2\rangle/8\pi}{r}, \tag{5.4}$$

where g is given by Eq. (4.25). As $P_B^{(r)}$ is given by Eq. (4.26), and assuming Eq. (4.2), we will have:

$$\frac{d}{dr}\Big[\frac{P_g}{\beta}(\frac{1-2\Delta}{3})\Big] = -\Big[\frac{P_g}{\beta} + \frac{P_g}{\beta}(\frac{1-2\Delta}{3})\Big]\ g + \frac{2\Delta P_g}{\beta r} \tag{5.5}$$

$$\frac{1-2\Delta}{3\beta}\ \frac{dP_g}{dr} - \frac{2}{3}\frac{P_g}{\beta}\frac{d\Delta}{dr} = 2P_r\frac{\Delta-2}{3\beta}\ g + \frac{2\Delta P_g}{\beta r}, \tag{5.6}$$

and substituting for dP_g/dr from Eq. (4.24), and solving for $d\Delta/dr$, we get:

$$\frac{d\Delta}{dr} = \Big[\frac{3}{2} + (\Delta - \frac{1}{2})\frac{\epsilon_g}{P_g}\Big]\ g - \frac{3\Delta}{r}, \tag{5.7}$$

which simplifies to:

$$r^3\Delta = \int_0^r \left[\frac{3}{2} + (\Delta - \frac{1}{2})\frac{\epsilon_g}{P_g}\right] \, g \, r^3 dr. \tag{5.8}$$

The suitable boundary condition for Δ is determined by the fact that in the anisotropic TOV equation for the magnetic field (5.4), the second term on the right side is well defined only if $\Delta \to 0$ when $r \to 0$. Eq. (5.8) solved along with the TOV equation for the gas, uniquely determines $\Delta(r)$. As we see in Figure 5.1, Δ remains very close to zero (isotropic field) and more than -1 until the edge of the star where it drops to lower values. This behaviour of Δ makes at most a 9% change (in case of $\beta = 1/3$ and smaller changes for larger values of β) to the mass radius relationships previously found as can be seen in Figure 5.2. It is important to note that values of $\Delta < -1$ are unphysical, implying imaginary magnetic field strengths. This raises some concern regarding the self-consistent solution near the stellar surface; for the case shown in Figure 5.1, roughly 20% of the mass is located in this unphysical regime, implying that the mass estimates from the self-consistent solutions are marginal over-estimates.

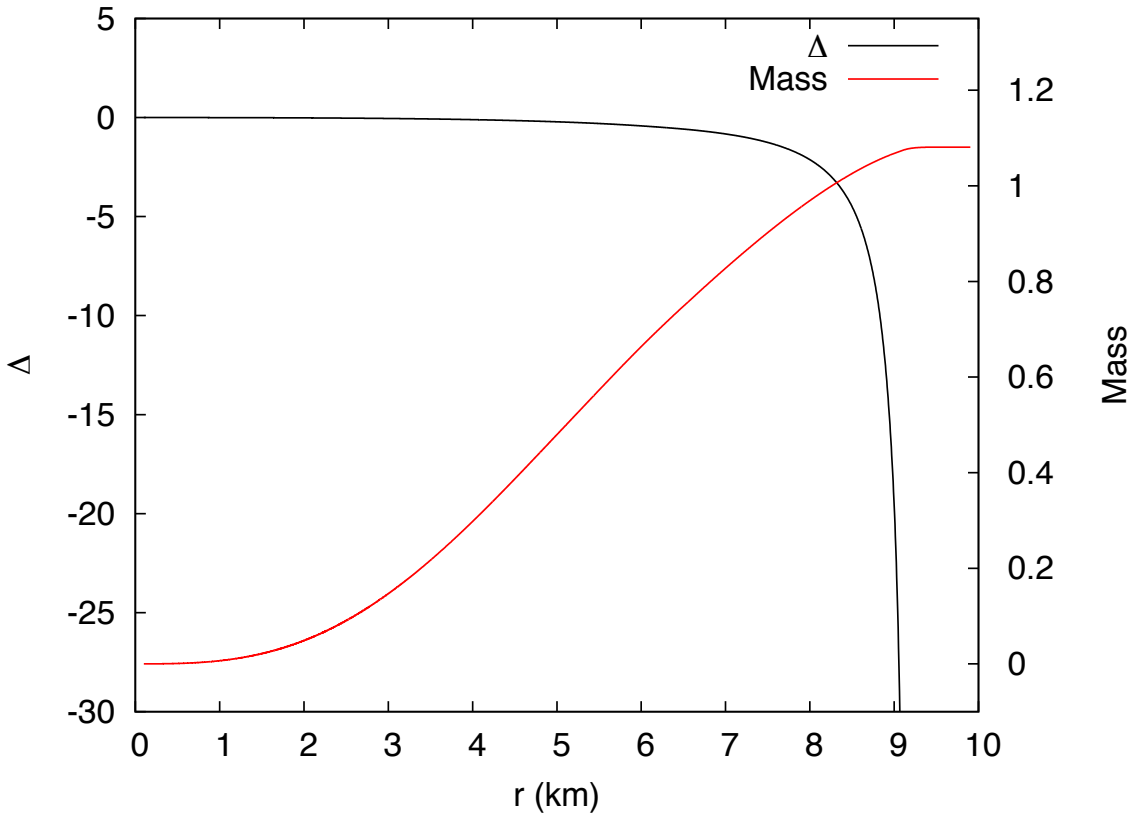

Figure 5.1: $\Delta(r)$ for a neutron star of radius $R = 10$ km with $\beta = 1/3$. Δ remains very close to zero (isotropic field) and more than -1 until the edge of the star where it drops to lower values.

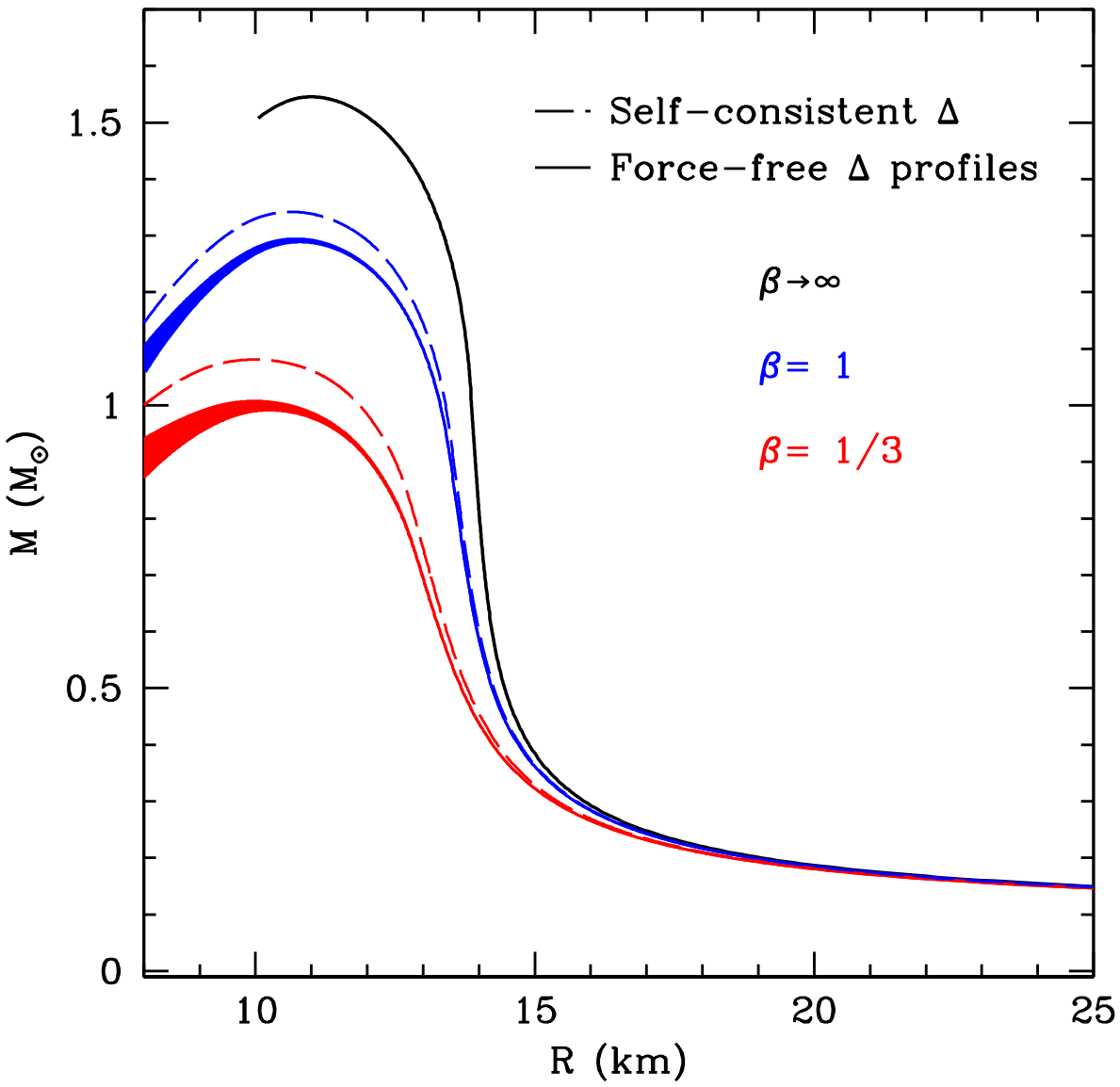

Figure 5.2: Solid curves are the force-free mass-radius relationships already shown in Figure 4.12. The dashed curves are the results found for the self-consistent anisotropy calculation presented in the Appendix.

References

Afshordi, N. 2008, arXiv:0807.2639 11, 12, 14, 36, 37, 113

Aharony, O., Gubser, S. S., Maldacena, J., Ooguri, H., & Oz, Y. 2000, Phys. Rep., 323, 183 9

Akmal, A., & Pandharipande, V. R. 1997, Phys. Rev. C, 56, 2261 21

Alavirad, H., & Weller, J. M. 2013, Phys. Rev. D, 88, 124034 17

Alcubierre, M. 2008, Introduction to 3+1 Numerical Relativity (Oxford University Press) 52, 53, 81

Alcubierre, M., & González, J. A. 2005, Computer physics communications, 167, 76 78, 79

Alford, M., Braby, M., Paris, M., & Reddy, S. 2005, ApJ, 629, 969 34

Anderson, M., Hirschmann, E. W., Lehner, L., et al. 2008, Physical Review Letters, 100, 191101 16

Antoniadis, J., Freire, P. C. C., Wex, N., et al. 2013, Science, 340, 448 8, 17

Ashtekar, A., & Lewandowski, J. 2004, Classical and Quantum Gravity, 21, 53 9

Aslanbeigi, S., Robbers, G., Foster, B. Z., Kohri, K., & Afshordi, N. 2011, Phys. Rev. D, 84, 103522 13, 14, 86, 113, 114

Astashenok, A. V., Capozziello, S., & Odintsov, S. D. 2013, J. Cosmology Astropart. Phys., 12, 40 14

—. 2014a, ArXiv e-prints, arXiv:1405.6663 18, 111, 114

—. 2014b, Phys. Rev. D, 89, 103509 15

Babichev, E., & Langlois, D. 2010, Phys. Rev. D, 81, 124051 14

Balberg, S., & Gal, A. 1997, Nuclear Physics A, 625, 435 34

Barausse, E., Palenzuela, C., Ponce, M., & Lehner, L. 2013, Phys. Rev. D, 87, 081506 15

Baumgarte, T. W., & Shapiro, S. L. 2010, Numerical Relativity: Solving Einstein's Equations on the Computer 48

Bekenstein, J. D. 2004, Phys. Rev. D, 70, 083509 14

Berti, E., Barausse, E., Cardoso, V., et al. 2015, ArXiv e-prints, arXiv:1501.07274 8, 10, 15

Boisseau, B., Esposito-Farèse, G., Polarski, D., & Starobinsky, A. A. 2000, Physical Review Letters, 85, 2236 9

Braithwaite, J., & Spruit, H. C. 2004, Nature, 431, 819 100

—. 2006, A&A, 450, 1097 100, 112

Brandt, E. H. 1995, Reports on Progress in Physics, 58, 1465 112

Broderick, A., Prakash, M., & Lattimer, J. M. 2000, ApJ, 537, 351 18, 88, 92, 94, 95, 96

Broderick, A. E., & Narayan, R. 2008, MNRAS, 383, 943 18, 19, 88, 94, 100, 112

Broderick, A. E., Prakash, M., & Lattimer, J. M. 2002, Physics Letters B, 531, 167 18, 88, 91, 94, 95, 99, 107, 108

Caldwell, R. R., Dave, R., & Steinhardt, P. J. 1998, Physical Review Letters, 80, 1582 9

Capozziello, S., De Laurentis, M., Farinelli, R., & Odintsov, S. D. 2015, ArXiv e-prints, arXiv:1509.04163 15

Capozziello, S., Harko, T., Koivisto, T. S., Lobo, F. S. N., & Olmo, G. J. 2013, J. Cosmology Astropart. Phys., 4, 11 9

Cardall, C. Y., Prakash, M., & Lattimer, J. M. 2001, ApJ, 554, 322 18

Carroll, S. M. 2001, Living Reviews in Relativity, 4, 1 11

Carroll, S. M., Duvvuri, V., Trodden, M., & Turner, M. S. 2004, Phys. Rev. D, 70, 043528 9

Cheoun, M.-K., Deliduman, C., Güngör, C., et al. 2013, J. Cosmology Astropart. Phys., 10, 21 14

Chevalier, R. A. 2005, ApJ, 619, 839

Choptuik, M. W., Lehner, L., & Pretorius, F. 2015, ArXiv e-prints, arXiv:1502.06853 15

Chow, N., & Khoury, J. 2009, Phys. Rev. D, 80, 024037 10

Cisterna, A., Delsate, T., & Rinaldi, M. 2015, Phys. Rev. D, 92, 044050 15

Cooney, A., Dedeo, S., & Psaltis, D. 2010, Phys. Rev. D, 82, 064033 10, 14, 27

Cyburt, R. H., Fields, B. D., & Olive, K. A. 2008, J. Cosmology Astropart. Phys., 11, 12 13

de Rham, C. 2014, Living Reviews in Relativity, 17, 7 10

Demorest, P. B., Pennucci, T., Ransom, S. M., Roberts, M. S. E., & Hessels, J. W. T. 2010, Nature, 467, 1081 xii, 4, 5, 6, 7, 17, 20, 29, 31, 32, 34, 113

DeWitt, B. S. 1967, Phys. Rev., 160, 1113

Dormand, J. R., & Prince, P. J. 1980, Journal of computational and applied mathematics, 6, 19 80

Douchin, F., & Haensel, P. 2001, A&A, 380, 151 21, 29, 30, 94, 95, 98, 99, 107, 108

Duncan, R. C., & Thompson, C. 1992, ApJ, 392, L9 15, 16, 91

Dunkley, J., Hlozek, R., Sievers, J., et al. 2011, ApJ, 739, 52

Eling, C., Jacobson, T., & Miller, M. C. 2007, Phys. Rev. D, 76, 042003 14, 113

Etienne, Z. B., Liu, Y. T., Paschalidis, V., & Shapiro, S. L. 2012, Phys. Rev. D, 85, 064029

Ferreira, P. G., & Joyce, M. 1997, Physical Review Letters, 79, 4740 9

Fialkovsky, I. V., Marachevsky, V. N., & Vassilevich, D. V. 2011, Phys. Rev. B, 84, 035446 10

Freire, P. C. C., Bassa, C. G., Wex, N., et al. 2011, MNRAS, 412, 2763 7

Friedman, B., & Pandharipande, V. R. 1981, Nuclear Physics A, 361, 502 21

Ganguly, A., Gannouji, R., Goswami, R., & Ray, S. 2014, Phys. Rev. D, 89, 064019 15

Garnavich, P. M., Jha, S., Challis, P., et al. 1998, ApJ, 509, 74 9

Gelb, A., & Tadmor, E. 1999, Applied and computational harmonic analysis, 7, 101 83

Glendenning, N. K. 1985, ApJ, 293, 470 34

Glendenning, N. K., & Moszkowski, S. A. 1991, Physical Review Letters, 67, 2414 91, 95, 98

Glendenning, N. K., & Schaffner-Bielich, J. 1999, Phys. Rev. C, 60, 025803 34

Gleyzes, J., Langlois, D., Piazza, F., & Vernizzi, F. 2015, J. Cosmology Astropart. Phys., 2, 18 10

Gomes, R. O., Dexheimer, V., & Vasconcellos, C. A. Z. 2014, ArXiv e-prints, arXiv:1407.0271 95

Gotthelf, E. V., Mori, K., Halpern, J. P., et al. 2013, The Astronomer's Telegram, 5046, 1 15

Gottlieb, D., Shu, C.-W., Solomonoff, A., & Vandeven, H. 1992, Journal of Computational and Applied Mathematics, 43, 81 83

Gourgouliatos, K. N., & Cumming, A. 2015, MNRAS, 446, 1121 111

Grandclément, P., & Novak, J. 2009, Living Rev. Relativity, 12 83

Guilet, J., & Müller, E. 2015, MNRAS, 450, 2153 16

Gundlach, C., Martín-García, J. M., & Garfinkle, D. 2013, Classical and Quantum Gravity, 30, 145003 82, 86

Harko, T., Koivisto, T. S., Lobo, F. S. N., & Olmo, G. J. 2012, Phys. Rev. D, 85, 084016 9

Harten, A., & Osher, S. 1987, SIAM Journal on Numerical Analysis, 24, 279 82

Haskell, B., Pizzochero, P. M., & Seveso, S. 2013, ApJ, 764, L25 112

Horndeski, G. W. 1974, International Journal of Theoretical Physics, 10, 363 10

Igumenshchev, I. V., & Narayan, R. 2002, ApJ, 566, 137 17

Israeli, M., & Orszag, S. A. 1981, Journal of Computational Physics, 41, 115 53

Jacoby, B. A., Hotan, A., Bailes, M., Ord, S., & Kulkarni, S. R. 2005, ApJ, 629, L113 7

Jaffe, R. L. 2005, Phys. Rev. D, 72, 021301 10

Kamiab, F., & Afshordi, N. 2011, Phys. Rev. D, 84, 063011 17, 37, 54, 57

Kamiab, F., Broderick, A. E., & Afshordi, N. 2015, arXiv:1503.03898

Kobayashi, T., & Maeda, K.-I. 2008, Phys. Rev. D, 78, 064019 14

Lahteenmaki, P., Paraoanu, G. S., Hassel, J., & Hakonen, P. J. 2013, Proceedings of the National Academy of Science, 110, 4234 10

Lasky, P. D., Sotani, H., & Giannios, D. 2008, Phys. Rev. D, 78, 104019 14

Lattimer, J. M., & Prakash, M. 2001, ApJ, 550, 426 17, 29, 34

—. 2007, Phys. Rep., 442, 109 3, 7, 17, 20, 34, 35

Levin, L., Bailes, M., Bates, S., et al. 2010, ApJ, 721, L33 16

Liu, X.-D., Osher, S., & Chan, T. 1994, Journal of computational physics, 115, 200 82

Lopes, L. L., & Menezes, D. P. 2014, ArXiv e-prints, arXiv:1411.7209 18

Lorenz, C. P., Ravenhall, D. G., & Pethick, C. J. 1993, Physical Review Letters, 70, 379 21

Maldacena, J. 1999, International Journal of Theoretical Physics, 38, 1113 9

Martí, J. M., Ibáñez, J. M., & Miralles, J. A. 1991, Phys. Rev. D, 43, 3794 48

Martin, J. 2012, Comptes Rendus Physique, 13, 566 11

Masada, Y., Takiwaki, T., & Kotake, K. 2015, ApJ, 798, L22 16

Melatos, A. 1999, ApJ, 519, L77 15

Momeni, D., Gholizade, H., Raza, M., & Myrzakulov, R. 2015, International Journal of Modern Physics A, 30, 50093 15

Momeni, D., & Myrzakulov, R. 2015, International Journal of Geometric Methods in Modern Physics, 12, 50014 15

Müller, H., & Serot, B. D. 1996, Nuclear Physics A, 606, 508 34

Narimani, A., Afshordi, N., & Scott, D. 2014, J. Cosmology Astropart. Phys., 8, 49 13, 113

Naso, L., Rezzolla, L., Bonanno, A., & Paternò, L. 2008, A&A, 479, 167 16, 91

Neilsen, D., Liebling, S. L., Anderson, M., et al. 2014, Phys. Rev. D, 89, 104029

Nobbenhuis, S. 2006, Foundations of Physics, 36, 613 11

Obergaulinger, M., Aloy, M. A., & Müller, E. 2010, A&A, 515, A30 16

Obergaulinger, M., Cerdá-Durán, P., Müller, E., & Aloy, M. A. 2009, A&A, 498, 241 16

Obergaulinger, M., Janka, H.-T., & Aloy, M. A. 2014, MNRAS, 445, 3169

Olausen, S. A., & Kaspi, V. M. 2014, ApJS, 212, 6 16

Orellana, M., García, F., Teppa Pannia, F. A., & Romero, G. E. 2013, General Relativity and Gravitation, 45, 771 14

Özel, F., & Psaltis, D. 2009, Phys. Rev. D, 80, 103003 xi, 21, 27, 29, 30

Özel, F., Psaltis, D., Ransom, S., Demorest, P., & Alford, M. 2010, ApJ, 724, L199 5, 20

Paczynski, B. 1992, Acta Astron., 42, 145 15

Pandharipande, V. R., & Smith, R. A. 1975, in Bulletin of the American Astronomical Society, Vol. 7, Bulletin of the American Astronomical Society, 240 34

Pani, P., Berti, E., Cardoso, V., & Read, J. 2011a, Phys. Rev. D, 84, 104035 15

—. 2011b, Phys. Rev. D, 84, 104035 17

Pannarale, F., Rezzolla, L., Ohme, F., & Read, J. S. 2011, Phys. Rev. D, 84, 104017 35

Parfrey, K., Beloborodov, A. M., & Hui, L. 2012, Monthly Notices of the Royal Astronomical Society, 423, 1416 83

Penna, R. F., Sądowski, A., Kulkarni, A. K., & Narayan, R. 2013, MNRAS, 428, 2255 17

Perlmutter, S., Aldering, G., Goldhaber, G., et al. 1999, ApJ, 517, 565 9

Prakash, M., Cooke, J. R., & Lattimer, J. M. 1995, Phys. Rev. D, 52, 661 34

Prescod-Weinstein, C., Afshordi, N., & Balogh, M. L. 2009, Phys. Rev. D, 80, 043513 12, 24, 113

Press, W. H., Flannery, B. P., Teukolsky, S. A., & Vetterling, W. T. 1989, Numerical recipes in C. The art of scientific computing (Cambridge University Press) 78, 80, 82, 84

Price, D. J., & Rosswog, S. 2006, Science, 312, 719 16, 17, 91

Ratra, B., & Peebles, P. J. E. 1988, Phys. Rev. D, 37, 3406 9

Read, J. S., Markakis, C., Shibata, M., et al. 2009, Phys. Rev. D, 79, 124033 21, 35

Rees, M. J., & Gunn, J. E. 1974, MNRAS, 167, 1

Rhoades, C. E., & Ruffini, R. 1974, Physical Review Letters, 32, 324 3

Riess, A. G., Filippenko, A. V., Challis, P., et al. 1998, AJ, 116, 1009 9

Romani, R. W., Filippenko, A. V., Silverman, J. M., et al. 2012, ApJ, 760, L36 8

Santos, E. 2012, Ap&SS, 341, 411 14

Sawai, H., Yamada, S., & Suzuki, H. 2013, ApJ, 770, L19 16

Schwarz, J. H., & Seiberg, N. 1999, Reviews of Modern Physics Supplement, 71, 112

Seljak, U., Slosar, A., & McDonald, P. 2006, J. Cosmology Astropart. Phys., 10, 14

Shapiro, S. L., & Teukolsky, S. A. 1983, Black holes, white dwarfs, and neutron stars: The physics of compact objects 2

Shu, C.-W. 2003, International Journal of Computational Fluid Dynamics, 17, 107 83

Strand, B. 1994, Journal of Computational Physics, 110, 47 81

Tadmor, E. 1989, SIAM Journal on Numerical Analysis, 26, 30 83

—. 1990, Computer Methods in Applied Mechanics and Engineering, 80, 197 83

Thompson, C., & Duncan, R. C. 1993, ApJ, 408, 194 16, 91

—. 1995, MNRAS, 275, 255 15

—. 1996, ApJ, 473, 322 15

Toro, E. F. 2009, Riemann solvers and numerical methods for fluid dynamics: a practical introduction (Springer Science & Business Media) 58, 82

Upadhye, A., & Hu, W. 2009, Phys. Rev. D, 80, 064002 14

van Kerkwijk, M. H., Breton, R. P., & Kulkarni, S. R. 2011, ApJ, 728, 95 8, 20, 29, 31, 32

Weinberg, S. 1972, Gravitation and Cosmology: Principles and Applications of the General Theory of Relativity 23, 55

—. 1989, Reviews of Modern Physics, 61, 1 11

Weinstein, S., & Rickles, D. 2015, in The Stanford Encyclopedia of Philosophy, summer 2015 edn., ed. E. N. Zalta 9

Will, C. M. 2006, Living Reviews in Relativity, 9, 3 13

—. 2014, Living Reviews in Relativity, 17, 4 8

Wilson, C. M., Johansson, G., Pourkabirian, A., et al. 2011, Nature, 479, 376 10

Witten, E. 1998, Advances in Theoretical and Mathematical Physics, 2, 253 9

—. 2001, ArXiv High Energy Physics - Theory e-prints, hep-th/0106109 9

Zrake, J., & MacFadyen, A. I. 2013, ApJ, 769, L29 16